gut ausgelegt

Measurement of Positron-Proton Scattering at $Q^2 = 0.25\,GeV^2$

by

M. Löwe

Measurement of Positron-Proton Scattering at $Q^2 = 0.25\,GeV^2$

Dissertation
zur Erlangung des Doktorgrades
des Fachbereichs Physik
der Universität Hamburg

vorgelegt von

Martin Löwe
aus Hamburg

Hamburg
1995

Zusammenfassung

In dieser Arbeit wird gezeigt, daß es am HERA Speichering möglich ist, Wirkungsquerschnitte bei kleinen Werten des Viererimpulsübertrags Q^2 in der Positron-Proton Streuung zu bestimmen. Die Positronen, die unter kleinen Winkeln ($19\,mrad < \theta < 34\,mrad$) gestreut werden, können durch ein Wolframkalorimeter, das durch Siliziumdioden ausgelesen wird, nachgewiesen werden. Dieses kompakte Kalorimeter befindet sich direkt neben dem Strahlrohr des Speicherrings, daher der Name Strahlrohrkalorimeter. Aufgrund der räumlichen Nähe zu den in HERA umlaufenden Teilchenpaketen ist auf gute Abschirmungen zu achten. Insbesondere die hohe Strahlenbelastung ist zu berücksichtigen.

Um das Kalorimeter auszulesen, wird ein Datennahmesystem eingesetzt, das auf einer Transputer-architektur aufbaut. Bei einer Kollisionsrate von $10.4\,MHz$ wird eine Sample & Hold Schaltung verwendet. Mittels einfacher Energieschwellen und Zeitschnitten wird bei Luminositäten von $10^{30}\,cm^{-2}\,s^{-1}$ eine Ereignisrate von $10\,Hz$ auf der ersten Triggerstufe erreicht.

Der über den dem Strahlrohrkalorimeter zugänglichen kinematischen Bereich gemittelte Positron-Proton Wirkungsquerschnitt ist $\sigma_{ep} = 49.5 \pm 9.1(\text{stat}) + 13.3/ - 17.1(\text{syst})\,nb$ bei einem mittleren $\langle Q^2 \rangle = 0.25\,GeV^2$ und Bjorken-$x = 7.4 \cdot 10^{-6}$. Dies kann in einen totalen Wirkungsquerschnitt für die Streuung von virtuellen Photonen an Protonen bei $\langle Q^2 \rangle = 0.25\,GeV^2$ umgerechnet werden: $\sigma_{\gamma^* p} = 130 \pm 24(\text{stat}) + 35/ - 45(\text{syst})\,\mu b$. Die mittlere Energie im Photon-Proton Schwerpunktsystem ist dabei $W = 183\,GeV$. Den Wert für die Protonstrukturfunktion erhält man zu $F_2 = 0.30 \pm 0.12$. Dies stimmt im Rahmen der Fehler mit der Vorhersage von Donnachie und Landshoff überein.

Abstract

The feasibility of measuring cross sections at small values of the squared four-momentum transfer Q^2 in positron-proton collisions at HERA is demonstrated. The positrons scattered at small angles ($19\,mrad < \theta < 34\,mrad$) are detected by a small tungsten calorimeter with silicon diode readout mounted on the beampipe of the ZEUS detector, hence the name beampipe calorimeter. The operation of a beampipe calorimeter close to the beams of the HERA storage ring requires special care, in particular the high radiation background needs attention.

A transputer based readout system, with a sample & hold architecture was used to take data at a beam crossing frequency of $10.4\,MHz$. Making use of simple energy thresholds and timing cuts, a first-level trigger rate on the order of $10\,Hz$ was achieved at a luminosity of $10^{30}\,cm^{-2}\,s^{-1}$.

The ep cross section integrated over the kinematical range accessible to the beampipe calorimeter has been determined to $\sigma_{ep} = 49.5 \pm 9.1(\text{stat}) + 13.3/ - 17.1(\text{syst})\,nb$ at a mean $\langle Q^2 \rangle = 0.25\,GeV^2$ and Bjorken-$x = 7.4 \cdot 10^{-6}$. Translating this into a total cross section of virtual photons on protons yields $\sigma_{\gamma^* p} = 130 \pm 24(\text{stat}) + 35/ - 45(\text{syst})\,\mu b$ at a photon-proton center of mass energy of $W = 183\,GeV$ and a mean $\langle Q^2 \rangle = 0.25\,GeV^2$. The proton structure function is $F_2 = 0.30 \pm 0.12$. This value agrees with the prediction of Donnachie-Landshoff within errors.

Contents

List of Figures

List of Tables

1 Introduction

Measurements of the total hadron-proton cross sections at high energies have since a long time been an important input to our understanding of some aspects of the high energy behaviour of strong interactions. Among others, the attempt to understand total cross sections has given a strong impetus to Regge theory and led to important applications and insights based on the Regge trajectory concept.

At large values of the center of mass energy ($W > 10\,GeV$) all hadron-proton cross sections show a slow rise with energy [6, 21] which cannot be explained by conventional Regge trajectories. This led to the introduction of the Pomeron, a 'particle' with the quantum numbers of the vacuum, whose exchange leads to the observed behaviour of the total cross sections. New measurements at very high energies at the $\bar{p}p$ collider at CERN [78] and at HERA [43, 83] have shed new light at this hypothetical particle, and its investigation is presently at the center of interest. Interactions of high energy (virtual) photons can be incorporated into this body of knowledge via the vector dominance model (VMD), which has been shown to work well at sub-HERA energies. It connects photon-proton interactions with vector-meson-proton reactions, and thus should describe photoproduction by the same formalism as hadron-hadron interactions.

For the total photoproduction cross section, a similar behaviour had been indicated in fixed target experiments before the advent of HERA. Now the HERA storage ring allows measurements of photoproduction at very high energies, corresponding to about $40\,TeV$ beam energy in a fixed target arrangement. Therefore the asymptotic behaviour of photoproduction becomes quite evident in the HERA regime.

Figure 1.1 shows the measurements of the total photoproduction cross section of protons at HERA together with the measurements at lower energies. The slow rise of the cross section with center of mass energy W is evident; it is consistent with theoretical predictions from Regge models derived from hadron-hadron interactions. Now, in contrast to hadron-hadron interactions, there is an additional dimension to explore with photons, because photons can be easily put off the mass shell in electroproduction experiments. Scattering can be explored at various values of Q^2, the virtuality of the photon. This technique yields new insights: in contrast to the slow rise of the total γp cross section of real photons, the cross section $\sigma_{\gamma^* p}^{tot}$ of virtual photons at values of Q^2 greater than a few GeV^2 shows a strong rise with the center of mass energy W; this is shown in figure 1.2. This can be understood as a consequence of the strong rise in the proton structure function F_2 at small values of Bjorken x, which has been measured at HERA [41, 81] and is shown in figure 1.3. In the parton model it can be interpreted as a strong rise in parton densities at small values of x and has aroused considerable theoretical interest.

The intermediate Q^2 region between photoproduction with real photons and the region of deep inelastic scattering ($0 < Q^2 <$ a few GeV^2) has so far not been measured at HERA. It is of considerable interest to explore how the cross section develops with Q^2 in between the two very different ways of behaviour, which has been seen for real photoproduction and deep inelastic scattering. Also, some theoretical descriptions of deep inelastic scattering in the context of QCD use as an anchorpoint parton densities in this intermediate region of Q^2 [37]. Experimentally, to get to this transition region at small Q^2, one has to go to very small angles of the scattered positron. At HERA energies, this corresponds to angles of about 25 mrad. It poses an experimental challenge to operate detectors a few centimeters away from positron and proton beams.

In this thesis a feasibility study of such a measurement is presented. The scattered positron/electron is detected in a beampipe calorimeter, with tungsten absorber plates and silicon diode readout. This choice of materials allows a compact design necessary to detect positrons at small angles. The calorimeter was placed 3.06 m from the interaction point in the positron direction directly next to the beampipe, a few centimeters away from the circulating beams. The design, running experience, problems, and a first measurement of the total photon-proton cross section in this new Q^2 region will be presented.
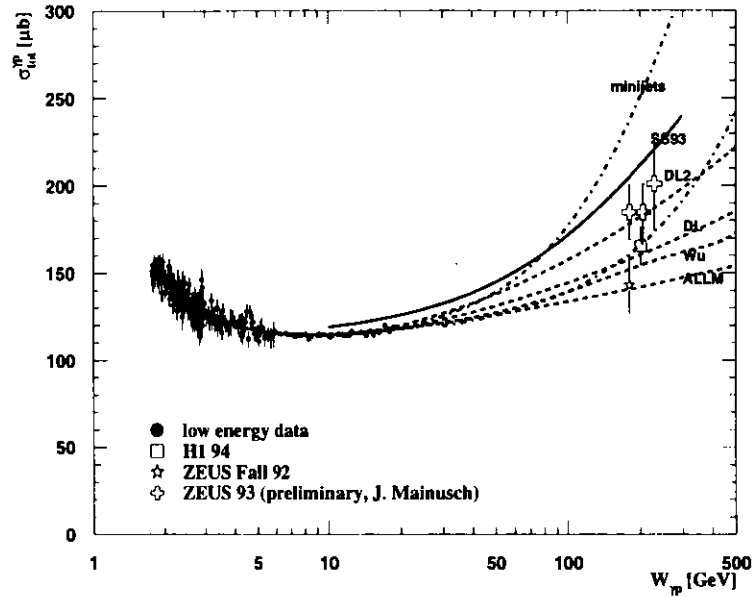
Figure 1.1: Total photoproduction cross sections from low energy and HERA data, adopted from [57]. The H1 point is taken from [42], the ZEUS data are from [85] and [57], and the low energy data from [51].
The dashed lines labeled ALLM [1], Wu [14], DL [28] and DL2 are results from different parametrizations of $\sigma^{tot}_{\gamma^*p}$. The curve labeled DL2 uses a pomeron intercept of $\epsilon - 1 = 0.112$ as resulting from recent measurements by the CDF collaboration [21].
The dash-dotted lines show the cross section calculated with the inclusion of hard scattering [71], so called minijet models. A $p_t^{min} = 2GeV(1.4GeV)$ is used for the lower (higher) prediction using the Drees-Grassie [31] parton distribution of the photon.
The solid line is a prediction from Schuler and Sjöstrand [70].
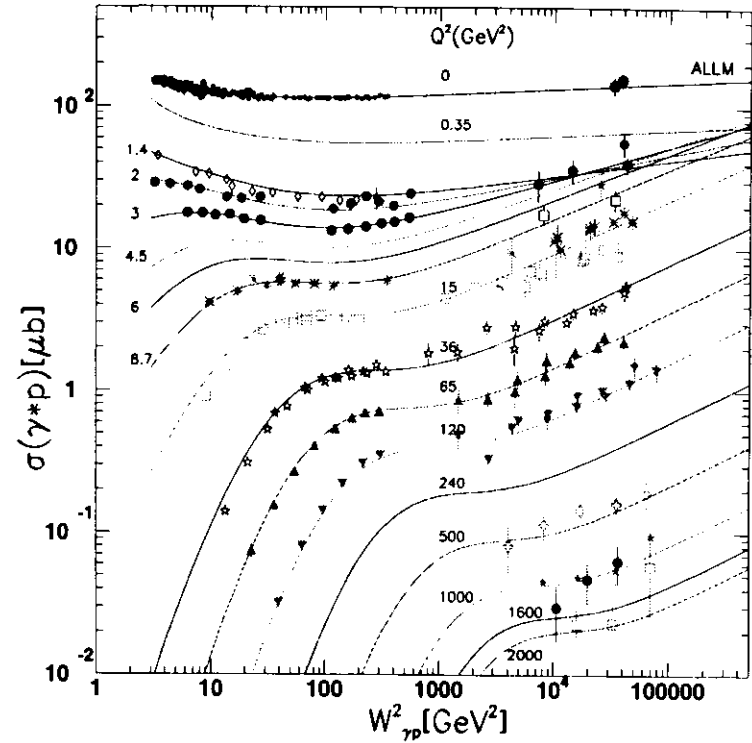
Figure 1.2: Total γ^*p cross section as function of the center of mass energy squared, W^2. The curves are ALLM parametrizations [1], fitted to the lower energy data ($W'^2 < 400GeV^2$), and extrapolated to the high energy region (adapted from [52]). The parameters are different values of Q^2 measured in GeV^2.
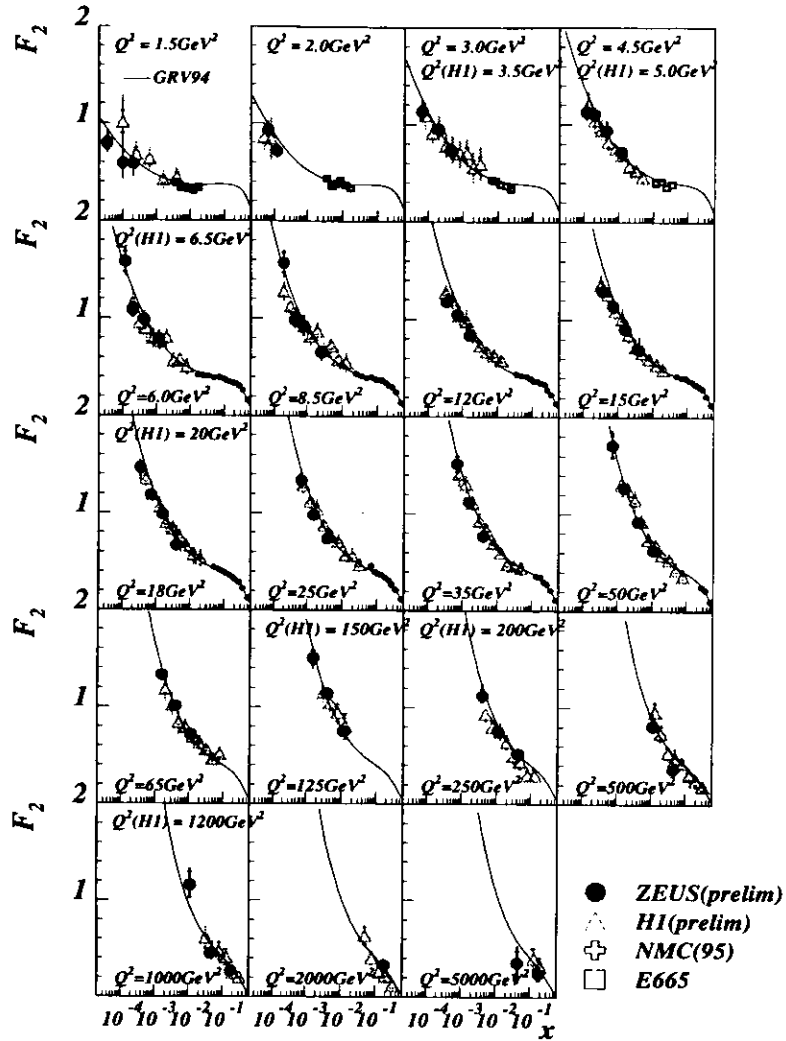
Figure 1.3: Proton structure function F_2 versus x_{BJ} for different Q^2 bins. The curves are parametrizations from next to leading order calculations. The plot is taken from [50].

2 Theoretical framework

The high Q^2 behaviour ($Q^2 > 1.5 GeV$) of electron proton scattering, also termed deep inelastic scattering (DIS), is well described by perturbative quantum chromodynamics (QCD).

At lower values of Q^2 perturbation theory breaks down. In the very low Q^2 regime Regge theory is able to describe the total cross section of photoproduction ($Q^2 = 0$) quite well.

The kinematical region probed by the measurements with the new beampipe calorimeter is $y_{Bjorken} \approx 0.37$ corresponding to $W = 183 GeV$, $Q^2 \approx 0.25 GeV^2$, and $x_{Bj} = 7.4 \cdot 10^{-6}$. This region is in the transition between deep inelastic scattering and photoproduction. The next sections give a brief introduction into the different regimes.
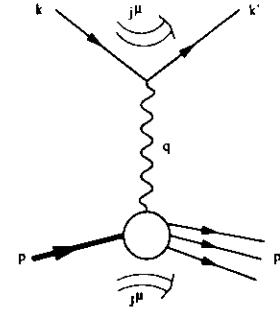
Figure 2.1: Feynman diagram of lepton nucleon scattering in lowest order α

2.1 Deep inelastic scattering

Scattering of electrons off protons in first order perturbation theory (i.e. QED) is shown in figure 2.1. An incoming lepton with four momentum k scatters off an incoming proton with four-momentum p and mass M. The outgoing lepton has momentum k', the outgoing hadronic system (which might be the original nucleon in case of elastic scattering) has momentum p_X and mass M_X. The invariants used are listed in table 2.1.

$$q^2 \equiv (k - k')^2 = -Q^2; \ Q^2 > 0 \tag{2.1}$$
$$s \equiv (p + k)^2 \tag{2.2}$$
$$t \equiv (p - p_X)^2 \tag{2.3}$$
$$W^2 \equiv (q + p)^2 \tag{2.4}$$
$$\nu \equiv \frac{p \cdot q}{M} = \frac{1}{2M}(W^2 + Q^2 - M^2), \tag{2.5}$$

Table 2.1: Definition of kinematical invariants

The transition amplitude for elastic scattering is given by (setting $p_X = p'$ the four momentum of the

outgoing nucleon)

$$T_{fi} = -i \int j^\mu \left(-\frac{g_{\mu\nu}}{q^2}\right) J^\nu d^4x, \tag{2.6}$$

where $q = k - k'$ in the propagator term refers to the four momentum of the exchanged photon. The electron transition current j^μ and the proton transition current J^μ are given by

$$j^\mu = -e\bar{u}(k')\gamma^\mu u(k)e^{i(k'-k)x} \tag{2.7}$$

$$J^\mu = -e\bar{u}(p_x)\Gamma^\mu u(p)e^{i(k'-k)x}, \tag{2.8}$$

where the $u(p)$ are Dirac fermion spinors. The ignorance of the internal structure of the nucleon is parametrized in

$$\Gamma^\mu = F_1(q^2)\gamma^\mu + \frac{\kappa}{2M}F_2(q^2)i\sigma^{\mu\nu}q_\nu, \tag{2.9}$$

where F_1 and F_2 are two independent form factors, κ is the anomalous magnetic moment, and M the mass of the nucleon.

It should be noted, that not only massless photons can be exchanged between the lepton and the nucleon, but also massive gauge bosons. For electron proton scattering, the Z_0 as well as the charged W may become exchanged. The propagator term for massive gauge bosons of mass M_G is

$$\frac{-i(g_{\mu\nu} - \frac{q_\mu q_\nu}{M_G^2})}{q^2 - M_G^2}. \tag{2.10}$$

Due to the mass term M_G^2 in the denominator ($M_W = 80\,GeV$, $M_Z = 91\,GeV$) massive gauge bosons can be completely ignored in the kinematical regime of this analysis ($Q^2 \approx 0.25\,GeV^2$).

The cross section can be written as

$$\frac{d\sigma}{dE'd\Omega} = \frac{\alpha^2}{q^4}\frac{E'}{E}(L_{\mu\nu})_{lepton}(L^{\mu\nu})_{nucleon} \tag{2.11}$$

with the tensor

$$L^{\mu\nu} \equiv \frac{1}{2}\sum_{spins}[\bar{u}(k')\gamma^\mu u(k)][\bar{u}(k')\gamma^\nu u(k)]^*. \tag{2.12}$$

The cross section in the laboratory frame for elastic scattering becomes then

$$\left.\frac{d\sigma}{d\Omega}\right|_{lab} = \frac{\alpha^2}{4E^2\sin^4\frac{\theta}{2}}\frac{E'}{E}\left(\frac{G_E^2 + \tau G_M^2}{1 + \tau}\cos^2\frac{\theta}{2} + 2\tau G_M^2\sin^2\frac{\theta}{2}\right). \tag{2.13}$$

The above equation is known as the Rosenbluth formula, where the following quantities have been introduced:

E energy of the incoming lepton
E' energy of the outgoing lepton
θ scattering angle of the lepton
τ $\equiv -q^2/4M^2$
G_E $\equiv F_1 + \kappa F_2 \cdot q^2/(4M^2)$
G_M $\equiv F_1 + \kappa F_2$

The form factors G_E and G_M are closely related to the nucleon electric and magnetic moment distributions in the brick wall frame.

In the case of inelastic scattering, the outgoing hadronic system consists of several particles that cannot be described by a single Dirac fermion spinor. The hadronic tensor in (2.11) is parametrized for the spin averaged cross section as

$$W^{\mu\nu} = W_1\left(-g^{\mu\nu} + \frac{q^\mu q^\nu}{q^2}\right) + W_2\frac{1}{M}\left(p^\mu - \frac{p \cdot q}{q^2}q^\mu\right)\left(p^\nu - \frac{p \cdot q}{q^2}q^\nu\right), \tag{2.14}$$

with W_1 and W_2 two independent inelastic structure functions. These structure functions depend on two independent variables. A conventional choice is q^2 and ν.

The cross section in the laboratory frame is then

$$\left.\frac{d\sigma}{dE'd\Omega}\right|_{lab} = \frac{\alpha^2}{4E^2\sin^4\frac{\theta}{2}}\left[W_2(\nu, q^2)\cos^2\frac{\theta}{2} + 2W_1(\nu, q^2)\sin^2\frac{\theta}{2}\right]. \tag{2.15}$$

The lepton mass m_e and the nucleon mass have been neglected. These masses show up in additional terms like m_e^2/Q^2 and M^2/s. In the kinematical range of this analysis, $m_e^2 \ll Q^2 \ll M_W^2$ and $s \approx 9 \cdot 10^4\,GeV^2$. Therefore the terms $m_e^2/Q^2 \ll 1$ and $M^2/s \ll 1$ can be safely ignored.

2.1.1 Total photon proton cross section

The total cross section for scattering of real photons of energy K and helicity λ off unpolarized protons can be obtained along the lines of the preceeding section where the lepton tensor is replaced by the polarization vector ϵ_λ^μ

$$L^{\mu\nu} \to \epsilon_\lambda^{\mu*}\epsilon_\lambda^\nu, \tag{2.16}$$

and no internal propagator of course.

$$\sigma_\lambda^{tot} = \frac{4\pi^2\alpha}{K}\epsilon_\lambda^{\mu*}\epsilon_\lambda^\nu W^{\mu\nu} \tag{2.17}$$

In equation (2.17) real photons have a flux factor $4MK$ associated with them. For virtual photons $q^2 \neq 0$ the flux is not well defined any more. The conventional choice is to require

$$W^2 = (p + q)^2 = M^2 + 2MK \tag{2.18}$$

to hold, leading to

$$K = \frac{W^2 - M^2}{2M} = \nu + \frac{q^2}{2M}. \tag{2.19}$$

This is known as the Hand convention. Using (2.14) one obtains for the cross sections of transversely and longitudinally polarized photons on protons:

$$\sigma_T \equiv \frac{1}{2}\left(\sigma_{\lambda=+1}^{tot} + \sigma_{\lambda=-1}^{tot}\right) = \frac{4\pi^2\alpha}{K}W_1(\nu, q^2) \tag{2.20}$$

$$\sigma_L \equiv \sigma_{\lambda=0}^{tot} = \frac{4\pi^2\alpha}{K}\left[\left(1 - \frac{\nu^2}{q^2}\right)W_2(\nu, q^2) - W_1(\nu, q^2)\right] \tag{2.21}$$

2.1.2 Quark parton model

At values of $Q^2 \gg M_p^2$ the virtual photon starts to resolve the constituents of the nucleon. In the approximation of the naive quark parton model the structure functions W_1 and W_2 are independent of Q^2 at fixed x_{Bj}, the so called Bjorken scaling variable:

$$\nu W_2(\nu, Q^2) \equiv F_2(x) \tag{2.22}$$

$$M W_1(\nu, Q^2) \equiv F_1(x), \tag{2.23}$$

where the dimensionless variables

$$x_{Bj} \equiv \frac{-q^2}{2p \cdot q} = \frac{-q^2}{2M\nu} \tag{2.24}$$

$$y_{Bj} \equiv \frac{p \cdot q}{p \cdot k} \tag{2.25}$$

have been introduced.

The double differential cross section for deep inelastic lepton nucleon scattering (2.15) then becomes

$$\frac{d^2\sigma_{ep}(y, q^2)}{dy dQ^2} = \frac{4\pi\alpha^2}{Q^4} \left[yx F_1(x) + \frac{1}{y}(1-y)F_2(x) \right]. \tag{2.26}$$

The structure functions F_1 and F_2 are identified with the momentum distributions $f_i(x)$ of the quarks within the nucleon (quark structure functions):

$$F_2(x) = \sum_i e_i^2 x f_i(x), \tag{2.27}$$

where the sum includes all valence and sea quarks of the nucleon, e_i is the charge of the respective quark. Due to the spin 1/2 of the partons one has in the naive parton model the Callan-Gross relation [19]

$$F_2 = 2x F_1(x). \tag{2.28}$$

By integrating over the quark structure functions one obtains momentum sum rules. Checking with data reveals that about 50% of the momentum of a nucleon is not carried by the quarks. Therefore some other constituents, namely the gluons, in the nucleon have to participate in the dynamics. Gluons can be emitted like Bremsstrahlung from the quarks within the nucleon. This gives rise to logarithmic violations of scaling. At lowest order this leads to

$$F_2(x, Q^2) = x \cdot \sum_q e_q^2 \int_x^1 \frac{d\xi}{\xi} f_q(\xi) \left(\delta\left(1 - \frac{x}{\xi}\right) + \frac{\alpha_s}{2\pi} P_{qq}\left(\frac{x}{\xi}\right) \log \frac{Q^2}{\mu^2} \right) \tag{2.29}$$

The $P_{qq}(z)$ represents the probability of a quark emitting a gluon and so becoming a quark with momentum reduced by a fraction z. The lower limit μ on the transverse momentum is introduced as a cutoff to regularize the divergence when $Q^2 \to 0$, and α_s is the strong coupling constant. The quark densities $f_q(x, Q^2)$ now depend also on Q^2.

The Q^2 evolution of the quark densities is expressed by

$$\frac{df_q(x, Q^2)}{d \log Q^2} = \frac{\alpha_s}{2\pi} \int_x^1 \frac{d\xi}{\xi} f_q(\xi, Q^2) P_{qq}\left(\frac{x}{\xi}\right). \tag{2.30}$$

Similar equations describe the evolution of the gluon densities. This system of integro-differential equations is called the DGLAP equations [4, 27, 39].

The approximate solutions of the DGLAP equations predict a growth of parton densities $f_q(x, Q^2)$ for $x \to 0$ for fixed Q^2. This translates into a growth of F_2 which is confirmed by experiment, see figure 1.3 on page 4 and figure 2.2 on page 10.

In case massive gauge bosons are not ignored in the propagator term, the neutral current (2.7) has a parity violating (vector - axial vector) structure

$$j_\mu^{NC} = \bar{u}(k')\gamma_\mu \frac{1}{2}(c_V^e - c_A^e \gamma_5)u(k), \tag{2.31}$$

with c_V^e and c_A^e the electro-weak coupling constants of the electron as defined in the Standard Model. The lepton tensor then contains anti-symmetric components. More structure functions have to be introduced; exploiting CP invariance and neglecting the lepton mass, only one extra structure function is needed [68]. The cross section (2.26) becomes

$$\left.\frac{d^2\sigma(y, q^2)}{dy dQ^2}\right|_{e^\pm p \to X} = \frac{4\pi\alpha^2}{Q^4} \left[yx F_1(x) + \frac{1}{y}(1-y)F_2(x) \pm (1 - \frac{y}{2})x F_3(x) \right]. \tag{2.32}$$

Due to the small value of the four momentum transfer F_3 can be completely neglected for this analysis, see the argument following equation (2.10).

2.1.3 The Weizsäcker-Williams approximation

Using the definition of the structure functions F_1 and F_2 in (2.22) and (2.23) and making use of $\nu^2/Q^2 = 2.5 \cdot 10^4 y/x \gg 1$ for the entire kinematic range (excluding only a small region of quasi-elastic scattering with $y/x < 10^{-4}$), the virtual photon proton cross sections (2.20) and (2.21) become

$$\sigma_T = \frac{4\pi^2\alpha}{MK} F_1 \tag{2.33}$$

$$\sigma_L = \frac{4\pi^2\alpha}{MK} \left[\frac{F_2}{2x} - F_1 \right] = \frac{4\pi^2\alpha}{MK} \frac{F_L}{2x}, \tag{2.34}$$

where the longitudinal structure function

$$F_L \equiv F_2 - 2x F_1 \tag{2.35}$$

has been introduced. Note that the Callan-Gross relation (2.28) of the naive parton model is expected to be violated at small values of Q^2 and x.

For small x or $Q^2 \ll M$ the flux factor (2.19) $K = \nu(1 - x)$ is just $K = \nu$. Solving (2.33) and (2.34) for F_1 and F_2 yields

$$x F_1 = \frac{1}{4\pi^2\alpha} \frac{Q^2}{2} \cdot \sigma_T \tag{2.36}$$

$$F_2 = \frac{1}{4\pi^2\alpha} \cdot Q^2 \cdot (\sigma_T + \sigma_L). \tag{2.37}$$

ZEUS 1994
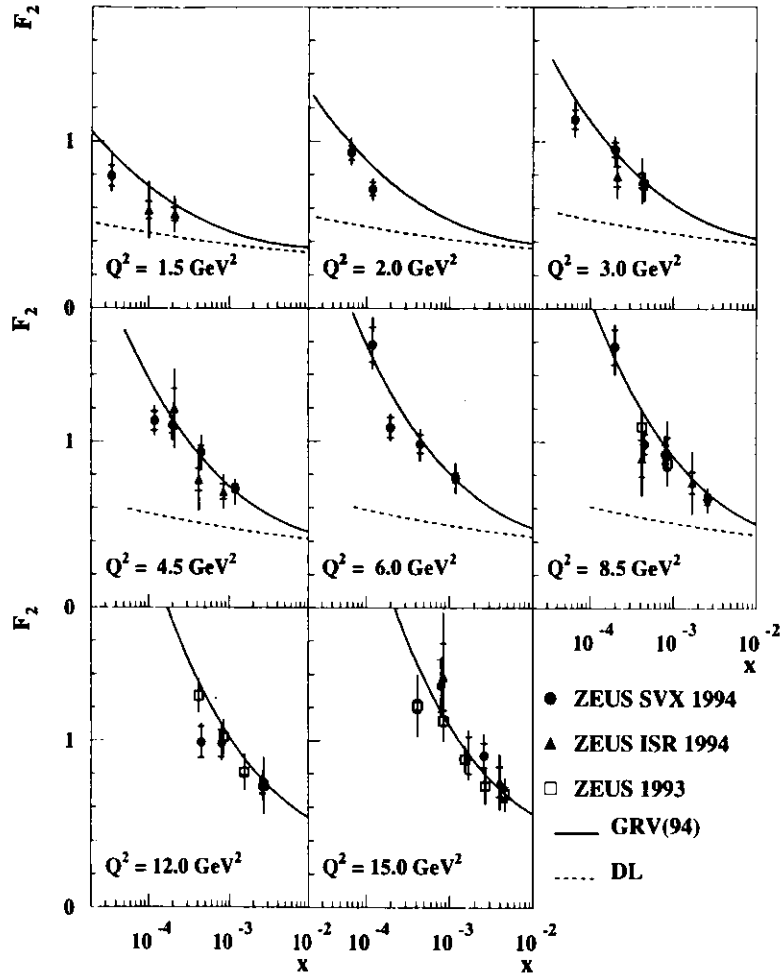
Figure 2.2: The measured structure function F_2 as measured by ZEUS in low Q^2 bins [82]. Shown are results from a shifted vertex analysis (SVX, solid dots), initial state radiation analysis (ISR, solid triangles) and from the 1993 analysis (open squares), compared with the expectations from GRV(94) (solid line) and Donnachie and Landshoff (DL) (dashed line). Overall normalisation uncertainties of 3% for the 1994 results and 3.5% for the 1993 points are not shown. The inner error bars represent the statistical errors, while the outer bars represent the systematical error added in quadrature to the statistical errors.

Inserting (2.36) and (2.37) into (2.26) one gets for $Q^2 \gg m_e^2$

$$\frac{d^2\sigma_{ep}(y,Q^2)}{dydQ^2} = \frac{\alpha}{2\pi}\frac{1}{Q^2}\left[\frac{1+(1-y)^2}{y}\sigma_T(y,Q^2)+2\frac{(1-y)}{y}\sigma_L(y,Q^2)\right]. \tag{2.38}$$

This is the Weizsäcker-Williams approximation. The cross section for electron proton collisions is expressed in terms of the cross section for photons on protons. The probability that such a photon is emitted from the incoming electron is expressed by the kinematical factors given above. For Q^2 getting closer to m_e^2 and in particular for the photoproduction limit, more terms have to be kept in (2.15) which account for 7% of the total photoproduction cross section at HERA energies [17].

2.2 Regge theory

Regge theory is based on the assumption of analyticity[1] of the scattering amplitude $\mathcal{A}$. In the partial wave formalism [54] the scattering amplitude $\mathcal{A}$ is continued into the unphysical region

$$\mathcal{A}(s,t) = \sum_{l=0}^{\infty}(2l+1)\cdot a_l \cdot P_l(z), \tag{2.39}$$

with the square center of mass energy s and the square four-momentum transfer on the hadron vertex t as given in table 2.1 on page 5.

In a diagram of J versus M^2 (Chew-Frautschi plot, see figure 2.3) the observation is that particles and resonances with a given spin J and mass M line up on certain trajectories. The idea is that the partial wave amplitude a_l can be identified with a propagator like term for the *exchanged* particles

$$a_l = \frac{\Gamma_l(t)}{t-m_l^2}, \tag{2.40}$$

where $\Gamma_l(t)$ is the partial decay width of a given particle of mass m_l. The recipe to obtain the scattering amplitude for a reaction is to select the trajectory with the suitable set of quantum numbers that are exchanged in that reaction. Equation (2.39) then becomes for the s-channel process

$$\mathcal{A}(t) = \sum_{\substack{l=0,2,4,\ldots \\ l=1,3,5,\ldots}}^{\infty}(2l+1)\cdot\frac{\Gamma_l(t)}{t-m_l^2}\cdot P_l(z), \tag{2.41}$$

summed over the particles with mass m_l on the appropriate trajectory. The selection of even or odd values of l is due to the parity conservation of the strong interaction.

The scattering amplitude (2.41) can be continued to complex l. As Regge has proved [67] this is possible for a wide class of potentials, the only singularities being poles, so called 'Regge poles'. The sum then becomes an integral along an appropriately choosen path ζ in the complex l plane:

$$\mathcal{A}(t) = \frac{1}{2i}\int_\zeta dl(2l+1)\cdot\frac{\Gamma_l(t)}{t-m_l^2}\cdot\frac{e^{i\pi l}\pm 1}{2}\cdot\frac{P_l(z)}{\sin(\pi l)}, \tag{2.42}$$

where the $P_l(z)$ are now Legendre functions of the first kind for complex l. The term $(e^{i\pi l}\pm 1)/2$ ensures that only the poles with even (+) or odd (-) angular momentum contribute. Following the

---

[1]More precisely 'maximal analyticity of the second kind', i.e. the scattering amplitude has only isolated singularities in the complex l plane [25].
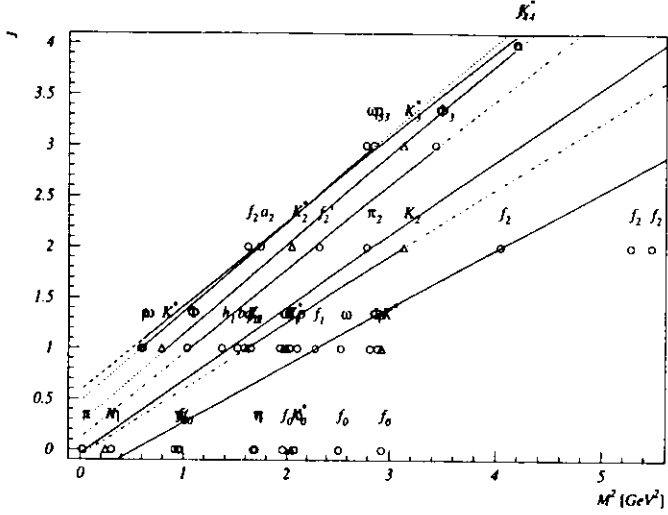
Figure 2.3: Chew-Frautschi plot. All mesons containing u, d, s quarks are plotted in the plane angular momentum J versus mass squared M^2, data from [64]. The $\circ$ are mesons made of u and d quarks and antiquarks, the $\triangle$ represent mesons including s quarks. The solid lines are fits to the Regge trajectories, the dashed and dotted lines their extensions into the nonfitted regions.

Cauchy theorem, this integral equals the sum of the residues of the poles enclosed by the path, which leads to (2.41).

The Chew-Frautschi plot suggests that there is a function

$$l = \alpha(m_l^2) \tag{2.43}$$

linking the particles and resonances of given isospin and strangeness, which can be expanded around $t = m_l^2$:

$$\alpha(t) \cong l + \frac{d\alpha}{dt}(t - m_l^2), \tag{2.44}$$

neglecting higher derivatives. This can be put into (2.42)

$$A(t) = \frac{1}{2i} \int_\zeta dl \frac{e^{i\pi l} \pm 1}{2 \sin(\pi l)} \cdot (2l + 1) \cdot \frac{\Gamma_l(t)}{\alpha(t) - l} \cdot \frac{d\alpha(t)}{dt} \cdot P_l(z). \tag{2.45}$$

One assumes that the integrand vanishes on an appropriately choosen path. With the pole at $\alpha(t) = l$ Cauchy's theorem reduces the integral to just the residue of the pole

$$A(t) = -\pi \frac{e^{i\pi\alpha(t)} \pm 1}{2 \sin(\pi\alpha(t))} \cdot (2\alpha(t) + 1) \cdot \Gamma_{\alpha(t)} \cdot \frac{d\alpha(t)}{dt} \cdot P_{\alpha(t)}(z). \tag{2.46}$$

After this simplification the sum (2.41) over many particles becomes just a single term. The term $\alpha(t)$ is commonly known as a Regge trajectory. The functional behaviour can be deduced from the Chew-Frautschi plots. In figure 2.3 linear fits are applied to trajectories of fixed isospin I.

The value for the fit of the highest lying trajectory $\alpha_{\rho,\omega}(t)$ including higher spin states taken from the literature [29] is

$$\alpha(t) = 0.44 + 0.93 \cdot |t|. \tag{2.47}$$

Since $|t|$ is usually small compared to s, $P_{\alpha(t)}$ has the asymptotic behaviour for large s of

$$P_{\alpha(t)}(z) \approx e^{-i\pi\alpha(t)} \cdot \left(\frac{s}{s_0}\right)^{\alpha(t)}. \tag{2.48}$$

Therefore the scattering amplitude can be written as

$$A(t) = \beta(t) \cdot \left(\frac{s}{s_0}\right)^{\alpha(t)}. \tag{2.49}$$

This result shows that all the contributions to the cross section of a given process depend only on the Regge trajectory for all the resonances on the corresponding trajectory. The differential cross section at $|t| \ll s$ is

$$\frac{d\sigma}{dt} \approx s^{-2}|A|^2 = |\beta(t)|^2 \left(\frac{s}{s_0}\right)^{2\alpha(t)-2}, \tag{2.50}$$

where $\alpha(t)$ is the Regge trajectory of the process given.

The optical theorem relates the *total* cross section to the imaginary part of the elastic ($t = 0$) scattering amplitude in the forward direction.

$$\sigma^{tot} = \frac{1}{s} \Im A(t = 0). \tag{2.51}$$

Putting in equation (2.49) yields

$$\sigma^{tot} \sim s^{\alpha(t=0)-1}. \tag{2.52}$$

This shows that the total cross section is dominated by the highest lying trajectory. From (2.47) one has $\alpha(0) = 0.44$, therefore

$$\sigma^{tot} \sim s^{-\frac{1}{2}} \tag{2.53}$$

is predicted.

This behaviour is not observed by hadron-proton interactions at high energy. Rather a slow rise of cross sections is observed at center of mass energies $W \gg 10\,GeV$. This energy behaviour cannot be explained by the exchange of a conventional trajectory and therefore requires the introduction of a hypothetical particle, the Pomeron. The Pomeron has the quantum numbers of the vacuum, $I^P = 0^+, S = B = Q = 0$, and the intercept of its trajectory at $t = 0$ is expected to be $\alpha_{I\!P}(0) \gtrsim 1$.

Donnachie and Landshoff [29] have successfully fitted the total cross sections at high energy for $pp, p\bar{p}, \pi^{\pm}p, K^{\pm}p$, and γp to a sum of two terms, one due to the Pomeron trajectory and one due to the exchange of the highest lying conventional trajectory (ρ, ω, f, a). Their ansatz of the form

$$\sigma^{tot} = X \cdot W^{2\epsilon} + Y \cdot W^{-2\eta} \tag{2.54}$$

gives a good fit to the high energy cross sections and yields

$$\epsilon = 0.0808 \qquad \text{and} \qquad \eta = 0.4525 \tag{2.55}$$

corresponding to

$$\alpha_{I\!P} = 1.0808 \qquad \text{and} \qquad \alpha_\rho = 0.5475, \tag{2.56}$$

close to expectations.

Donnachie and Landshoff point out, that these exponents are 'effective' exponents - they are expected to show a (slow) dependence on W due to multiple exchanges; at present the data do not require this. At extremely high energies, when one approaches the Froissart-Martin bound [34]

$$\sigma^{tot} \underset{W \to \infty}{\leq} c \cdot (\log W)^2 \tag{2.57}$$

this might become relevant. This bound follows from unitarity of the partial wave scattering amplitudes and the optical theorem. It can also be proven from field theory [59]. Therefore some mechanism has to be invoked for the extremely high energy total cross sections to obey unitarity.

2.3 Application to inelastic ep scattering

Donnachie and Landshoff have applied these ideas to describe inelastic ep scattering at not too large values of Q^2 ($Q^2 \ll 10 GeV^2$) [30]. The total $\gamma^* p$ cross section for virtual photons can be connected with the proton structure function F_2 via equation (2.37). Near $Q^2 = 0$, where perturbation theory cannot be applied to describe F_2, it will depend on Q^2 and x. Its Q^2 dependence for small values of Q^2 is of the form of equation (2.37); its x dependence follows according to Regge theory the same Regge parametrizations as for hadrons.

Donnachie and Landshoff therefore make the following ansatz for F_2:

$$F_2(x, Q^2) = A x^{-0.8080} \left(\frac{Q^2}{Q^2 + a} \right)^{1.0808} + B x^{0.4525} \left(\frac{Q^2}{Q^2 + b} \right)^{0.5475} \tag{2.58}$$

with the same Regge exponents as for hadronic scattering and a Q^2 dependence suggested by equation (2.37). They have fitted this form to measurements of the NMC collaboration at lower energies and this can make a prediction for measurements at HERA; they are particularly relevant for the x, Q^2 values of this experiment.

2.4 Vector meson dominance model

The vector meson dominance model (VMD) [35, 69] is inspired by the fact that photon-hadron physics at high energies exhibit similar properties as hadron-hadron physics. The uncertainty principle allows a photon to fluctuate into $q\bar{q}$ pairs with the same quantum numbers as the photon: the vector mesons. The probability for this to occur is rather small but it is more than compensated for by the much larger cross section of mesons on protons. The main ingredients of this model shall be presented in the following. The notation used here follows [70].

The photon is modelled as a superposition of a bare photon $|\gamma_B\rangle$ and a hadronic component $\sqrt{\alpha}|h\rangle$

$$|\gamma\rangle = |\gamma_B\rangle + c\sqrt{\alpha}|h\rangle, \tag{2.59}$$

with c being a normalization constant. The hadronic state has to carry the same quantum numbers as the photon $J^{PC} = 1^{--}, Q = B = S = 0$.

The vector meson dominance model assumes that the bare component $|\gamma_B\rangle$ can be neglected with respect to the hadronic one. The simplest formulation of VMD assumes that the three lightest vector mesons ρ^0, ω, and ϕ are the sole hadronic constituents of the photon. It is motivated by the abundant production of those mesons that is observed in photoproduction. This results in

$$c\sqrt{\alpha}|h\rangle = \sum_{V = \rho^0, \omega, \phi} \frac{e}{f_V}|V\rangle. \tag{2.60}$$

The factor $4\pi\alpha/f_V^2$ gives the probability for the transition $\gamma \to V$. The couplings imply that the photon can be found in its VMD state for about 0.4% of the time. The coefficients $f_V^2/4\pi$ have been determined in fits to low energy data, for a detailed account, see [8].

	$f_V^2/4\pi$
ρ	2.20
ω	23.6
ϕ	18.4

$$\tag{2.61}$$

These coefficients are the geometrical mean of $e^+ e^-$ annihilation and photoproduction of vector mesons data. Usually, they are assumed to be independent of energy.

The inclusion of higher mass vector mesons is referred to as generalized vector meson dominance (GVD). All event classes known from hadron-hadron collisions may occur in the VMD model, such as elastic, diffractive, low-$p_\perp$ and high-$p_\perp$ events.

In the vector meson dominance model the single and double diffractive processes are

$$\begin{align}
\gamma + p &\to V + X, \tag{2.62}\\
\gamma + p &\to X + p, \tag{2.63}\\
\gamma + p &\to X_1 + X_2, \tag{2.64}
\end{align}$$

where the X denotes a final state made of several hadrons.

Non-diffractive events are characterized by

$$\gamma + p \to X, \tag{2.65}$$

where the system X does not allow identification of the reaction products with a dissociated photon or proton. The true elastic (Compton) process

$$\gamma + p \to \gamma + p \tag{2.66}$$

is of $\mathcal{O}(\alpha^2)$, whereas the VMD elastic process

$$\gamma + p \to V + p \tag{2.67}$$

is of $\mathcal{O}(\alpha)$, therefore the Compton process can generally be neglected.

If the transverse momentum $p_\perp$ in the event is larger than $\approx 1.3 GeV$ an exchanged gluon has a transverse wavelength that is smaller than the typical size of hadrons. It therefore starts to probe the partonic content of the vector mesons.

A class of events, that conventionally is not part of the vector meson dominance model, enters if the photon fluctuates into a $q\bar{q}$ pair of larger virtuality $Q^2 > 2.2\,GeV$. This process is perturbatively calculable. It gives rise to the anomalous part of the photon structure function, hence leading [70] to name it the 'anomalous' event class.

Putting together the VMD, the anomalous, and the direct class (interactions of the bare photon) the total cross section can be written as

$$\sigma^{tot}_{\gamma p} = \sigma^{VMD}_{\gamma p} + \sigma^{anom}_{\gamma p} + \sigma^{dir}_{\gamma p}. \tag{2.68}$$

For collisions of virtual photons γ^* with protons the prediction from the vector meson dominance model for transversely polarized photons at a $\gamma^* p$ center of mass energy W and a four-momentum transfer Q^2 of the virtual photon is

$$\sigma^{T}_{\gamma^* p}(W, Q^2) = \sum_{V=\rho^0,\omega,\phi} \frac{e^2}{f_V^2} \left(\frac{m_V^2}{m_V^2 + Q^2}\right)^2 \sigma^{T}_{Vp}(W), \tag{2.69}$$

where $\sigma^{T}_{Vp}(W)$ is the total cross section of transversely polarized vector mesons on protons at $Q^2 = 0$. Similarly, for longitudinally polarized photons one obtains

$$\sigma^{L}_{\gamma^* p}(W, Q^2) = \sum_{V=\rho^0,\omega,\phi} \frac{e^2}{f_V^2} \left(\frac{m_V^2}{m_V^2 + Q^2}\right)^2 \sigma^{T}_{Vp}(W) \cdot \frac{\xi_V Q^2}{m_V^2}. \tag{2.70}$$

The factor ξ_V defined by

$$\xi_V(W) = \frac{\sigma^{L}_{Vp}(W)}{\sigma^{T}_{Vp}(W)}, \tag{2.71}$$

with the expectation $0 \leq \xi_V \leq 1$, is introduced because the cross section may be different for longitudinally and transversely polarized hadrons. Some data suggest $\xi \approx 0$ [73]. A reanalysis [2] of that data contests this finding and suggests $\xi = 1$, as do references therein on small Q^2 data and as expected from the additive quark model or models based on exchange of Pomerons. The ratio (2.71) has also been measured at HERA for ρ^0 production in deep inelastic scattering [84],

$$\xi = 1.5 \begin{array}{c} +2.8 \\ -0.6 \end{array}, \tag{2.72}$$

where the statistical and systematic error have been added in quadrature.

Using above equations (2.69) and (2.70) and assuming $\xi = 1$ the cross section for longitudinally polarized photons can be expressed in terms of the cross section for transversely polarized photons:

$$\sigma^{L}_{\gamma^* p}(y, Q^2) = \frac{Q^2}{m_V^2} \sigma^{T}_{\gamma^* p}(y, Q^2), \tag{2.73}$$

which shall be used later in the discussion of the results of this analysis.

3 ZEUS detector

ZEUS is a multipurpose detector aiming at a spatial coverage as complete as possible. The main components (see figure 4.1 on page 20) are a vertex detector, a central tracking detector, planar drift chambers in the forward (proton) and backward (positron) directions plus transition radiation detectors, all in a magnetic field of 1.43 T provided by a thin superconducting solenoid. These tracking devices are surrounded by a high resolution calorimeter. The magnetized iron yoke surrounding the calorimeter is instrumented for use as a backing calorimeter and muon detector. In the forward direction iron toroids and tracking chambers reinforce muon detection. To detect forward scattered protons, six silicon detector stations inserted into the beampipe act as a proton spectrometer. In the backward direction photon and electron detectors close to the beampipe serve as the luminosity monitor. Interesting physics occur at a rate of a few Hz while background from proton beam gas interactions has a much higher rate, on the order of 100 kHz. To filter the events, the ZEUS detector is furnished with a 3-level, staged trigger system.

The following sections describe those detector components in more detail that are used in this analysis. For a detailed description of all components see [86].

3.1 High resolution calorimeter

The ZEUS calorimeter [5, 26] is a sampling calorimeter made of layers of depleted uranium interleaved with plastic scintillator. By choosing the correct fraction of absorber to readout material, the calorimeter has the same response to electrons and hadrons, i.e it is a so called compensating calorimeter. The scintillator tiles form towers which are read out via wave length shifter bars, light guides, and two photomultipliers. The calorimeter is segmented longitudinally into an electromagnetic and one or two hadronic sections. The tower sizes are $5 \times 20\,cm^2$ in the electromagnetic section and $20 \times 20\,cm^2$ in the hadronic section. The calorimeter is divided into a forward[2] (FCAL), barrel (BCAL), and a rear (RCAL) part with a depth of 7, 5, and 4 absorption lengths, respectively. In the forward hemisphere the solid angle coverage corresponds to 99.8%, in the rear part it is 99.5%, the difference to 100% due to the openings for the beampipe. The polar angle coverage extends from 2.2° to 176.5° where 0° is the proton beam direction. The energy resolution is under testbeam conditions for electrons $\sigma_E/E = 0.18/\sqrt{E} \oplus 1\%$ (E in GeV) and for hadrons $\sigma_E/E = 0.35/\sqrt{E} \oplus 2\%$. The calorimeter also provides timing information. The time resolution depends on the energy deposition; for energies greater than $4.5\,GeV$ it is better than 1 ns.

3.2 ZEUS calorimeter first level trigger

The calorimeter first level trigger (CFLT) is designed to process events by applying pattern recognition algorithms and fast digital summation techniques in order to collect interesting physics events and to reduce background from interactions of the beams with the residual gas in the beampipe. The decisions are derived in a pipelined fashion every 96 ns, the time interval between consecutive bunch crossings in HERA.

The signal of each of the 12864 photomultipliers of the uranium calorimeter is split into an analog pipeline to the ZEUS readout system and a signal for the front end cards of the CFLT. Trigger sum cards combine those analog signals to 896 calorimeter trigger towers ($20 \times 20\,cm^2$). Each trigger tower is divided into an electromagnetic and a hadronic section. This analog information is shipped into the electronics housing next to the detector, in which all the detector DAQ systems reside. Trigger

---

[2]Direction of the proton beam.

encoder cards digitize the information of the trigger towers every 96 ns by two 8-bit flash ADCs with high and low gain.

The digitized information is processed by lookup tables to provide directional (e.g. transverse and missing energy) and regional (e.g. energy in trigger towers around the beampipe) trigger information. This information uses calibration constants preloaded into lookup tables as well. The calibration is done by comparing the trigger data with the information from the calorimeter gathered with the data readout chain. The resolution of the digitized trigger energies is 48.8 MeV and the dynamic range is 400 GeV. The noise from electronics and uranium fission is measured to be below 200 MeV. This allows trigger thresholds as low as 464 MeV, as being employed in the GFLT triggers used in this analysis (see section 11.6).

Adder cards combine the information from the trigger encoder cards to provide detailed and global information for every bunch crossing. It also applies pattern recognition algorithms to identify isolated electrons and muons. Each adder card is dedicated to a certain number of trigger towers. An additional set of lookup tables receiving 6-bit compressed scale information compares the energy deposition against six programmable thresholds and calculates the energy of each trigger tower on a 3 bit scale[3]. The adder cards process the data into quantities used by the global first level trigger.

The information from the different adder cards is shipped to the CFLT trigger processor which handles the communication with the ZEUS Global First Level Trigger (GFLT). Before sending the calorimeter trigger quantities to the GFLT the information of all adder cards is combined to form the final sums of global and regional quantities and counting the number of isolated particles. The quantities used in the trigger for the beampipe calorimeter can be found in table C.2 in appendix C.

A more detailed description of the calorimeter first level trigger system can be found elsewhere [75].

3.3 Central tracking detector and vertex detector

Of the tracking devices of ZEUS only the central tracking detector (CTD) and the vertex detector (VXD) are being used in this analysis. Both chambers operate in a solenoidal magnetic field of 1.43 T. Great care has been taken in the selection of the materials and the mechanical design for the inner tracking detectors to present as little dead material as possible for the calorimeters surrounding them.

The vertex detector is surrounding the beampipe at radii from 106.5 mm to 142.5 mm. It conists of 120 cells with 12 sense wires each. The wires run parallel to the beam axis. The chamber is filled with dimethylether which allows high spatial resolution of the particle tracks.

The CTD is a drift chamber surrounding the VXD. Its diameter is 1650 mm and its length is 2400 mm. The chamber consists of 72 cylindrical drift layers organised into 9 superlayers. Five of the superlayers have their wires parallel to the chamber axis, four superlayers have a small stereo angle of 5°. The total number of sense wires is 4608. The chamber is filled with a mixture of 85% argon, 8% CO_2, 7% ethane, and 0.8% ethanol [33]. The single track resolution in 1994 was 153 μm [32]. The resolution in transverse momentum is $\sigma(p_T)/p_T \approx \sqrt{(0.005 \cdot p_T)^2 + (0.016)^2}$ where p_T is in GeV. The single hit efficiency is greater than 95%.

The vertex resolution using the information from VXD and CTD is 4 mm in z and 1 mm in the xy plane.

---

[3]These so called threshold bits are denoted by the extension '_th' to the names of the calorimeter quantities. Where such threshold bits were used in the trigger for this analysis can be found in table C.2 in appendix C, where the definitions of the BPC GFLT trigger are listed.

3.4 Luminosity monitor

The luminosity monitor consists of two electromagnetic calorimeters, located in the HERA tunnel in the direction of the outgoing positrons. Photons leave the HERA proton beampipe through a beryllium-copper exit window at $z = -82\,m$, pass through a carbon filter at $z = -103\,m$ to shield against synchrotron radiation, and are detected by a lead scintillator sampling calorimeter at $z = -106\,m$. The calorimeter is 23 radiation lengths X_0 deep and has a position detector inserted after 4 X_0. Since the carbon filter did not shield completely against synchrotron radiation, some additional lead shielding has been installed during 1994, for details see [66].

The positron calorimeter consists of a lead scintillator sandwich calorimeter of thickness 21 X_0. At a depth of 7 X_0 a position detector is installed. The positron calorimeter is positioned at $z = -35\,m$ near the positron beampipe. The positrons coming from the interaction point have to pass through quadrupole and dipole magnets. Those magnets deflect positrons that are below nominal beam energy out of the beampipe onto the positron calorimeter. The acceptance in energy is therefore restricted to $E = 9.2 - 18.2\,GeV$ [57].

The luminosity measurement is based on the detection of ep bremsstrahlung events. The cross section for this process is known to high accuracy from QED given by the Bethe-Heitler formula. If the event rate can be determined accurately, a precise determination of the luminosity is possible. To be insensitive to the acceptance of the positron tagger, which is complicated by the trajectory of the charged particles through the HERA magnets, the luminosity determination is using the counting rate in the photon calorimeter alone. For this measurement a precise knowledge of the energy of the incoming photon is important.

The positron beamgas interactions have the same experimental signature. To subtract this background, the event rate for 'pilot' positron bunches is also determined. Pilot bunches are particle packets in HERA that have their respective partner bunch not filled such that there are no ep collisions occuring, when the particles traverse the ZEUS detector. This background rate is scaled by the current of particles in those bunches with respect to the bunches that participate in ep collisions and statistically subtracted.

4 Beampipe calorimeter

The beampipe calorimeter is located $3.055\,m$ from the interaction region of the ZEUS detector in the direction of the positrons, in front of the collimator C5 (seen from the interaction point, see figure 4.1). It is a small ($240\,mm \cdot 112\,mm \cdot 80\,mm$) tungsten silicon sampling calorimeter, designed to detect scattered positrons. Its nominal polar angle acceptance is $18.8 - 34.5\,mrad$. The detector is mounted next to the beampipe, on the inside of the HERA storage ring. Right in front of the calorimeter there is a steel and tungsten flange which has a total thickness of 2.8 radiation lengths and acts as the first layer of absorber of the BPC.

The front-end electronics reside within the box of the calorimeter at the beampipe. The readout system for triggering and digitization is located in the so called 'Rucksack', the housing of all the ZEUS electronics next to the detector.
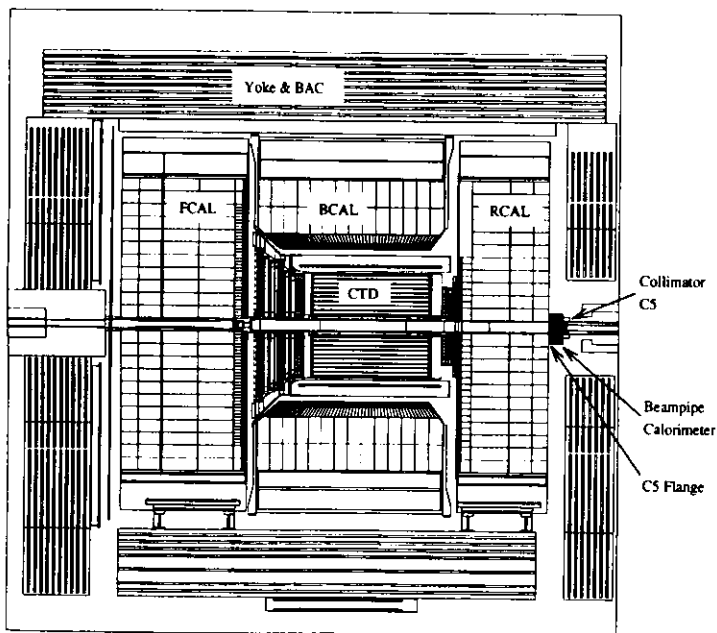
Figure 4.1: Location of the beampipe calorimeter within ZEUS

4.1 W-Si calorimeter

The calorimeter, its position detector and the associated electronics, are contained within a box of overall size $240\,mm \cdot 112\,mm$ (along the beampipe) $\cdot 80\,mm$. The bottom, top and side walls are made of aluminum, $5\,mm$ thick. The front face, where the particles enter, and the back side consist of $1\,mm$ copper.

As can be seen in figure 4.2, the calorimeter consists of 8 tungsten plates every $11\,mm$ interspersed
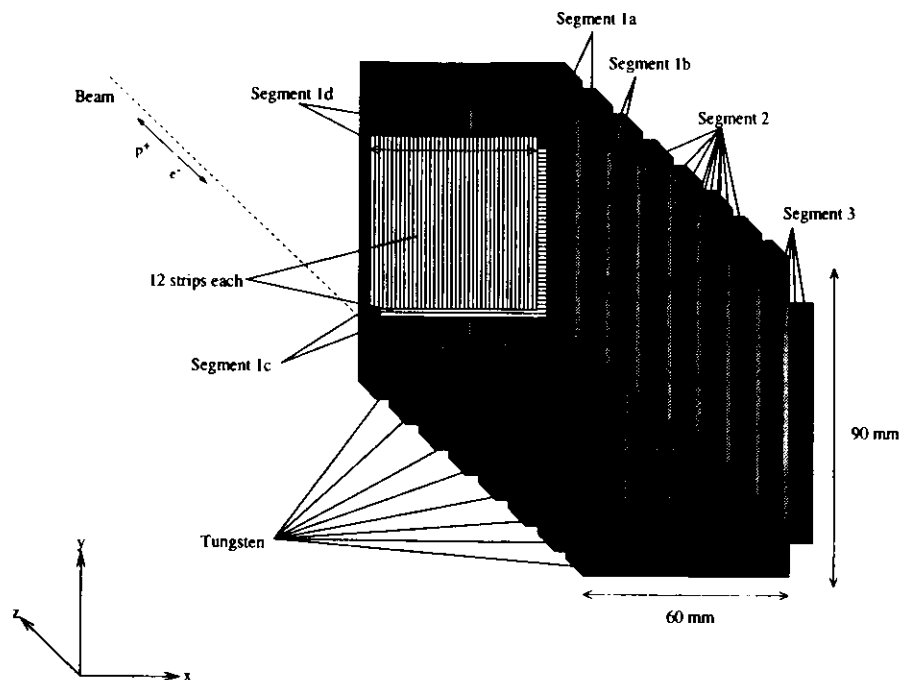
Figure 4.2: The calorimeter and the position detector. The tungsten absorbers are shown in light grey, the readout diodes in dark grey, and the position detector in white. Also indicated are the readout segments: the signals of a number of diodes are added together by analog circuitry. The ZEUS coordinate system is shown.

with silicon diodes. Each tungsten plate measures $90\,mm \cdot 60\,mm \cdot 7\,mm$. The thickness corresponds to two radiation lengths X_0.

The active layers for readout are located in between the tungsten plates and also in front of the first and behind the last one. Each active layer consists of four silicon diodes. They are the same diodes as are used in the Hadron Electron Seperator [86] of the ZEUS detector. Two diodes are mounted together on a ceramic card, which hosts preamplifiers and calibration capacitors as well.

The diodes have a thickness of $430\,\mu m$ and an active area of $29.6 \cdot 33.2\,mm^2$ [7]. The four diodes of each layer are placed next to each other, so that the total active area of the calorimeter is approx. $60 \cdot 60\,mm^2$. Due to the mounting, there is a small gap between adjacent diodes on the same ceramic card of $0.9\,mm$. The ceramic cards were mounted on a motherboard in such a way that the active areas of the diodes of different cards joined, see figure 4.3.

4.2 Position detector

To obtain information about the position of the incoming particles, two strip detectors (Hamamatsu S2461) are located in front of the first active layer of the calorimeter. The strip detectors are oriented at $90°$ with respect to each other. The first position detector has its strips vertically oriented, the
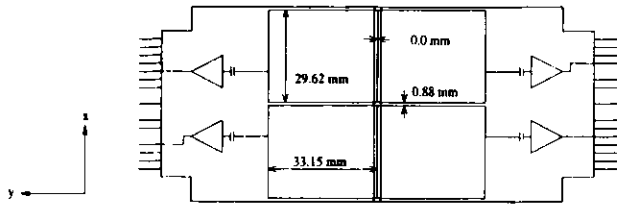
Figure 4.3: The diode cards in the calorimeter. The dimensions shown correspond to the active area of the diodes.

second one horizontally. Their active area is $48 \cdot 48\,mm^2$. The pitch is $1\,mm$. Due to a restriction in the number of output amplifiers, 4 adjacent strips are electrically connected in order to have 12 strips $4\,mm$ wide on each of the two position detectors.

4.3 Survey

The beampipe calorimeter has been surveyed at the end of the 1994 datataking period before being taken out. For that purpose two survey marks had been attached to the top of the BPC. The positions of these marks have been determined by triangulation with major survey marks on the CTD frustum. In figure 4.4 the location of the survey marks on top of the BPC can be found. The position of the strip detector and the calorimeter diodes with respect to these marks has been determined in the DESY machine shop with a three-dimensional survey machine. Adding the errors of the two surveys the overall error in the position of the BPC is $\delta = 1.5\,mm$.

The position of the geometrical center of the position detector in the ZEUS reference system is shown in table 4.1. The center of the calorimeter, as defined by the point were the corners of the four diodes of the diodes join, in ZEUS coordinates can be found in table 4.2. The offset between the position detector center and the calorimeter center is $\Delta_x = +3.1\,mm$ and $\Delta_y = -0.5\,mm$.

The BPC as being seen from the interaction area can be found in figure 4.5. The measurements as resulting from the survey have been marked.

Figure 4.4: Location of survey marks on the top side of BPC (distances in mm)

	[mm]
x:	81.4
y:	-3.1
z:	-3055.4

	[mm]
x:	84.5
y:	-3.6

Table 4.1: Position of the center of the strip detector in ZEUS coordinates

Table 4.2: Position of the center of the calorimeter in ZEUS coordinates
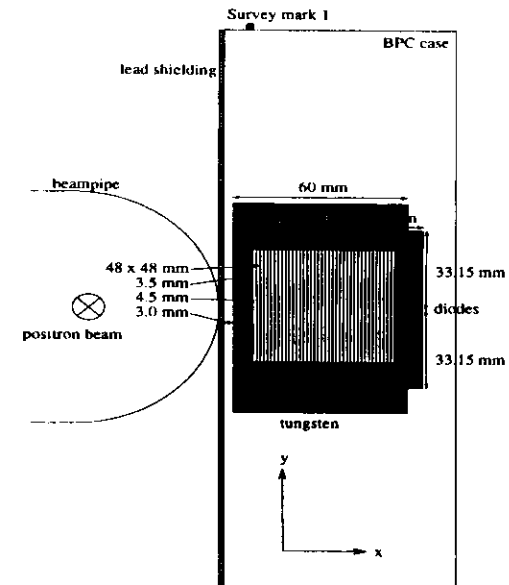
Figure 4.5: BPC seen from the interaction region, the different parts are shown in the same shades of grey as in figure 4.2

5   Readout electronics

A schematic diagram of the readout system can be found in figure 5.1. The signals from the front-end electronics in the BPC housing at the beampipe are transferred via 50 m twisted pair cables to the electronics housing of the ZEUS detector, the so called 'Rucksack'. There, cable receivers filter noise and amplify the signals. Their maximum is determined by a peak detector and stored in a sample & hold circuit until the global first level trigger (GFLT) of ZEUS has reached a decision to keep or discard an event. For the BPC to participate in this decision making process, a trigger signal derived by a constant fraction discriminator is provided to the GFLT. In case of a positive GFLT decision the stored signal is digitized by a 12-bit ADC. The digitized data is then shipped to the ZEUS event-builder (EVB) in case of a positive decision of the global second level trigger (GSLT). The readout system is controlled by a transputer system. The online data processing is done on that system as well and it is described in section 6.
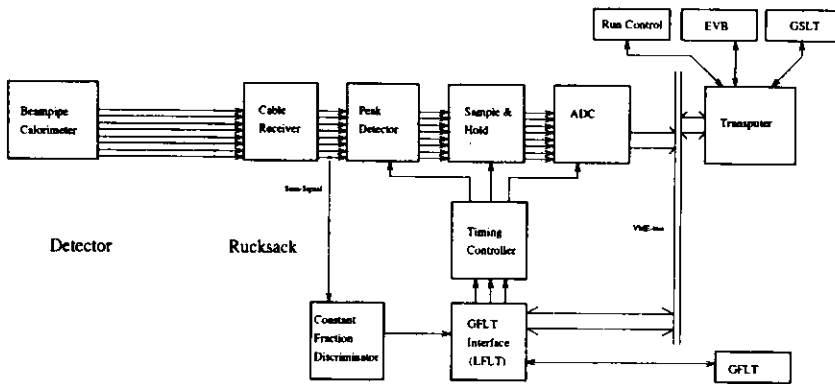
Figure 5.1: The readout chain (the components are explained in section 5.2)

5.1   Front-end electronics

The calorimeter box hosts all the necessary electronics to operate the calorimeter itself and the position detector. This includes power supplies, preamplifiers, analog sum amplifiers, cable drivers, and testpulser.

5.1.1   Readout amplifiers

The signals of the diodes are amplified by hybrid electronics on the ceramic cards carrying the diodes. These preamplified signals of a number of diodes are grouped into readout segments which form the different channels[4] of the calorimeter, see figure 4.2.

- Segment I: The first two diode layers, i.e. after zero and two radiation lengths X_0.

- Segment II: The 3rd, 4th, 5th, 6th and 7th diode layer. That corresponds to 4, 6, 8, 10 and 12 radiation lengths.

---
[4]The channel assignment can be found in appendix A.

- Segment III: The last two diode layers. Those diodes have 14 resp. 16 X_0 of absorber in front of them.

Segment I is laterally divided into four subsegments. Seen from the interaction point the subsegments are:

- Segment Ia: The two diodes in the upper right quadrant.

- Segment Ib: The two diodes in the lower right quadrant.

- Segment Ic: The two diodes in the lower left quadrant.

- Segment Id: The two diodes in the upper left quadrant.

The summing of the analog signals is done by transimpedance amplifiers CLC401 [9]. The preamplified signals of all diodes are added to derive an electronic analog sum signal. This signal is used to determine the energy which the particles deposit in the calorimeter. The outputs of the transimpedance amplifiers act as quasi-differential line drivers that ship the calorimeter signals via the 90Ω shielded twisted pair cables to the electronics in the Rucksack of ZEUS.

For the signals of the strips of the position detetcor MSD-2 amplifiers and matching line drivers are used to feed the signals over the twisted pair cables into the Rucksack electronics.

The connectors used and their pin assignment can be found in [55].

5.1.2   Test pulser

The testpulser is a custom design circuit for calibration purposes. It generates square wave pulses. The risetime is 50ns, the pulse duration 8 μs, with a falling edge of 500 ns. If a positive trigger signal is applied to the pulser input a single pulse will be generated. This trigger signal has to be $U_{Trig} > 2.0V$ and the width to be $T_{Trig} > 50ns$. The pulser will fire once for every incoming trigger.

The output voltage U, i.e. the pulse height of the test pulse, can be controlled by supplying an external reference voltage U_{ref} from the Rucksack.

The calibration for the testpulser is the following:

$$U = 52\frac{mV}{V}(6.0V - U_{ref}).\tag{5.1}$$

U is the voltage applied by the testpulser to the calibration capacitors on the diodecards in mV and U_{ref} is the reference voltage measured in V. This reference voltage is looped back to the rucksack for monitoring purposes.

5.1.3   Power supplies

The high voltage of -80 V for reverse biasing the diodes is supplied from the Rucksack and passively filtered at the BPC. All other voltages required by the calorimeter electronics are generated from ± 9 V which are externally provided by the electronics in the Rucksack. Power regulators 7805 and 7905 provide ± 5 V. Voltages of ± 4 V and -2 V are derived from these using the voltage drop across diodes.

The power regulators are mounted on the outside of the BPC case. This reduces the heat production on the inside, which is difficult to cool. Heating inside stems only from the inevitable power consumption of the amplifiers.

National Semiconductor LM35C temperature sensors are used for monitoring. They are sitting on the outside of the walls of the calorimeter box and on the beampipe. The sensor on the walls of the box is located near the heat sink of the voltage regulators. It therefore should sense the maximum temperature of the walls of the calorimeter box. The flange sensor is located on top of the beampipe near the top Si-PIN Diode used for background measurements [61]. This sensor should sense the temperature of the beampipe in the calorimeter region. The mean temperature of the calorimeter in operation is 40° C as measured by the box sensor.

5.1.4 Grounding and electrical shielding

Great care was taken in providing a single good ground for the electronics of the calorimeter. Low impedance paths are provided from every circuit board within the box to a certain ground point, which is directly connected with the ground line of the power line input.

The electronics are shielded inside the box by means of copper foil which is at the same potential as the power ground. The walls of the calorimeter box in contrast are isolated against the electronics in order to prevent induction of noise into the calorimeter electronics. If necessary, the box can be put to any desired potential by using certain lines of the connectors. To be safe against electronics oscillation, the calorimeter case was put to ground potential. The walls of the box are isolated from the beampipe support as well.

5.2 Electronics in the Rucksack

The readout chain in the Rucksack consists of the following parts: cable receiver (filter and amplifier), peakdetector, sample & hold circuit and ADC. There is also a path for trigger data consisting of a constant fraction discriminator, an interface to the ZEUS Global First Level Trigger (GFLT), and a timing controller. The readout system is under control of a transputer system which interfaces with the ZEUS Event-Builder (EVB), ZEUS Global Second Level Trigger (GSLT) and Run Control. A schematic overview can be found in figure 5.1.

This readout system is located in the Rucksack rack C-3-9. Transputer, ADC, sample & hold circuit, timing controller, and the interface with GFLT reside in a VME crate. Cable receiver, discriminator, and peak detector are housed in a NIM crate.

5.2.1 Cable receiver

The signals of the beampipe calorimeter front-end electronics are brought via two 90Ω shielded twisted pair cables into the Rucksack to the cable receivers. Inside the cable receiver the signals are filtered by a high frequency transformer, which blocks low frequency noise and high frequency transients. After that the signals are amplified. The differential video amplifier LM733 used here allows to set the gain by means of a jumper. Values in the range of 10 to 400 are selectable. Both outputs of these amplifiers (inverted and non inverted) are buffered by a fast LH0002 amplifier. The circuit diagram can be found in figure 5.2.

5.2.2 Trigger and interface to the GFLT

In order to derive a trigger decision and timing information for the ZEUS Global First Level Trigger (GFLT) and the control circuits of the peakdetector and the sample & hold circuit, the analog sum signal of the calorimeter is fed into a constant fraction discriminator, which provides an accurate
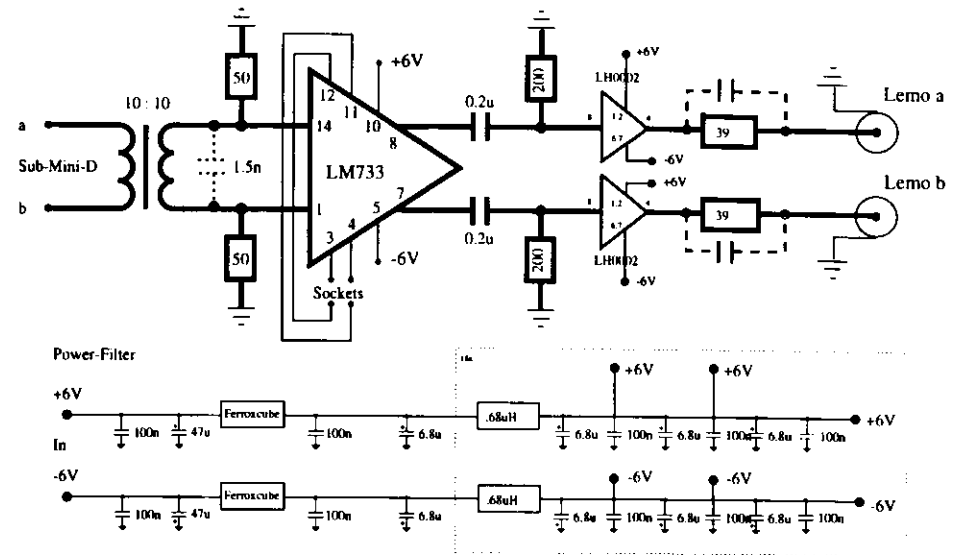
Figure 5.2: Cable receiver circuit diagram

timing independent of the signal height. In order to not disturb the analog signal, the sum signal for the trigger is taken from the inverted output of the cable receiver which has its own output driver.

The intrinsic timing resolution of the calorimeter is 1.8 ns. The discriminator is a Canberra Model 2126, with a much better timing resolution. If a certain adjustable threshold is surpassed, a trigger signal is passed to an interface to the GFLT. This interface called LFLT (Local First Level Trigger) exchanges trigger information for every HERA bunch crossing with the GFLT. The data exchange between GFLT and LFLT is done according to [77]. The LFLT contains a TDC to compute timing information for the GFLT with a timing resolution of 5 ns. A finite state machine handles the different trigger situations. It has also access to the VME-bus and can issue interrupt requests to the transputer system to inform the readout software about the occurence of local or ZEUS wide triggers. For more details see [79].

The trigger signal is passed by the LFLT to a custom design timing controller circuit, see figure 5.3. This timing controller derives the signals necessary to control peak detector, sample & hold circuit, and ADC. All signals of LFLT and timing controller use ECL logic.

The beampipe calorimeter readout system does not use pipelines for the data. Only data of one event can be stored in the sample & hold circuit. The HERA bunch crossing number for the data in the sample & hold circuit is stored in the LFLT. In case the GFLT sends a positive trigger decision, the bunch crossing number of the stored data is compared to the trigger decision's bunch crossing number. If no matching trigger decision reaches the LFLT within a certain timeout period (software adjustable, should be the GFLT decision time, currently 46 bunch crossings) the sample & hold circuit is cleared.

If the constant fraction discriminator has issued a trigger, the LFLT will inhibit any further triggers to the timing controller until the GFLT derives a positive decision or the timeout occurs. Up to that moment all other triggers coming from the discriminator are blocked in order not to corrupt the already sampled data. This particular choice of readout scheme introduces a deadtime of 4.4 μs, the
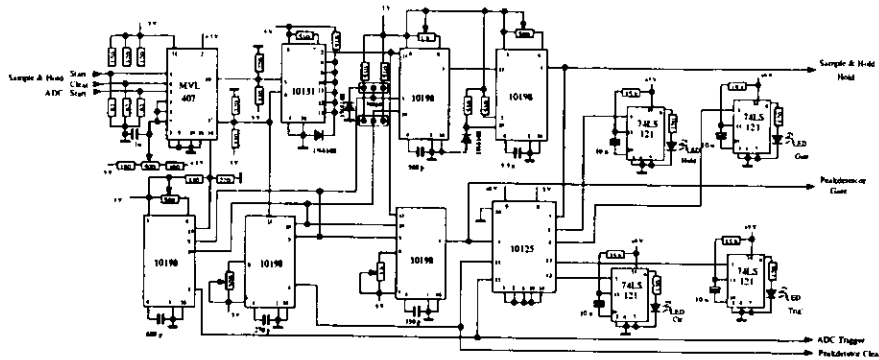
Figure 5.3: Timing controller of the beampipe calorimeter readout chain

time it takes the GFLT for its trigger decision. In case of a positive trigger decision for which the bunch crossing numbers match, the ADC will be started. Its conversion time of $10\,\mu s$ per channel plus an extra $10\,\mu s$ for internal timing, has to be added to the BPC deadtime for that event, giving a total of $334.4\,\mu s$.

All positive GFLT triggers are passed to the BPC readout software by issuing an interrupt request. If the sample & hold circuit is filled but with data not corresponding to the bunch crossing of the GFLT decision, that decision gets a special flag[5], which is put into the data stream to the event-builder. By using this flag in the offline analysis it is possible to monitor the total deadtime of the BPC. The buffering that is necessary to prevent that the BPC readout software misses a trigger decision while busy with other tasks, e.g. serving an interrupt request of the ADC, is done by means of a FIFO buffer for trigger decisions on the LFLT board. For more details see [79].

5.2.3 Peak detector

The second stage in the readout chain is a custom design peak detector facilitating CLC400 transimpedance amplifiers. It detects the peak value of the calorimeter signal and holds it for a few μs until the following stage has sampled the signal. The electronics is mounted in NIM cassettes. A circuit diagram can be found in figures 5.4 and 5.5.

5.2.4 Sample & hold circuit

The third stage, housed in the VME crate, is based on a commercial sample and hold circuit, the Analog Devices AD684. This integrated circuit can hold the stored value until a trigger decision has been formed and the ADC has digitized the data. Over this time period of 335 μs there is virtually no drop of the analog signal. For the circuit diagram see figure 5.6.

5.2.5 Analog to digital converter

After a positive decision from the Global First Level Trigger, the signals enter an ADC, a Xycom XVME566. This is a VME based 32 channel, 12 bit commercial ADC with a conversion time of $10\mu s$ per channel.

---

[5]In the LFLT status word.
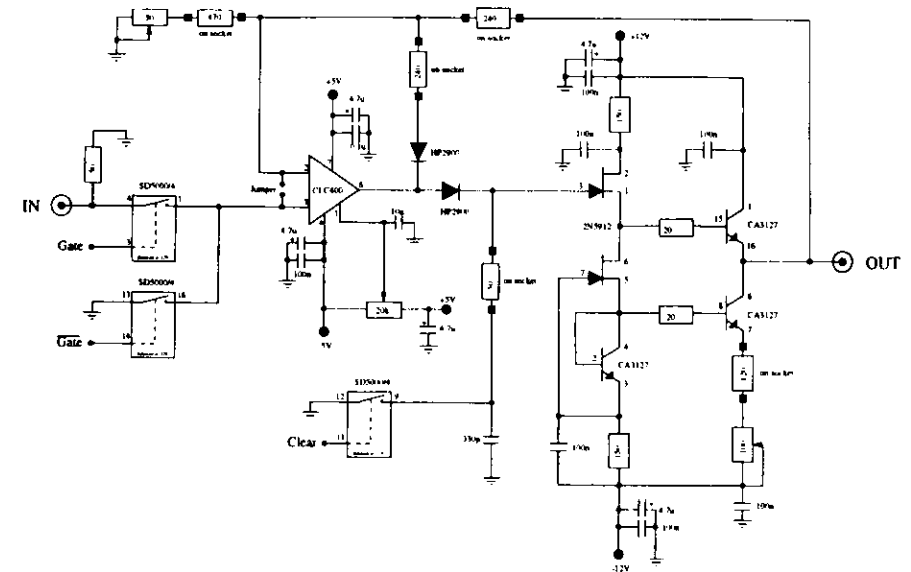
Figure 5.4: Peak detector circuit diagram

5.2.6 Power supplies

All power supplies necessary to operate the beampipe calorimeter are located in the Rucksack. The power cables have a cross-section of $3 \times 2.5 mm^2$. To account for resistive losses over the 30 m of cable to the calorimeter, the setting for nominal $+9.0\,V$ at the calorimeter is $+9.4$ V at the power supply, and -9.2 V for nominal -9.0 V. The current drawn is 1.0 A (+9 V) and 0.8 A (-9 V).

The diode cards require for their operation $\pm\,9\,V$, all other required voltages are deduced from these inside the calorimeter box, see section 5.1.3.

The bias voltage to drive the diodes into depletion is provided by a medium voltage power supply. The setting used is -80 V. The current is small, approx. $300\mu A$.
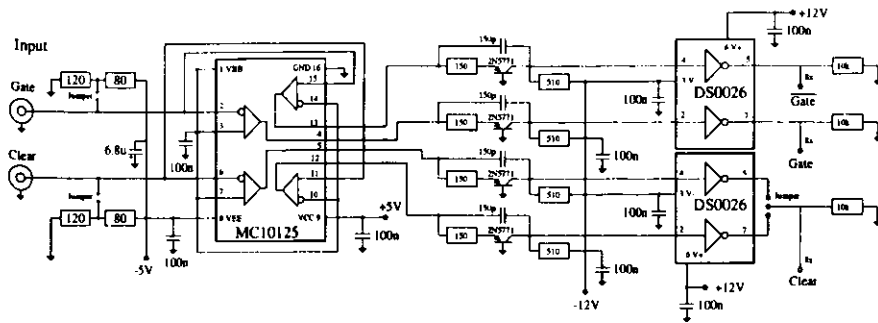
Figure 5.5: Control circuit diagram of the peak detector
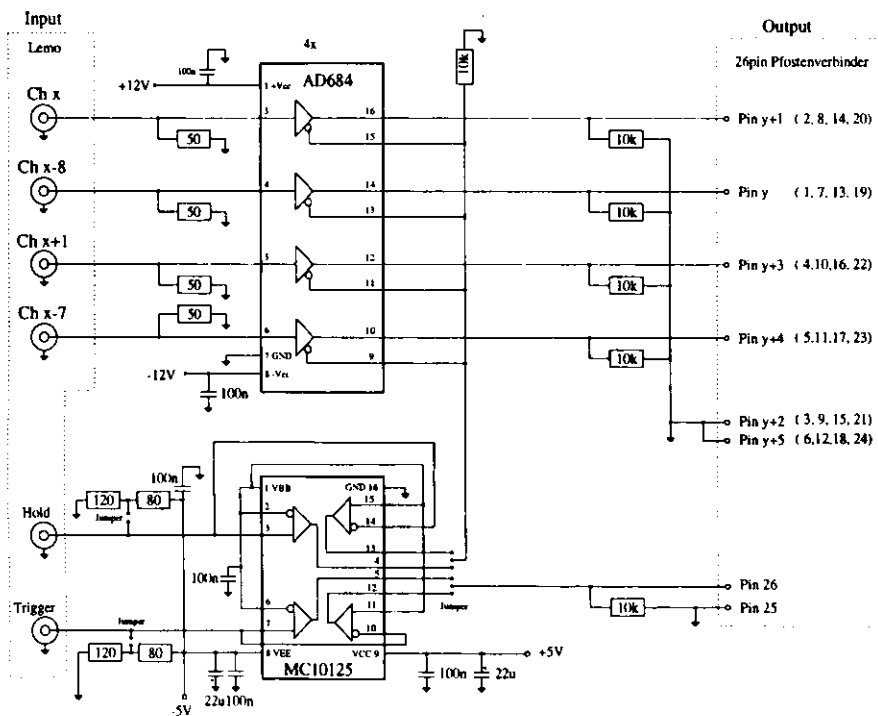
Figure 5.6: Sample and hold circuit diagram

6 Software of the beampipe calorimeter

The online software of the beampipe calorimeter does all the tasks necessary to get the signals of the calorimeter into the ZEUS data stream.

A schematic overview, the functional model, of the readout software can be found in figure 6.1. The system is event driven. In case data occurs from the ADC or the local trigger interface (LFLT) the interrupt server will send the information to the internal data storage. The data there are processed by a data mamanger which will finally ship the data to the ZEUS event-builder (EVB) in case that the global second level trigger (GSLT) has accepted the event. Separate from this data handling, a local run control tasks steers the operation of the hard- and software. It communicates with the outside world via a UNIX workstation (calec.desy.de). The outside world for the beampipe calorimeter are the ZEUS overall run control and human experts. The communication tasks on the workstation are described in section 6.7.
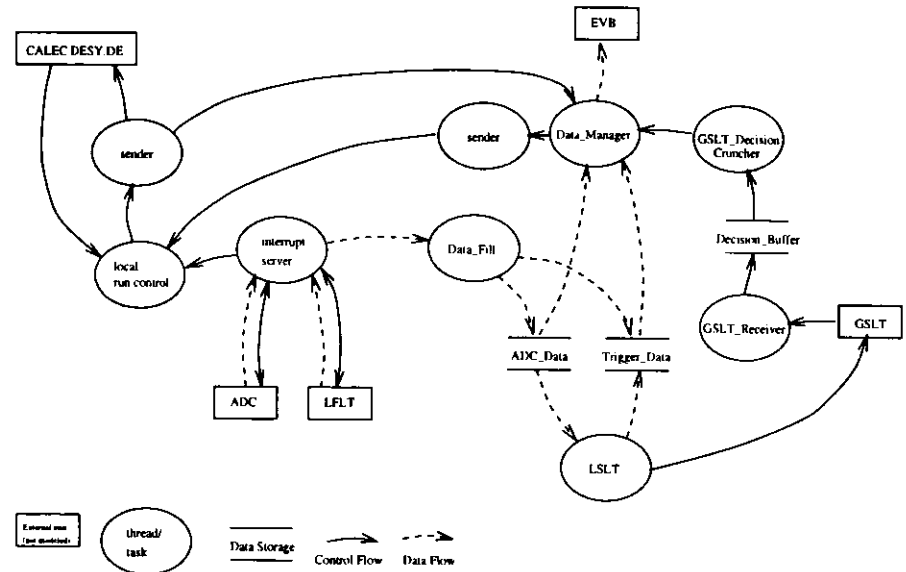
Figure 6.1: Functional model of the beampipe calorimeter readout software

The readout software runs on the Y transputer of a NIKHEF two transputer board [38]. Those transputers are INMOS T800, with 4MB of dynamic memory, access to 128KByte triple ported memory, which is the interface to the ZEUS event-builder, and access to the hosting VMEbus [13].

The software has been written in Parallel C (e.g. [20]), which is an extension of the ANSI C standard to make use of the features specific to transputers.

Since the transputer has a scheduler, dispatcher and timer already integrated into the processor's hardware, there can be several processes running in quasi-parallel without any need for an operating system. Another important feature is the hardware support for fast serial communications. On four bidirectional links on the T800 data can be transfered at speeds of 20 *Mbits/s* to other processors. It is possible as well to create such links between processes on the same processor, which will communicate

through memory addresses.

6.1 Software configuration

Parallel C supports two types of processes, tasks and threads. Tasks are fully self contained, linked with their own copy of library routines and can be handled by the task configurer. This configurer is a program that comes with the software development system and puts one or more tasks according to a configuration file into one bootable file. The configuration file includes information on how to assign the memory to the different tasks. The location of the stack and/or heap of tasks can be choosen to reside either in fast processor RAM (4k) or in the dynamic RAM. The bootfile is loaded into the transputer and executed on booting. In case of the beampipe calorimeter, this booting is done by the server process BC_server (see section 6.5) on CALEC.DESY.DE, a Silicon Graphics workstation running UNIX, see figure 6.2.

Each task can dynamically create other processes, which are then called threads. These threads share their heap area and static variables with the creating task on the memory area that has been assigned by the configurer. They also share the library routines with the creating task. Besides this sharing of the memory, threads behave the same as tasks. Therefore they are able to create more threads on their own.

6.2 Process scheduling

Tasks and threads can run at high ('urgent') or low ('non urgent') priority. Urgent priority means, that this process runs uninterrupted until it deschedules itself by waiting for some input or output on one of its links or by an explicit descheduling instruction. Non urgent processes on the other hand will be interrupted immediately if some other process with high priority is ready to execute. If the non urgent process has been executing for a certain time, around 2 ms, it will be descheduled by the processor scheduler. Another process that is ready will then be executed instead. By doing so the processor time is time sliced between non urgent processes while urgent processes execute immediately[6] and uninterrupted. More details can be found in [47].

6.3 Functional model

In the following the different tasks and threads that compose the readout software of the beampipe calorimeter are being described. The source for all the processes can be found in ˜beam/src/beam on CALEC.DESY.DE. The corresponding header files are located in ˜beam/src/global. All source and header code is well documented and the reader is encouraged to consult those files for details not covered here.

There are three tasks which compose the readout software. The only path of information exchange between these is implemented by message exchange over the links. The format of these messages can be found in the header file ˜beam/src/global/link_messages.h. By doing so, it is very simple to reconfigure the software for multiprocessor systems without rewriting any code.

The tasks are the interrupt server, running at high priority with its stack located in the fast processor RAM, the local Run Control running at low priority, and the Data_Manager task. The latter task encompasses many threads running at low priorities, with the exception of the threads receiving the decisions of the Global Second Level Trigger (GSLT) running at high priority.

---

[6]If more than one urgent process is ready for execution, they will be queued. The next process in the queue will become active if the preceeding high priority process deschedules itself.

The functional model of the beampipe calorimeter readout, which shows the different tasks and threads, can be found in figure 6.1.

6.4 Interrupt server

The interrupt server takes care of all the hardware requests of the beampipe calorimeter readout. It is a task running at high priority with its stack residing in the fast on-processor memory. As soon as an interrupt occurs, any low priority process will be descheduled. All other processes of the beampipe calorimeter readout except the threads handling the decisions of the GSLT[7] are running at low priority.

Two sources of interrupt requests exist: the LFLT which interfaces with the GFLT and the ADC for digitizing the signals. Only after all their interrupt requests have been serviced the interrupt server will deschedule and allow other processes to resume.

6.4.1 Serving the ADC

If the ADC requests some service, it is first checked whether it is a valid service request, i e. end of a sequence of conversions. If that is the case, the data of all the channels on which a conversion has been performed are read out. That information is then put into a message and sent via a link to the data_fill thread in the data_manager task. After that has been accomplished, the ADC is being made ready for the next conversion by resetting the adequate bits in the status register of the ADC. Finally the state machine on the LFLT (see section 5.2.2) is informed, that the ADC is ready again.

After the bits in the transputer status register which handle the VME bus interrupts are reset, the interrupt server is ready again for new requests.

6.4.2 Serving the LFLT

The LFLT, interfacing with the Global First Level Trigger (GFLT), does all the necessary timing handling between the BPC readout, which does not have a pipeline, and the GFLT. It can request interrupts in six different situations:

1. The GFLT has sent an ACCEPT for a bunch crossing, when there was no trigger pending from the BPC.

2. The BPC had a trigger pending for which no ACCEPT occured within a certain timeout period. Currently the GFLT will issue an ACCEPT exactly 46 bunch crossings after the interaction had taken place. Since these triggers have been rejected by the GFLT this interrupt source is masked out in the LFLT interrupt mask register.

3. There was a pending trigger and an ACCEPT occured within 46 bunch crossings, but the bunch crossing numbers of the trigger and the ACCEPT did not match.

4. There has been a trigger and a matching ACCEPT. In this case the ADC will be triggered by the LFLT to start converting data.

5. While the ADC is converting data of another event, an ACCEPT has occured. Naturally there is no data for this event available from the BPC.

---

[7]The thread receiving the decisions of the GSLT and putting them into a buffer is requested to run at high priority in order not to block ZEUS during data taking. Due to the library structure the thread reading from this buffer has to run at high priority as well. These processes can't be descheduled before they have completed. Since they do not do extensive computations, actually they just put into or read from the buffer the GSLT decision, this does not introduce much latency into the interrupt serving. More details can be found in section 6.6.

6. There has been an ABORT request from the Fast Clear of the ZEUS trigger system. ABORTs are treated by the BPC readout system as extra triggers. The ABORT may occur after the readout system has already started converting data, and therefore the event is already in the data buffers. The only chance to handle the event properly is the data_manager to detect it by finding two triggers with the same GFLT number when processing the data in the software buffers.

The different interrupt request sources are enabled by means of an interrupt mask register, which is set during the LFLT initialisation. This is done during setup of a run.

If the LFLT requests an interrupt, the status of the FIFO is being checked by software during servicing. The FIFO can contain up to 512 entries of GFLT number, GFLT system- and user-readout data and ambiguity range from the GFLT as well as a bit indicating whether the ADC had been started for the corresponding GFLT number. As long as there are data in the FIFO, the content of the FIFO and a trigger counter[8] and the status bits of the LFLT[9] are being sent as a message to the data_fill thread in the data_manager task. After the FIFO has been emptied, the interrupt request bits of the LFLT are reset.

After having reset the bits in the transputer status register which handle the VME bus interrupts, the interrupt server is ready again to handle new interrupts.

6.5 Local run control task

Local run control is the interface between all the tasks of the transputer to the BC_server on CALEC and through that to ZEUS Central Run Control (RCC) and any user, see figures 6.1 and 6.2.

The local run control task listens to messages on any of its inputs links. Those inputs are software links to the interrupt server and the data manager as well as the hardware link from CALEC. All messages are decoded and the necessary action taken. For messages originating from the interrupt server or the data manager this means forwarding of the message or the data. Messages from the BC_server, and through that server from users or RCC, are forwarded to the appropiate task, e.g. 'debug on' command, or the action is taken by local run control itself, e.g. 'activate'.

In order to circumvent the problem of deadlocks[10], local run control sends out messages through an extra thread, called 'sender'[11]. Messages that should be sent out over a link are put into a ring buffer accompanied by information of which link to use. The sender thread works independently from local run control, i.e. if one link is temporarly blocked, local run control can still continue to operate.

6.6 Data manager task

The data manager task is the most complex piece of the beampipe calorimeter software. The processes are grouped around two ring buffers which store the ADC and trigger information. The task encompasses six threads: the data manager itself with an accompanying sender thread, a thread putting the data from the ADC and the LFLT into the buffers (data_fill) and a local second level trigger (LSLT) which performs some calculations on the buffered data and forwards this information to the Global Second Level Trigger (GSLT)[12]. The remaining two threads handle the decisions coming from the

---

[8]This is a hardware counter on the LFLT board that counts all triggers of the BPC constant fraction discriminator regardless whether being accepted by the GFLT or not.

[9]The status bits contain information about the source of the interrupt and the status of the FIFO.

[10]Consider the case when both local run control and BC_server want to send messages at the same time to each other; they would be descheduled indefinetely since their respective adressee is not listening.

[11]The source code can be found in ~beam/src/beam/output.c

[12]In 1994 the BPC data was not used in the GSLT

GSLT whether an event has become accepted. The thread gslt_receiver is by request of the GSLT running at high priority and puts the information into a small ring buffer. The decisions are read from the buffer by a high priority thread gslt_decision_cruncher and sent to the data_manager task running at low priority, which then takes the appropriate action. This extra high priority process is necessary since simultaneous access by high and low priority processes to the buffer could corrupt the control structures[13] of the ring buffer.

If the event has been accepted by the GSLT, the data is ADAMO'ized[14] and shipped to the event-builder. This is done by means of the triple ported memory to save links. The second transputer on the 2TP board is used by the event-builder system to read the beampipe calorimeter data from the triple ported memory and transfer the data over links to the ZEUS Third Level Trigger. The data to the ZEUS event-builder has to be in ZEBRA exchange format; for a description of the dataflow format and the communication protocol see [11, 10].

For a description of the threads within the Data Manager task, please refer to [55]

6.7 Run control interface of the beampipe calorimeter

The general run sequencing of ZEUS is done centrally by ZEUS run control (RCC). The BPC readout system is controlled by a transputer which neither has a mass storage device nor a network connection. The transputer mass storage and booting is facilitated by a UNIX workstation CALEC.DESY.DE, which has network access as well. The model of the software written in ANSI C can be found in figure 6.2.

On CALEC there is one process servicing the needs of the beampipe transputer, called BC_server. This software is hooked up to the tranputer link with the front end local run control task. The connection between CALEC and Central Run Control (RCC) of ZEUS is done via Ethernet using TCP/IP. The message handling between RCC and BC_server is facilitated by the process BC_rcc. This is necessary since the message handling of ZEUS RCC in 1994 (see [63]) did not provide the tools to log into servers.

The structure of these tasks is described in detail in [55]. There one also finds a description on how the interaction with users is organized and what commands are understood by the BPC.

---

[13]Threads accessing a given semaphore using routines of the run time library must run at the same priority.

[14]The format can be found in ~beam/src/global/adamo_tables.h
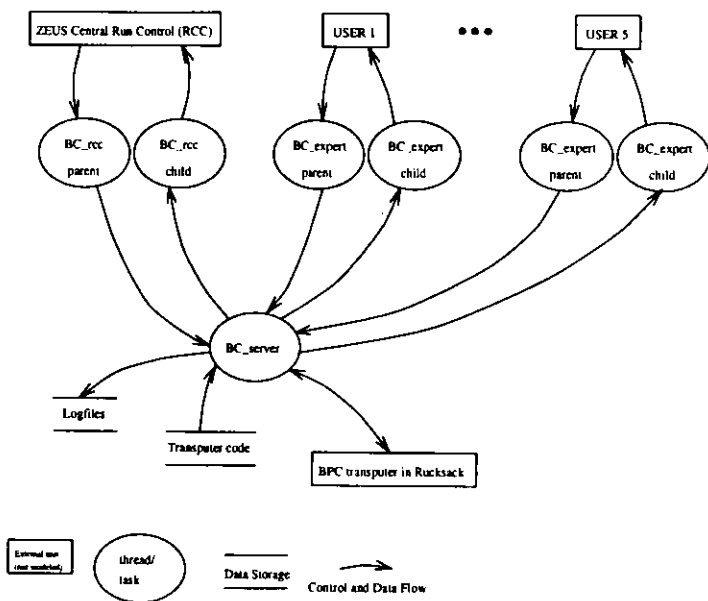
Figure 6.2: Model of the BPC server software on the UNIX workstation CALEC.DESY.DE. This software handles the communication between ZEUS central run control and up to 5 users on one side and the transputer system of the readout system on the other side. It alsoe provides means for archiving information in logfiles.

7 Testbeam measurements

The beampipe calorimeter has been exposed twice to electrons of $1\ldots5\,GeV$ in the DESY testbeams. The first exposure was carried out November 1991 in testbeam 21, when the assembly of the calorimeter itself was finished, and the second one in November 1993 in testbeam 24 after two years of operation. The 1991 testbeam measurements are used for determination of the energy resolution. The 1993 exposure, after the beampipe calorimeter had been in operation for two years, showed some sign of performance deterioration [40] which eventually led to the replacement of the complete calorimeter electronics (diodes and readout) and position detector readout. In the 1991 testbeam exposure the position detector readout had not been installed yet, therefore the 1993 measurement is used for the determination of the strip detector performance.

7.1 Testbeam 21

The testbeam 21 used for calibration purposes uses the DESY II electron synchrotron. A carbon filament in the halo of the beam is used to produce γ-quanta. Those quanta traverse the DESY III proton synchrotron that is in the same horizontal plane as the electron synchrotron. Then they are converted back to electrons and positrons using a copper conversion target. A dipole magnet is used to sort the particles (and antiparticles) for momenta. Passing a beamshutter, the electrons enter the testbeam area via a lead collimator. This setup is shown in figure 7.1. The trigger system consists of a beam definition system, two finger counters and a veto. The beam definition uses three paddles of scintillator at angles of 90° with respect to each other. They were located at the entry of the electrons into the testbeam area. The finger counters are placed in front of the beampipe calorimeter, defining a cross section of $5\times5\,mm^2$. The veto counter is a large area scintillator with a central cutout of $15\times15\,mm^2$.

The energy resolution of the beam has been estimated in [9] to

$$\frac{\sigma_E}{E}<5\%. \tag{7.1}$$
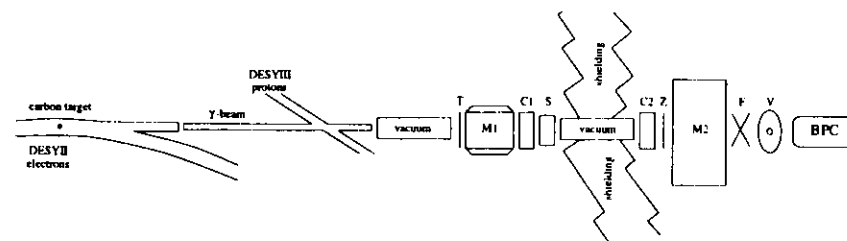
Figure 7.1: Schematic drawing of the DESY testbeam 21. The symbols denote the following:

T	=	conversion target	M1	=	momentum selecting magnet
C1,C2	=	collimators	S	=	beam shutter
Z	=	trigger counters	M2	=	magnet for experiments
F	=	finger trigger counters	V	=	veto counter
BPC	=	beampipe calorimeter			

7.2 Testbeam 24

The testbeam 24 uses a different setup than testbeam 21. In between the dipole magnet and the beamshutter, a second dipole magnet is inserted. This acts as a momentum filter on the secondary electrons. Except for this difference, the testbeam setup is identical.

The beam profile of the testbeam has been measured by varying the position of the finger counters. The relative rate of the finger counters with respect to the beam definition counters can be found in figure 7.2. Gaussians have been fitted to the data.

The width of the testbeam is

$$\sigma_{beam} = \sqrt{\sigma_{measured}^2 - \sigma_{finger\ counters}^2} \tag{7.2}$$

Using the result from the fit, one obtains the testbeam width:

$$\sigma_x = 7.5\,mm \tag{7.3}$$

$$\sigma_y = 8.0\,mm. \tag{7.4}$$

This shows that the beam is wider than the trigger counters of $5 \times 5\ mm^2$. Therefore the beam electron position is known with an rms error of

$$\sigma = \frac{5\,mm}{\sqrt{12}} = 1.44\,mm \tag{7.5}$$
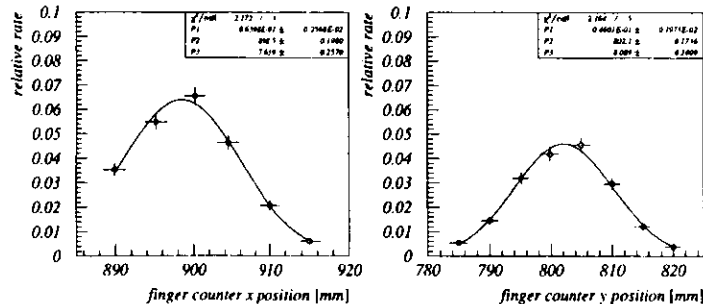
Figure 7.2: Profiles of the DESY testbeam 24 at $E = 3.7\,GeV$

7.3 Linearity and energy resolution of the beampipe calorimeter in the testbeam

The determination of the energy resolution uses the analog sum channel, since this is the one which is used in the energy measurement. The resolution has been determined by electrons of $1–6\,GeV$ and with $4\,cm$ of iron in front of the calorimeter.

The readout system used in the ZEUS datataking did not exist at that time, instead a CAMAC based charge integrating ADC read out by a Motorola VME147 computer had been used. The electronics of the BPC are designed to deliver voltage driven signals. Using the charge integrated signal introduces some nonlinearities in the signal. These nonlinearities can be seen in figure 7.3. Since the testpulser internal to the beampipe calorimeter was not operational yet, an external pulse generator is used. A polynomial of second order has been fitted to the data:
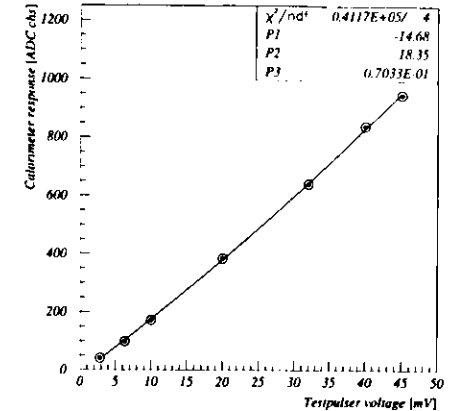
Figure 7.3: Response of the BPC to charge injection in the 1991 testbeam exposure

$$ADC = P_1 + P_2 \cdot U_{Testpulser} + P_3 \cdot U_{Testpulser}^2. \tag{7.6}$$

Inverting this relationship allows to get the calorimeter response free of nonlinearities from the electronics. The corrected data of the sum signal is fitted by a Gaussian for each testbeam energy. The average response U plotted versus testbeam energy E for the case with no absorber in front can be found in figure 7.4. The signal shows a linear behaviour as can be seen by a linear fit:

$$f(E) = P_1 + P_2 \cdot E. \tag{7.7}$$

The relative deviation δ from the fitted line is shown in figure 7.5 and is 1% of the signal at most:

$$\delta = \frac{U - (P_1 + P_2 \cdot E)}{U}. \tag{7.8}$$

The energy resolution is defined by

$$R = \frac{\sigma_U}{U}, \tag{7.9}$$

where U is the corrected energy response and σ_U the width of a Gaussian fitted to the corrected energy response. The energy resolution obtained in testbeam 21 for energies of $1\cdot6\,GeV$ is plotted in figure 7.8. To account for signal broadening by electronics noise and the energy resolution of the testbeam an error of 3 % has been subtracted quadratically. The errors are estimated by allowing the energy resolution of the testbeam to be different by $\pm2\,\%$. The following function was used to parametrize the energy resolution:

$$R = \frac{P_1}{\sqrt{E}} + P_2, \tag{7.10}$$
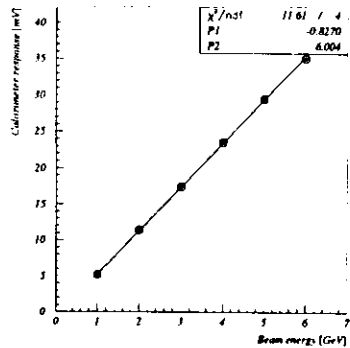
Figure 7.4: Corrected energy response of the BPC with no absorber in front in testbeam 21
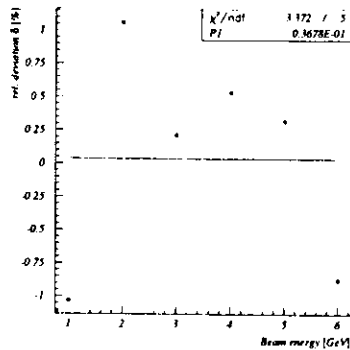
Figure 7.5: Relative deviation of the corrected energy response from the linear fit in figure 7.4 in per cent of the signal with no absorber in front of the BPC.

Figure 7.6: Corrected energy response of the BPC with 4 cm iron absorber in front in testbeam 21
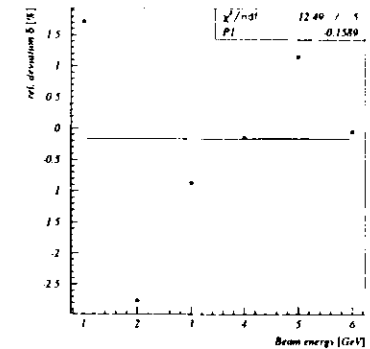
Figure 7.7: Relative deviation of the corrected energy response from the linear fit in figure 7.6 in per cent of the signal with 4 cm iron absorber in front in testbeam 21.

where E is the beam energy in GeV.

The analysis has been done for the calorimeter with 4 cm of iron simulating the C5 flange in front of the beampipe calorimeter as well. The corresponding plots can be found in figure 7.6, figure 7.7, and figure 7.9.

The results of the fits of the energy response and the energy resolution can be found in table 7.1.

	no absorber	4 cm iron absorber
energy response	$U = -0.8 + 6.0 \cdot E$	$U = -1.5 + 5.7 \cdot E$
energy resolution	$R = \dfrac{26.4\%}{\sqrt{E}} + 1.3\%$	$R = \dfrac{29.5\%}{\sqrt{E}} + 1.8\%$

Table 7.1: Fit results for calorimeter energy response and resolution in testbeam exposures with and without absorber. The energy response U is given in mV, the energy resolution R in %.

When taking the flange of the beampipe in front of the BPC into account[15], the energy resolution of the beampipe calorimeter in the testbeam is:

$$\frac{\sigma_E}{E} = \frac{29.5\%}{\sqrt{E}} + 1.8\%, \tag{7.11}$$

where E is measured in GeV.

7.4 Position scans

The energy response of the beampipe calorimeter in ADC counts is shown in figure 7.10 for a scan in x and in figure 7.11 for a scan in y. Both figures show a dip at the center of the calorimeter due to the gap between the diodes, which were present for y and x in the testbeam exposure. The dip in y should be much smaller in the 1994 data, since the diodes have been mounted in such a way when being replaced that there is less spacing between the diodes in y.

These scans can be directly compared with the 1991 scans in testbeam 21, see [9]. They both agree well. They can also be compared with the results from Monte Carlo simulations in section 10.1. For this comparison one has to bear in mind that that particular Monte Carlo study assumed perfect position reconstruction. The dips in the testbeam and ZEUS data are more shallow and wider due to position smearing.

To keep the error on the measured energy due to the hit position within the limit set by the energy resolution at beam energy $\sigma_E/E = 5.6\%$ fiducial cuts are necessary. Staying within 10 mm of the diode boundaries ensures this.

---

[15]By using 4 cm iron in the testbeam.
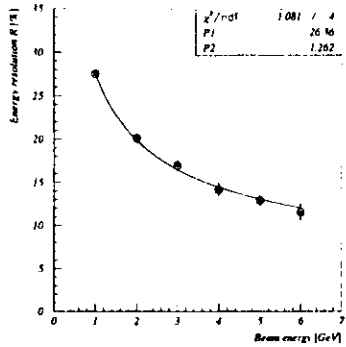
Figure 7.8: Energy resolution of the BPC with no absorber in front
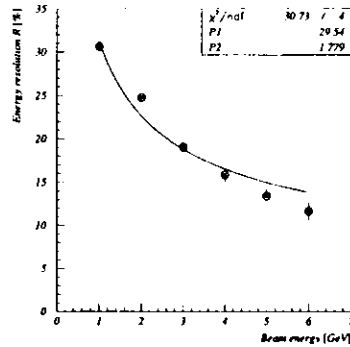
Figure 7.9: Energy resolution of the BPC with 4 cm iron absorber in front
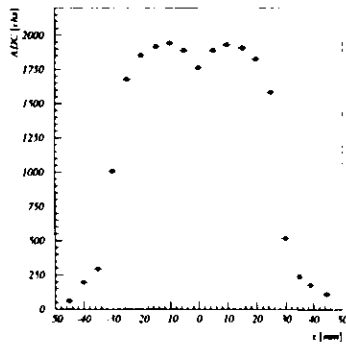
Figure 7.10: Energy response in x with 4 cm iron absorber in front in testbeam 24 ($x = 0\,mm\dot{=}$ center of the calorimeter)
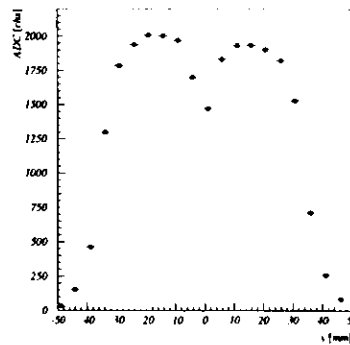
Figure 7.11: Energy response in y with 4 cm iron absorber in front in testbeam 24 ($y = 0\,mm\dot{=}$ center of the calorimeter)

8 Position reconstruction

In order to understand the position reconstruction the beampipe calorimeter has been exposed to electrons of 1 to $5\,GeV$ in the DESY testbeam 24, see section 7.4. The position reconstruction method has been tested by scanning the beampipe calorimeter with electrons of $E = 5\,GeV$ in x and y. The effect of the beampipe flange has been simulated by 5cm of iron in front of the BPC.

The position of a particle impinging on the BPC is known to an accuracy of $\sigma = 1.4\,mm$, given by the width of a 5 mm wide finger counter in front of the beampipe calorimeter.

To obtain the position reconstruction resolution, the reconstruction code (see section 8.3) for the ZEUS data has been applied to the testbeam data, using appropriate calibration constants as being determined from charge injection runs. The coordinate system used in the testbeam measurements has its origin at the center of the detector with the same orientation as in ZEUS.

8.1 Strip detector position reconstruction

The strip detector of the beampipe calorimeter is located in front of the first layer of tungsten absorber of the calorimeter. Since the calorimeter is situated behind a flange of 5 cm steel, corresponding to 2.8 X_0, particles entering the strip detector have already begun to shower. Therefore the strips are on average not hit by only a single particle which affects the position resolution.

Figure 8.1 shows the distribution of hits when only a single strip was hit in the testbeam exposure with 5 cm of iron in front of the BPC. The mean of the Gaussian fitted to the distribution is $\bar{x} = -6.1\,mm$ reproducing the beam position. The standard deviation of the Gaussian is $\sigma = 2.8\,mm$. The expected resolution from the width of the beam and the strip is 1.9 mm. The difference is due to the influence of the iron absorber.
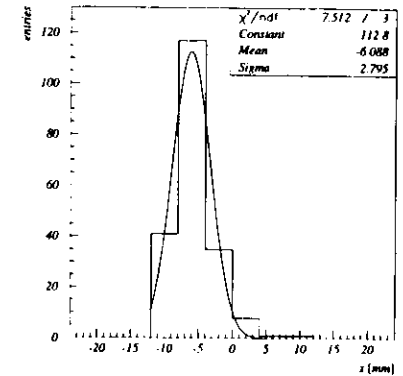
Figure 8.1: Reconstructed position for single hits

Due to showering of the incoming particle in the iron, on average more than one strip is hit. This can be used to improve the position resolution. The algorithm is described in the next sections.

8.2 Calibration of the strip detector

The strip detector is calibrated by a testpulser which injects some charge into the calibration capacitor of the preamplifiers of the strips. The pulseheight of the rectangular pulse can be varied by means of a reference voltage, see section 5.1.2.

For a pulseheight of $46.8\,mV (\dot{=}U_{ref} = 5.1\ V$, see equation (5.1)) the signal of a strip as seen by the ADC (after pedestal subtraction) is shown in figure 8.2. The mean strip signal versus injected charge is being plotted in figure 8.3 for the same strip. Care has been taken in selecting the pulseheight to assure that the readout chain is operating in a range where it responds linearly to signals. There is
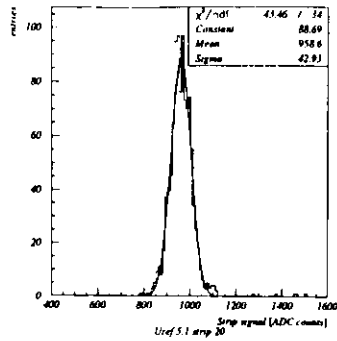
Figure 8.2: Strip signal for charge injection for 46.8 mV input
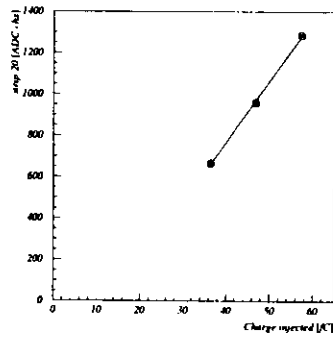
Figure 8.3: Strip detector charge calibration: ADC channels versus injected charge

an offset of about 14 fC, due to the sample & hold circuit in the readout electronics. The result of the fits of all strips is stored in a table, which gives for each strip the value of the offset and the slope in ADC channels/ fC (see Appendix B). The value of the charge quoted is however an 'effective' charge, because capacitance of the injection capacitor of 1 pC is comparable to 1 cm of conductor on a printed circuit board.

Electrons of 10 GeV deposit 3.9 MeV / cm energy by ionisation in silicon. At total depletion, the active thickness of the strips is 230 μm [9], giving an energy deposition of 90 keV. The threshold for electron-hole creation in silicon is 3.62 eV, giving 25000 electron-hole pairs. This corresponds to a charge deposit in the strips of 4 fC for a single electron.

8.3 The clustering algorithm

First, the ADC signals for all strips are converted into charges, according to

$$Q_i = \frac{ADC_i - \text{offset}_i}{\text{slope}_i},\qquad(8.1)$$

using the calibration from section 8.2.

The clustering then starts with looking for the strip with the maximum signal above a certain threshold, namely 16.9 fC. This corresponds to a threshold of about 4 Mips. Adjacent strips are added to the cluster as long as their signals are above threshold. If the adjacent strips are below threshold, one cluster is found. The strips of that cluster are removed from the list of strips, and the procedure starts over, by looking for another cluster on the remaining strips.

The position of a cluster is determined by the signal weighted average [3, 18] of the positions of the strips in a cluster. Since the strip width is smaller than the width of the shower, corrections to the position as obtained from the weighted mean have been neglected [16]. The clustering is done seperately in the x and y planes.

Before the clustering algorithm is started, the signal of any dead channel is substituted by linear interpolation. The readings of the two closest operational strips are taken and linearly interpolated. In the 1994 data taking this has been done for strips 7 and 10, both in the y plane.
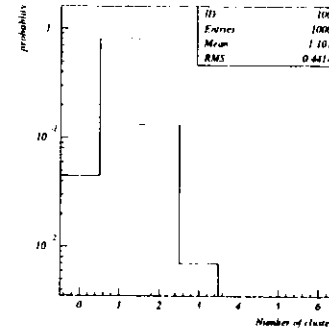
Figure 8.4: Probability for finding a certain number of clusters produced by single electrons of 5 GeV hitting the BPC
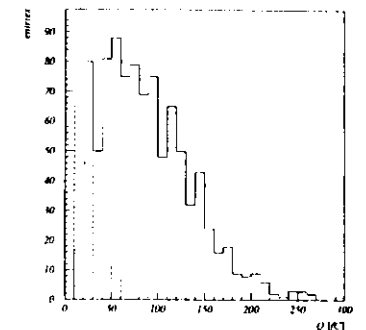
Figure 8.5: Energy deposited in the strips of a cluster for single electron hits of 5 GeV in equivalent charge. The solid line is the most energetic cluster, the dashed line is the second most energetic cluster.

The probability of finding a certain number of clusters in a testbeam exposure by 1000 electrons of 5 GeV at x = −6.1 mm is shown in figure 8.4. In 82% of all cases a single cluster is found, 13% of all events have two clusters, and 0.7% have three clusters. No cluster is found in 4.5% of the events.

The distribution of energy deposited in the strips belonging to a cluster is plotted in figure 8.5. The solid line is for the cluster with the highest signal, the dashed line is for the second most energetic cluster if there is more than one cluster. These secondary clusters have much less energy and stem from stray particles. The fact that only few strips (one or two) make up these secondary clusters support this as well as figure 8.6. That plot shows that the position of the cluster of second highest energy is different from the position where the beam particle hits the BPC. This leads to using only the most energetic cluster for determining the hit position.

The efficiency of finding an electron is calculated as a function of the maximum number of strips allowed in the cluster of the highest energy. The distribution of the number of strips belonging to the most energetic cluster in the testbeam exposure 1993 can be found in figure 8 7. The efficiency in the x plane averaged over 12 different beampositions (x ∈ [−7.1 mm; 1.9 mm], y ∈ [−1 mm, 4 mm]) can be found in table 8.1. The efficiency of the strips in the y plane should be the same since there is no material between the two planes. Unfortunately, this could not be verified experimentally since 5 of the 12 y strips were not operational in the testbeam exposure.

To get a reasonable acceptance and at the same time requiring a narrow cluster, only clusters of at most 4 strips are considered in the following paragraphs.

8.4 Position resolution

The mean as obtained from a Gaussian fitted to the reconstructed position versus the position of the beam can be found in figure 8 8 for a scan in x. The errors are the width of the Gaussian, therefore the uncertainty is for an individual hit. Since in the testbeam setup the 3 leftmost strips (in x) could not be read out not the full width of the strip detector could be scanned
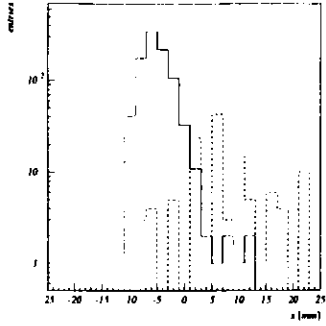
Figure 8.6: Cluster position for beam position $x = 6.1\,mm$. The solid line is the position of the cluster of highest energy, the dashed line for the cluster of second highest energy.
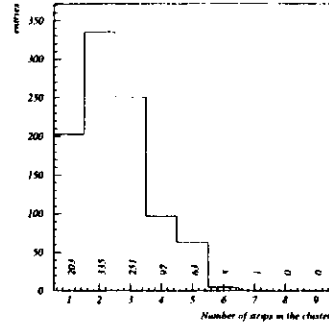
Figure 8.7: Multiplicity distribution of strips in the most energetic cluster used for position determination

max. multiplicity	efficiency [%]
8	96.7±0.2
7	96.7±0.2
6	96.3±0.2
5	95.3±0.3
4	88.3±0.7
3	78.1±1.1
2	54.0±1.0
1	21.0±0.4

Table 8.1: Position reconstruction efficiency in one plane for different strip multiplicities in the cluster as determined in the testbeam exposure

In figure 8.9 the standard deviation of a Gaussian fitted to the resonctructed position is plotted as a function of x. The error bars are the errors of the fit parameter. The position resolution is worse on the right hand side. This effect[16] is due to the third strip from the right which was not operational in the testbeam. Therefore the fit has been restricted to those positions where all strips were read out.

Subtracting the uncertainty in the beam position quadratically one obtains an overall position reconstruction resolution of:

$$\sigma = 1.9\,mm. \qquad (8.2)$$

Figure 8.8: Position scan (x) of the strip detectors in DESY testbeam 24
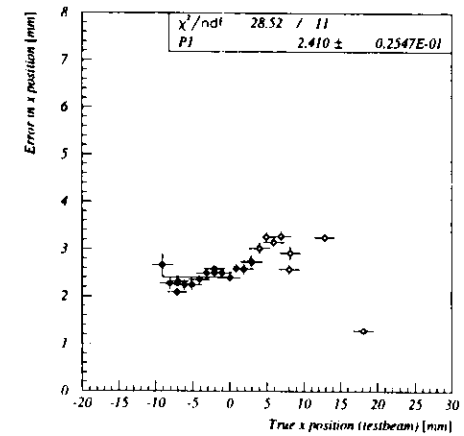
Figure 8.9: Position resolution of the strip detectors as a function of x in DESY testbeam 24

---

[16]It has been verified by artificially turning off another strip on the left hand side in the reconstruction code

9 Energy calibration

In 1994 it became necessary to replace the front-end electronics. Therefore the calibration from the testbeam, which had been done in 1993 using the testpulser could not be used anymore. The stability of the new front end electronics is described in section 11.4. In this chapter a method is described on how to calibrate the beampipe calorimeter with ZEUS data.

In principle there are two possibilities to reconstruct the total energy deposit in the beampipe calorimeter. Firstly, the signals of all the individual segments, see section 5.1.1, are digitized. Then their analytical energy sum is computed. The second method is using the analog sum signal, which has summed up the signals of all diodes already within the calorimeter housing and is used for triggering. In this analysis only the second method could be used since the cable driver of segment Ib for the line to the Rucksack did not work. The diodes themselves were working properly, giving the correct analog sum signal which is derived by the front-end electronics. This is demonstrated in figure 9.1:
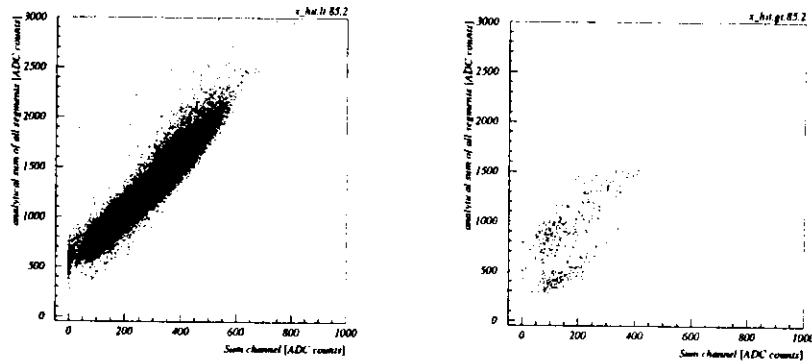
Figure 9.1: Signal of the sum of all diodes versus analog sum signal. Deviations from linearity are due to using uncalibrated ADC readings for this figure, and due to different gains on the readout amplifiers for the individual segments. Left figure for hit positions on the left half of the calorimeter, the right figure for the right half. The second band in the right plot is due to the readout line of segment Ib to the Rucksack being broken. The fact that the analog sum signal sees more energy for those hits, indicates that the readout of segment Ib itself was functioning and the signals indeed fed into the analog sum signal.

One can also see the effect of the beampipe shadow in this plot; the center of gravity is at smaller signals than in the left plot, where the particles did not have to pass the beampipe before entering the calorimeter.

To calibrate the BPC energy, use is made of the ZEUS main calorimeter energy measurement of real events. Using the reconstruction of y by the Jacquet-Blondel method, which is based on hadronic data alone, an independent measurement of the scattered electron energy can be carried out.

$$y_{JB} = \frac{\sum\limits_{hadrons} (E - p_z)}{2 E_e}, \tag{9.1}$$
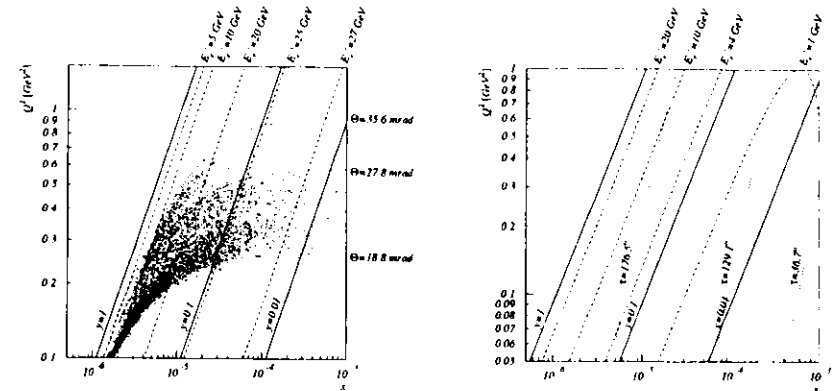
Figure 9.2: (x, Q^2) phase space accessible to the beampipe calorimeter. The solid lines denote constant y, the dashed lines are constant energy in the BPC, the dotted lines denote constant angle θ of the scattered electron (measured against the positron beam direction). Also shown is the raw data. For more details see text.

Figure 9.3: Acceptance of the ZEUS calorimeter in (x, Q^2) phase space for the hadronic system. The solid lines denote constant y, the dashed lines are constant energy of the struck quark, the dotted lines denote constant angle τ of the struck quark (measured against the proton beam direction).

where E_e is the beam energy of the positrons and the sum goes over all cells of the ZEUS main calorimeter above noise treshold. The p_z for a calorimeter cell i is taken as $(p_z)_i = E_i \cdot \cos\tau_i$, τ_i the angle from the interaction vertex to the center of the cell, as measured against the proton direction.

The other method reconstructs the y from the energy E_e' and the angle θ_e of the scattered positron with respect to the positron beam axis, as measured by the BPC.

$$y_e = 1 - \frac{E_e'}{2 E_e} (1 - \cos\theta_e) \tag{9.2}$$

From $y_e = y_{JB}$ one gets an independent value of E_e'.

The kinematical range that is accessible to the beampipe calorimeter is shown in figure 9.2 in the (x, Q^2) phase space. It is mainly limited by the minimum scattering angle of $18.8\,mrad$ and the maximum scattering angle of $35.5\,mrad$. Also shown is the scattering angle of $27.8\,mrad$ at which the positrons have to cross the beampipe before entering the BPC. The beampipe, made of $2\,mm$ of steel, represents $4\,X_0$ dead material at those scattering angles. Therefore a sizeable fraction of the energy of the positron is lost before it reaches the BPC, leading to an underestimate of Q^2. Events with a scattering angle greater than this have to be rejected. As discussed in section 12, some more cuts on the hit position are necessary and already applied in the energy calibration procedure. The distribution of the raw data sample in (x, Q^2) is shown without data selection cuts.

One can see that the lines of constant y are also lines of constant energy E_e' in the beampipe calorimeter. If one is able to select events of a certain y with the ZEUS detector, it is possible to calibrate the beampipe calorimeter.

If one turns to the acceptance of the uranium calorimeter in ZEUS in figure 9.3, one can see that there is an overlap in acceptance with the beampipe calorimeter. The boundary of the uranium
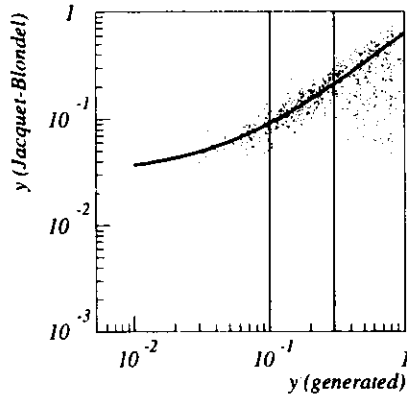
Figure 9.4: Reconstruction of y_{Bj} using the Jacquet-Blondel method. The solid curve is the result of a fit at $0.1 < y < 0.3$

calorimeter in the backward (electron) direction is given by the beampipe at $\theta = 176.5°$. The overlap with figure 9.2 extends to $y_{max} = 0.3$, corresponding to $E_{BPC} = 19.3\,GeV$.

It is also known [72], that there is a lower limit on the y that can be reconstructed by the Jacquet-Blondel method. This is due to noise in the uranium calorimeter and due to the fact that the position where a particle hits a calorimeter cell is not necessarily the center of the cell with the present analysis method. The lower limit is given by $y_{min} = 0.04$. In order to suppress events with radiative corrections, a minimum energy deposit of $1\,GeV$ in the RCAL is required, see section 12.12. This limits the minimum usable y in this calibration to $y_{min} = 0.1$ which corresponds to $E_{BPC} = 24.8\,GeV$.

9.1 Calibration

The y as reconstructed by the Jacquet-Blondel method plotted versus the true y_t for Monte-Carlo events can be found in figure 9.4. About 24000 events from diffractive (Pythia) and nondiffractive (Herwig) Monte Carlo codes (see section 13) were used. In between y_{min} and y_{max} a fit has been performed to determine the systematics in the event reconstruction:

$$y_{JB} = a + b \cdot y_t. \tag{9.3}$$

This leads to a correction function for the reconstruction of the true y_t:

$$y_t = -0.051 + 1.664 \cdot y_{JB}. \tag{9.4}$$
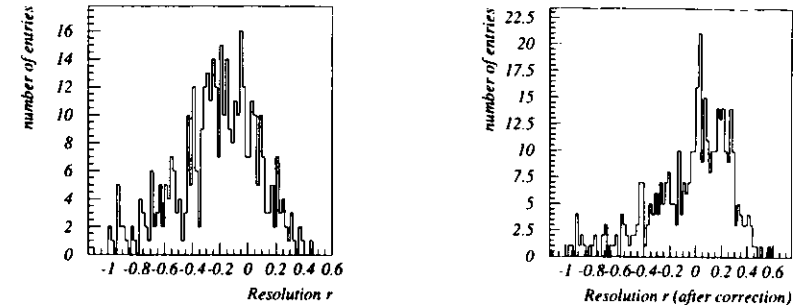
Figure 9.5: Relative error r (see equation (9.5)) for the Jacquet-Blondel reconstruction method. In the left figure the uncorrected y_{JB} is used, in the right figure the correction from equation (9.4) has been applied.

The improvement in the resolution of the Jacquet-Blondel method can be seen in figure 9.5. Plotted is the relative error r:

$$r = \frac{y_{JB} - y_t}{y_{JB}} \tag{9.5}$$

for the uncorrected and the corrected y_{JB}.

The idea of the calibration is to plot the raw data of the sum channel of the beampipe calorimeter for a range in reconstructed Bjorken y after applying the correction function (9.4). The y range is choosen such that it has a width corresponding to $1\,GeV$. The boundaries of the bins used for the calibration can be found in table 9.1.

Bjorken y	Energy in BPC [GeV]
0.2931	19.5
0.2568	20.5
0.2206	21.5
0.1843	22.5
0.1481	23.5
0.1118	24.5

Table 9.1: Boundaries of the y bins used in the calibration of the beampipe calorimeter

The fits to the pedestal subtracted raw data of the sum channel of the beampipe calorimeter after the data selection cuts of section 12 have been applied can be found in figure 9.6. The result of those fits versus the true electron energy is plotted in figure 9.7.
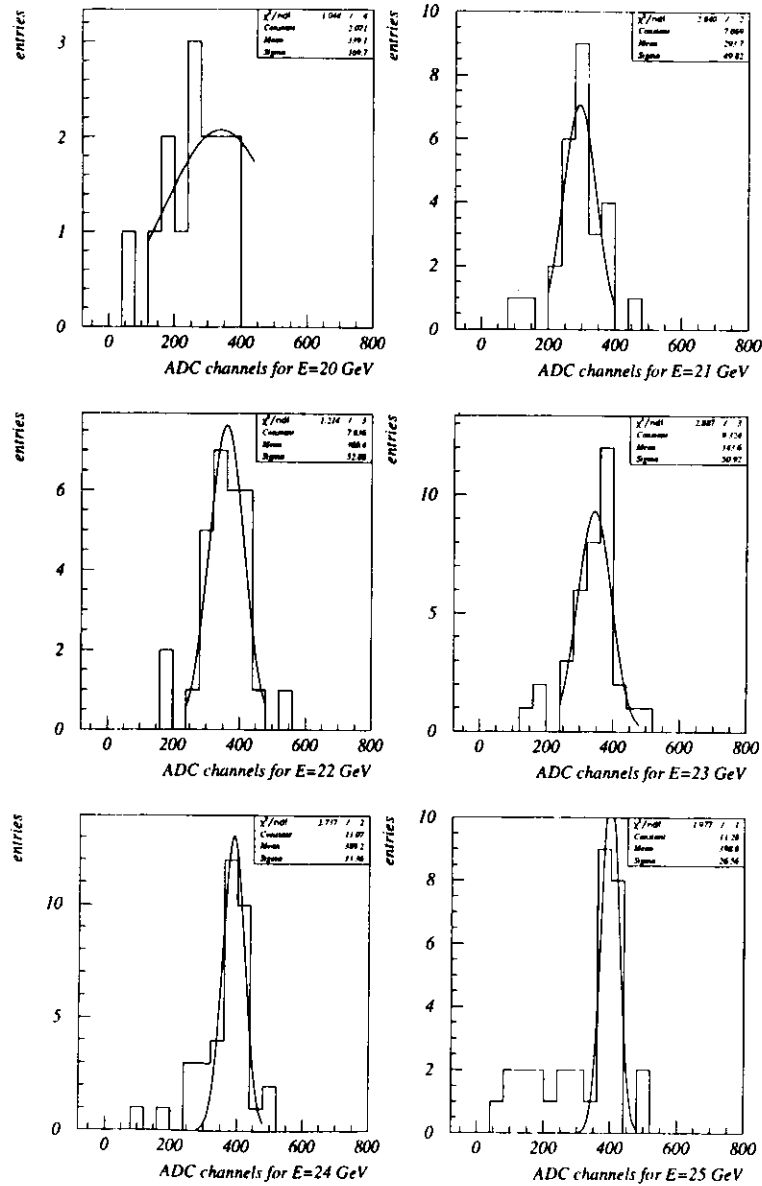
Figure 9.6: ADC spectra of the beampipe calorimeter for y_{Bj} bins according to table 9.1 on page 51.
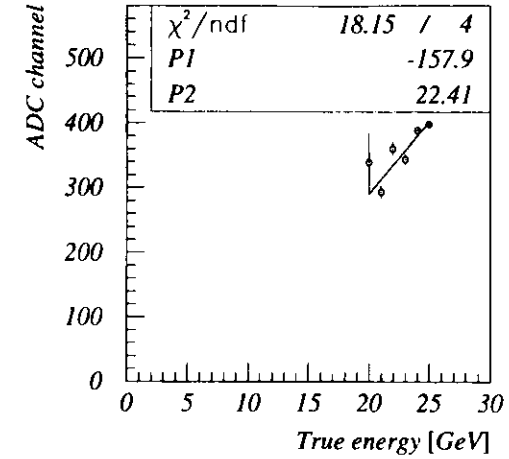
Figure 9.7: Energy calibration of the beampipe calorimeter using the y_{JB} method

Since this method suffers from limited statistics, another fit is done with less stringent selection cuts on the data. That fit result is

$$\text{ADC} = -157.7 + 22.0 \frac{channels}{GeV} \cdot E, \tag{9.6}$$

which agrees well with the fit in figure 9.7. The result of the calibration is:

$$E = 4.5 \cdot 10^{-2} \frac{GeV}{channel} \times \text{ADC} + 7.2 GeV, \tag{9.7}$$

where ADC is the pedestal subtracted readout of the sum-channel. The rather large constant term stems from the threshold of the diode within the peak detector in the readout chain

9.2   Cross check of the calibration

The calibration is crossed checked by two methods, one using $E - p_z$, the other the so called kinematic peak events.

The first method is using the distribution of $E - p_z$: by exploiting momentum and energy conservation it is readily obtained that for an incoming positron of energy E_e

$$2 \cdot E_e = E'_e(1 - \cos\theta_e) + \sum_{hadrons} E_i(1 - \cos\theta_i). \tag{9.8}$$
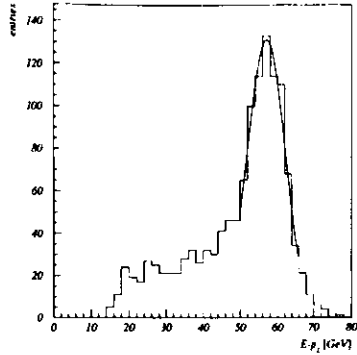
Figure 9.8: Global $E - p_z$ as determined by the beampipe calorimeter and the ZEUS main calorimeter being used as a calibration cross check. The result of the fit is given in equation (9.9).
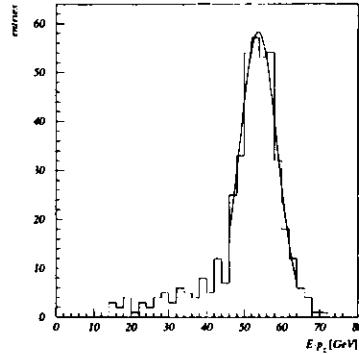
Figure 9.9: Global $E - p_z$ as determined by the beampipe calorimeter and the ZEUS main calorimeter in Monte Carlo. The result of the fit is given in equation (9.10).

Figure 9.10: Distribution of the energy for unbiased trigger, the kinematic peak is clearly visible (uncorrected for acceptance). The curve is a Gaussian fitted in the range $E = 27 \ldots 33\,GeV$.

E'_e is the energy of the positron scattered by an angle θ_e. On the assumption that the positron is hitting the BPC, the first term simplifies to twice the energy deposited in the beampipe calorimeter; the relative error due to neglecting the scattering angle is $3 \cdot 10^{-4}$. The sum over all hadrons is then the sum over all energy deposits in the ZEUS main calorimeter. The angle θ_i is the angle from the interaction point to the cell i in the calorimeter containing the energy E_i.

The distribution of $E - p_z$ of the event sample is shown in figure 9.8. The requirement imposed on these data is an energy deposit in the beampipe calorimeter and the main ZEUS calorimeter as is defined in the first level trigger slot 32, see section 11.6.1, and a selection by the third level trigger stage, see section 11.6.3. The data selection cuts to ensure proper timing, hit position etc. as described in section 12 are applied except the cuts on the azimuthal angle (section 12.6).

Most of the $E - p_z$ is contributed by the energy deposits in the beampipe calorimeter, such that the distribution is insensitive to the energy scale of the main calorimeter. The tail at lower values is due to the photon remnant escaping undetected through the beampipe.

Fitting a Gaussian to the region of $50\,GeV < E - p_z < 65\,GeV$ yields

$$
\begin{aligned}
\overline{E - p_z} &= 57.0 \pm 0.3 \quad GeV \\
\sigma_{E-p_z} &= 5.1 \pm 0.3 \quad GeV.
\end{aligned}
\tag{9.9}
$$

In figure 9.9 the $E - p_z$ distribution is shown in a Monte Carlo simulation, where the same cuts as in the data are applied. The result of the fit from $47\,GeV$ to $62\,GeV$ is:

$$
\begin{aligned}
\overline{E - p_z} &= 53.8 \pm 0.3 \quad GeV \\
\sigma_{E-p_z} &= 5.0 \pm 0.4 \quad GeV
\end{aligned}
\tag{9.10}
$$

Both distributions have their central value within 3.6% of the theoretical value of $55.0\,GeV$, for a HERA positron beam energy of $27.5\,GeV$. The widths of the distributions are not directly comparable
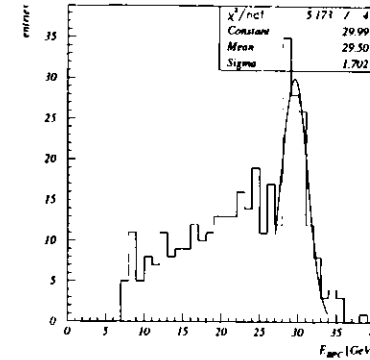
since the Monte Carlo sample is free of backgrounds and has the wrong energy resolution for the BPC (Mozart version 12). The difference to the theoretical value could be compensated for by shifting the energy spectrum of the BPC by $1\,GeV$ downwards. Instead of applying a correction like this, it will be used as the estimate of the systematic error of the calibration.

Another cross check is done employing the so called kinematic peak events. In figure 9.10 the distribution of the energy deposit in the BPC is plotted. To have a statistically independent sample, those events are taken from a datastream for which the filter algorithms at the second and third level stage of the ZEUS trigger system are bypassed, so called pass-through events. The prescale factor is rather high, but comparable to the one used in the datastream which has the SLT and TLT applied. The energy spectrum is not corrected for acceptance effects, but the peak due to the kinematics is clearly visible. The requirement for these events consists of an energy deposit in the beampipe calorimeter and the main ZEUS calorimeter as is defined in the first level trigger slot 32, see section 11.6.1. The data selection cuts to ensure proper timing, hit position etc. as described in section 12 are applied except the cuts on the angle (section 12.6). In order to determine the endpoint of the spectrum, a Gaussian is fitted to the data between $27\,GeV$ and $33\,GeV$, since the endpoint of the spectrum is smeared by the energy resolution of the calorimeter. The result of the fit is

$$
\begin{aligned}
\overline{E} &= 29.2 \pm 0.2 \quad GeV \\
\sigma_E &= 1.7 \pm 0.2 \quad GeV.
\end{aligned}
\tag{9.11}
$$

The mean value is expected to be the beam energy of the positrons. Therefore the calorimeter is overcalibrated by 7.3%. The width of the Gaussian is given by the energy resolution of the BPC. The σ_E of equation (9.11) translates into a relative resolution of $\sigma_E/E = 5.8\%$ at $E = 27.5\,GeV$. This is in good agreement with the result in equation (7.11) from the testbeam measurement.

The deviations from the theoretically expected values of the distribution of $E - p_z$ (equation (9.9)) and the kinematical peak (equation (9.11)) are used as an estimate of the systematic error. The two deviations are averaged and yield an error of 5.5% of the calibration

9.3 Calibration stability

Figure 9.11 shows the deposited energy in the BPC versus run number N_{run} for events that pass the selection cuts of section 12. Up to run 9560 problems with oscillations of detector signals persisted. A linear function

$$\langle E \rangle = P_1 + P_2 \cdot \frac{N_{run} - 9870}{9870} \tag{9.12}$$

has been fitted to the mean energy of the events in about 10 runs each for the runs 9560 through 10154. The result of the fit $P_1 = 19.1 \pm 0.1\, GeV$ and $P_2 = -7.5 \pm 7.5\, GeV$ shows that there is no significant drift of the energy calibration over this run range. Therefore run to run corrections are not necessary. Nonetheless, the fit allows to give an estimate of the calibration stability.

The error on the slope P_2 is as big as the slope itself. Therefore the fit is compatible with no change of the calibration over time, which is assumed for the analysis. The slope is used as an estimate of the systematic uncertainty of the calibration. The value of P_2 translates into a calibration uncertainty of 2.5% over the whole data taking period.
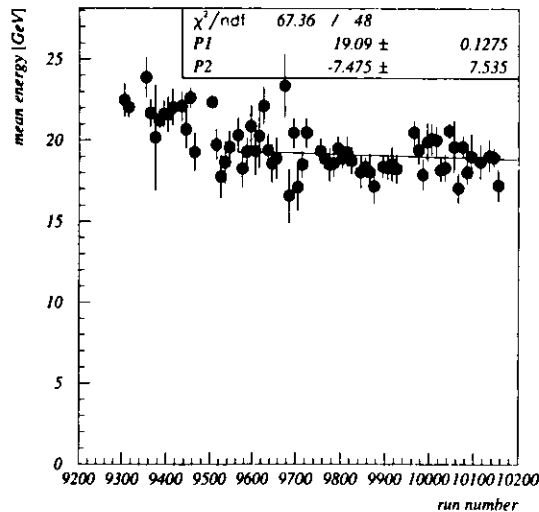
Figure 9.11: Mean energy of events with the data selection cuts (see section 12) used in the total cross section analysis versus run number

10 Monte Carlo simulation

The beampipe calorimeter hardware is incorporated into the ZEUS detector simulation program Mozart. Mozart uses for the particle tracking and the materials simulation the Geant program, developed at CERN [15].

The calorimeter geometry is modeled in very detail. The silicon diodes are thin, $400\,\mu m$, too thin to be simulated correctly. Therefore the thickness in the Monte Carlo is $2\,mm$, requiring the signal in the simulation to be divided by five. The strip detectors are simplified. They consist in the detector simulation of two $400\,\mu m$ thin silicon planes, with no transverse division. Since Geant doesn't simulate silicon that thin well, the hit position is calculated by the *arithmetical* mean of the positions where particles traverse the silicon planes.

For this analysis Mozart version 12 which describes the 1993 configuration had to be used[17], which had the beampipe calorimeter modelled in a different configuration. The difference is, that in Mozart version 12 the position of the BPC and the adjacent beampipe walls is $10\,mm$ closer to the beams than in reality, and a gap between the diodes in y of $4\,mm$ existed. In the 1994 configuration of the BPC this gap did not exist.

10.1 Calorimeter response

The MC description of the beampipe calorimeter has evolved with time. In Mozart version 12, shower terminators were used, to speed up the production of Monte Carlo events. They work by terminating the shower cascade if the particle energy is below a certain threshold. The tracking of the particle is stopped and its remaining energy is locally deposited. The shower terminators have been tuned to work with the uranium-scintillator calorimeter of ZEUS. Since the beampipe calorimeter is a tungsten silicon calorimeter, they degrade its performance. In figure 10.1 the result of $27.5\,GeV$ electrons hitting the BPC at x=-10 mm and y=+10 mm next to the center can be seen. Too little energy is seen by the beampipe calorimeter and the energy resolution is worse than has been measured in the testbeam. At $27.5\,GeV$ the relative resolution is $\sigma_E^{num12}/E = 7.4\%$, which corresponds to

$$\frac{\sigma_E^{num12}}{E} = 39.0 \frac{\%}{\sqrt{E(GeV)}} \tag{10.1}$$

In figure 10.2 the hit position as reconstructed in Mozart by the aforementioned averaging procedure can be found. The position is reconstructed correctly, but the resolution of $0.1\,mm$ is much too good.

For comparison, the result of the same tests with the Mozart version 13 can be found in figures 10.3 and 10.4. The energy of the electrons is $27.5\,GeV$, hitting at x=-15 mm and y=+10 mm. In this version the shower terminators are turned off for the beampipe calorimeter and the beampipe in its vicinity (i.e. the beampipe around collimator C5 and within RCAL). The energy response is correct, and the energy resolution of

$$\frac{\sigma_E^{num13}}{E} = 28.6 \frac{\%}{\sqrt{E(GeV)}} \tag{10.2}$$

agrees with the testbeam measurement, equation (7.11) on page 40. The procedure to reconstruct the hit position in version 13 is the same as in version 12; the resolution has been tuned to agree with testbeam measurements, see equation (8.2) in section 8.4. The tuning is done by smearing the calculated position with a random smearing following a gaussian of width $2.0\,mm$.

---

[17]The Mozart version 13 describes the 1994 configuration correctly, but became released too late to be used for all simulations of this analysis.
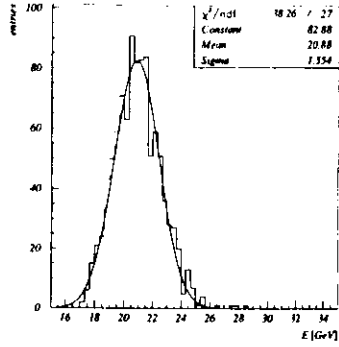
Figure 10.1: Energy response of the beampipe calorimeter to electrons of $27.5\,GeV$ in Mozart version 12
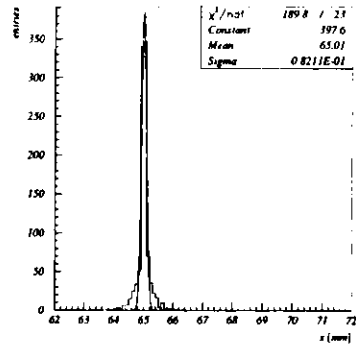
Figure 10.2: Reconstructed hit position in x for $27.5\,GeV$ electrons in Mozart version 12

To get the energy response versus hit position, the beampipe calorimeter is scanned in Monte Carlo with electrons of 15 GeV. The electrons traverse the beampipe flange before they hit the calorimeter. The energy deposit can be seen in figure 10.6. The curve drawn is the result of a shower model fit to the data in figure 10.5.

The transverse profile of an electromagnetic shower can modeled by use of two exponentials [12, 3]:

$$\frac{dE_{dep}}{dr} = C_1 \cdot e^{-\lambda_1 \cdot r} + C_2 \cdot e^{-\lambda_2 \cdot r}. \tag{10.3}$$

This formula describes the radial distribution of the energy deposit in the calorimeter. Since the diodes in the calorimeter have rectangular boundaries, equation (10.3) is an approximation, which however has been used to save computing time.

The response function $\mathcal{R}$ is split into a horizontal and vertical response function.

$$\mathcal{R}_{hor}(x) = \int_{x_1}^{x_2} dx \frac{dE_{dep}}{dx}(|x - x_0|) + \int_{x_3}^{x_4} dx \frac{dE_{dep}}{dx}(|x - x_0|) \tag{10.4}$$

x_1 and x_2 are the boundaries of the left diodes, x_3 and x_4 the boundaries of the right diodes, x_0 being the center of the calorimeter. The vertical response function $\mathcal{R}_{vert}(y)$ is defined in the same way with the integration boundaries the active area of the diodes in y.

Due to the gap between the diodes on the same ceramic card (see 4.1) the response function shows a dip of 50% at the center ($x_0 = 7.74\,cm$ in Mozart version 12) of the calorimeter. As a consistency check, the horizontal response function has been fitted to only the central calorimeter region, as shown in figure 10.5. By inspection of figure 10.6, one sees the resulting response function describes the overall response of the beampipe calorimeter very well. The discrepancy at $10\,cm < x < 11\,cm$ is due to a problem in Mozart. This problem doesn't affect the analysis of the data, since only events which do not hit the beampipe before they enter the beampipe calorimeter are used in the analysis.
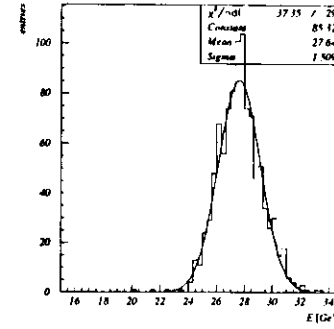
Figure 10.3: Energy response of the beampipe calorimeter to electrons of $27.5\,GeV$ in Mozart version 13
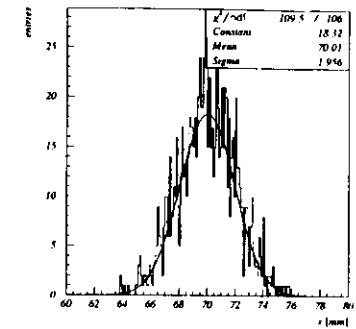
Figure 10.4: Reconstructed hit position in x for $27.5\,GeV$ electrons in Mozart version 13
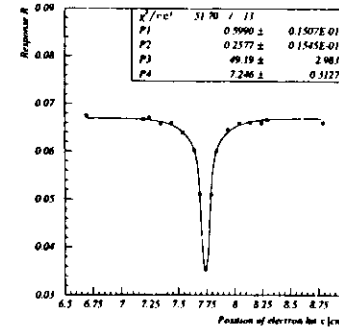
Figure 10.5: Fit of the response function $\mathcal{R}$ to the central region of the beampipe calorimeter in Monte Carlo ($15\,GeV$ electrons)
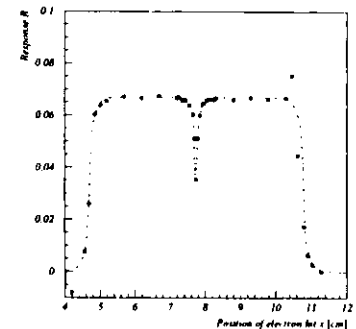
Figure 10.6: Response of the calorimeter to $15\,GeV$ electrons in Monte Carlo (the curve drawn is the function $\mathcal{R}$ from figure 10.5)
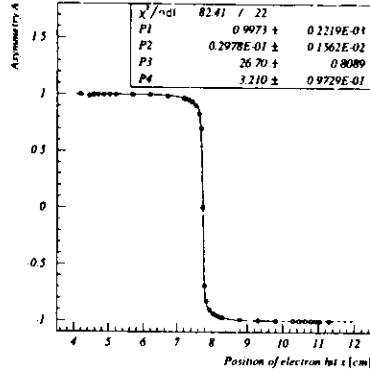
Figure 10.7: Fit of the asymmetry function A for $15\,GeV$ electrons in Monte Carlo. Only solid points participate in the fit.

10.2 Calorimeter asymmetry

One can define a horizonatal asymmetry function $\mathcal{A}$:

$$\mathcal{A}_{hor}(x) = \frac{E_{left} - E_{right}}{E_{left} + E_{right}} \qquad (10.5)$$

and similarly a vertical asymmetry function

$$\mathcal{A}_{vert}(y) = \frac{E_{bottom} - E_{top}}{E_{bottom} + E_{top}} \qquad (10.6)$$

where

$$E = \int dx \frac{dE_{dep}}{dx}, \qquad (10.7)$$

the boundaries choosen as the rims of the left or right, upper or lower diodes. The horizontal asymmetry function is shown in figure 10.7.

10.3 Clustering Monte Carlo

Because of the finite width of the clusters in the position reconstruction algorithm (see section 8.3), there is a migration of events from outside the active area into the edges of the strip detector. The center of the shower developing in the flange in front of the BPC, i.e. the true hit position, may be outside the strip detector, but some strips may still be hit due to the lateral spread of the shower.

The effect is a migration of events into the active area of the BPC. To simulate this and the effect of the two dead strips in the y plane, a special Monte Carlo program is used.

As a first step, the true particle position is calculated assuming a dependence of the positron scattering angle Θ of the form

$$f(\Theta) = \left(\frac{\Theta}{P_1}\right)^{P_2}, \qquad (10.8)$$

with P_1, P_2 parameters, and an isotropic distribution in Φ, the azimuth angle around the beam direction. The slope parameter P_2 has been determined from Pythia and Herwig event generators, see section 13. The slope in Pythia is $P_2 = -1.8$, the slope from Herwig is $P_2 = -1.4$. Taking the weights of the different processes into account a value of $P_2 = -1.6$ is used. The deviation from $P_2 = -1$ expected from QED is due to the Q^2 dependence of the γ^*p cross section, which is parametrized differently in the two generators.

For each position a hit is generated using the strip multiplicity as determined from the most energetic cluster in the data. The probability for a given strip multiplicity and the mean energy associated with such a cluster can be found in table 10.1.

# strips	probability	equivalent energy [fC]
1	0.2161	33.3
2	0.2810	79.5
3	0.2444	119.2
4	0.1440	156.0
5	0.0606	192.4
6	0.0274	236.3
7	0.0134	276.8
8	0.0078	302.8
9	0.0021	398.8
10	0.0008	438.1
11	0.0003	427.3
12	0.0021	703.3

Table 10.1: Probability for finding n strips in the most energetic cluster in data and the associated energy (for x strips).

The energy is distributed into 4 mm bins using a binominal distribution. This is consecutively filled into the strips of the position detector with the energy of each bin filled into the hit strips, proportional to the overlap of 4 mm bin and strip width. Then the clustering algorithm as described in section 8.3 is applied to the generated data. To be comparable to data, the same cut on the strip multiplicity in a cluster is applied as in data.

The result of this simulation is shown in figure 10.8 for x and 10.9 for y. The two dips at $y = -5\,mm$ and $y = -17\,mm$ are the effect of dead strips 7 and 10. The agreement with data, figure 12.7, is good.

In order to reduce the corrections due to this migration effect, the most outside bins are not be used in the analysis. In x a fiducial cut of 8 mm, in y of 4 mm is applied. It has also been checked that the effect is the same for the different slopes of the Θ distribution of the Pythia and Herwig event generators.

The acceptances in the different (x, y) bins can be found in table E.1 in appendix E.
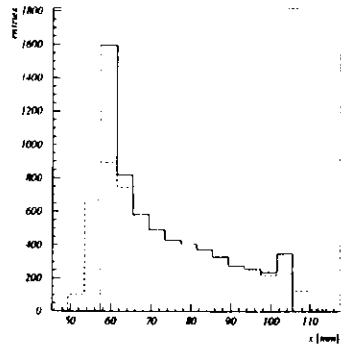
Figure 10.8: Result of the clustering simulation in x. The solid line respresents the reconstructed hit position in x. The dashed line is the distribution of the true x position.
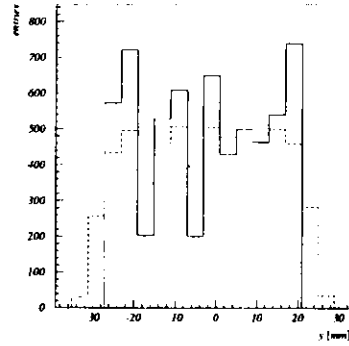
Figure 10.9: Result of the clustering simulation in y. The solid line respresents the reconstructed hit position in y. The dashed line is the distribution of the true y position.

10.4 Vertex distribution

The event vertex distributions in the Monte Carlo calculation are plotted in figure 10.10. The corresponding plot for data can be found in figure 11.1. The difference is that in the simulation the vertex is in x and y centered around zero, while there is an offset of 1.5 mm and -1.3 mm in x respectively y in data. The offsets for z also differ by 6 mm (see the discussion in section 11.3).
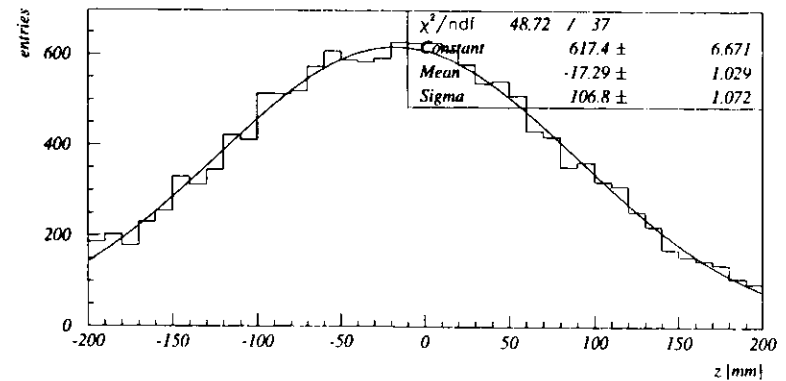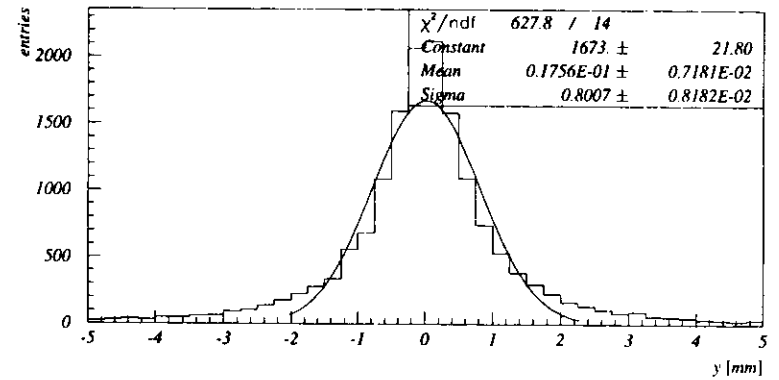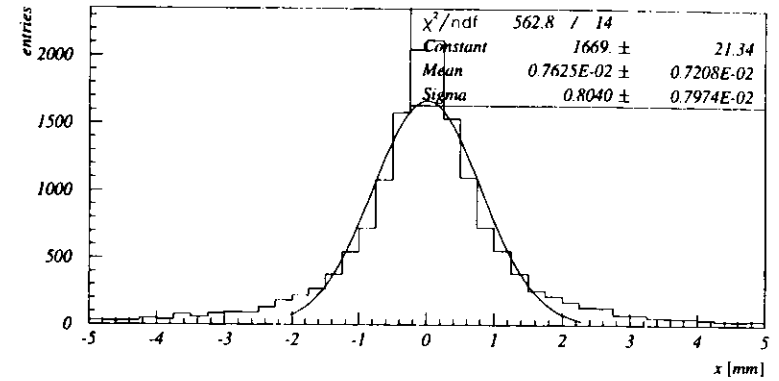
Figure 10.10: Distribution of vertex positions in Monte Carlo in detector coordinates

11   1994 Data taking with the beampipe calorimeter

The beampipe calorimeter was reinstalled into the ZEUS detector after replacement of the front-end electronics became necessary, see section 11.10. This has been done during an access on July, 18th 1994. After timing it in, data taking with the BPC resumed at run 9287.

11.1   HERA running conditions

In 1994, HERA operated with 153 colliding bunches of positrons of $27.5\,GeV$ and protons with an energy of $820\,GeV$. The average current of all positron bunches was $17\,mA$, for protons $38\,mA$. Additional unpaired positron and proton bunches were used to determine beam related background. The root mean square of the proton bunch length is approximately $24\,cm$. The positron bunch width is neglible in comparison. The average luminosity was $\sim 1.3 \cdot 10^{30}\,cm^{-2}\,s^{-1}$. Approximately 7% of the proton current is contained in satellite bunches, which are shifted with respect to the nominal bunch by $4.8\,ns$ corresponding to the RF of $208\,MHz$, resulting in a fraction of the events occuring at $z = +72\,cm$.

11.2   Run range used in this analysis

The first run to be used after the reinstallation of the beampipe calorimeter is 9560 on August, 27th 1994, as discussed in section 9.3 about the calibration stability. After run 10154 (October, 24th 1994) the interaction point has been shifted by 65 cm towards the forward calorimeter. This determines the last run used in this analysis.

11.3   Beam tilt and vertex offset

The nominal proton beam orbit in ZEUS is tilted with respect to the z-coordinate of the ZEUS reference frame. The tilt has been determined by the DESY survey group as

$$\Theta_p = 0.41\,mrad$$

in the horizontal plane. The ZEUS luminosity monitor has determined [65] that the positron beam was also tilted by

$$\Theta_e = -0.15\,mrad$$

with respect to the nominal proton orbit. This adds up to a total tilt of the positron beam of

$$\Theta_{tilt} = 0.26\,mrad \tag{11.1}$$

with respect to the ZEUS coordinate system in the horizontal plane.

The average vertex position in 1994 did not coincide with the ZEUS center. The displacements are determined by a Gaussian fit to the vertex distributions. The vertex position is determined by the ZEUS tracking reconstruction program VCTRAK [45]. The coordinate system used in there has an offset [44] with respect to the ZEUS coordinate system in z of

$$\Delta_z = z_0^{ZEUS} - z_0^{VCTRAK} = -25\,mm. \tag{11.2}$$

The vertex distributions in ZEUS coordinates with the fitted Gaussians are shown in figure 11.1. The average vertex position from the fits for this analysis is:

$$
\begin{aligned}
x &= 1.5\,mm \\
y &= -1.3\,mm \\
z &= -6.0\,mm.
\end{aligned}
\tag{11.3}
$$

χ²/ndf	46.16 / 18	
Constant	187.7 ±	5.504
Mean	1.527 ±	0.2919E-01
Sigma	1.245 ±	0.3102E-01

χ²/ndf	74.13 / 14	
Constant	208.6 ±	6.698
Mean	-1.297 ±	0.2719E-01
Sigma	1.056 ±	0.3265E-01

χ²/ndf	27.76 / 37	
Constant	102.5 ±	2.707
Mean	19.02 ±	2.402
Sigma	102.6 ±	2.349
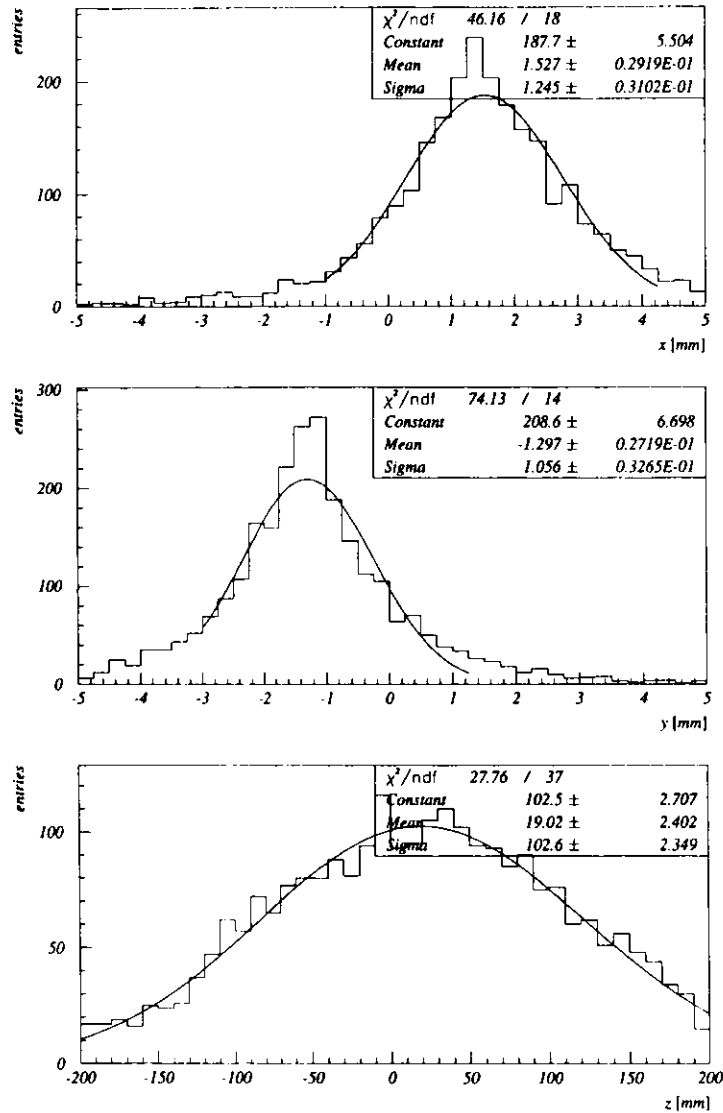
Figure 11.1: Distribution of vertex positions in ZEUS detector coordinates for events used in this analysis
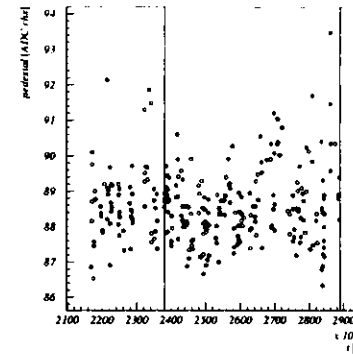
Figure 11.2: Pedestal distribution of the strip no. 5 versus time in seconds elapsed since the beginning of the year 1994. The lines indicate runs 9560 and 10154.
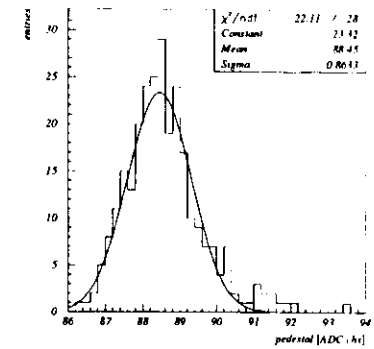
Figure 11.3: Distribution of the pedestal of strip no. 5

11.4 Electronics stability and linearity

The stability of the BPC electronics can be checked by looking at the pedestals, which are determined at the beginning of each run by averaging 2000 random samples. In figure 11.2 the pedestal of strip no. 5 is plotted versus time. It is very stable over the complete running period, and no sytematic dependence on time is visible. Figure 11.3 shows the distribution of the pedestals. It follows a Gaussian with $\sigma = 0.86$ channels.

The same analysis is done for the pedestal of the analog sum channel. The pedestal distribution versus time, figure 11.4 shows a sharp drop on October 5th, 1994, when there had been a maintenance access to the detector. The pedestal distribution is plotted in figure 11.5. The root-mean-square of the distribution is 0.8257 channels. Fitting a Gaussian to the runs before the aforementioned access yields $\sigma = 0.27$ channels, after that it is $\sigma = 0.31$ channels.

Nonwithstanding the very stable readout chain of the BPC, the pedestal subtraction is done in this analysis (offline) for each run seperately.

To test the linearity of the front-end as well as the readout electronics, special runs have been taken. For those, the testpulser put a precisely known voltage over the calibration capacitors on the preamplifier boards in the BPC. In this and the following paragraph, all plots are from data of the analog sum channel.

The linearity of the readout system can be found in figure 11.6. There the pedestal subtracted ADC readout is plotted versus the voltage U_T applied to the capacitors. This voltage is generated by the testpulser within the BPC , see section 5.1.2. The linear fit covers $U = 0.7 \ldots 1.5\,V$. Using calibration equation (9.7) this corresponds to energies of $13\text{-}30\,GeV$. It has been verified that the readout system is linear at least up to twice the signal caused by positrons of HERA beam energy. The onset of the nonlinearity is due to the differential amplifier in the cable receiver. The offset at small signals is due to threshold effects in the peak-detector.

For checking the linearity of the front-end electronics for small signals, an additional amplifier has been
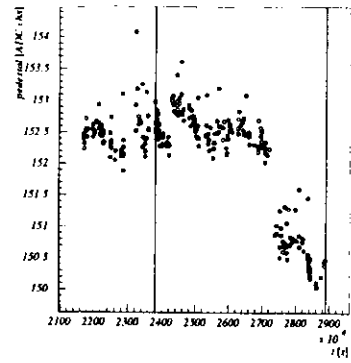
Figure 11.4: Pedestal distribution of the analog sum channel versus time, time in seconds since the beginning of the year 1994. The lines indicate runs 9560 and 10154. The sharp drop visible occured during a maintenance access to the detector on October 5th.
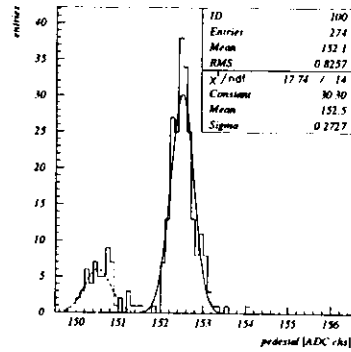
Figure 11.5: Distribution of the pedestal for the analog sum channel. The RMS value refers to the complete distribution. The σ of the Gaussian quoted belongs to the solid line fit to the data before October 5th; the dashed line fit to the data after that date is $\sigma = 0.31$ channels

Date	P_1	P_2
22.7.1994	-199.6	469.7
16.8.1994	-192.5	456.2
30.8.1994	-197.4	456.9

Table 11.1: Fit results of the charge injection runs

inserted between cable receiver and peak-detector. By doing so, the signal is always below the onset of the nonlinearities in the cable receiver and can after the amplification be used to check the rest of the readout chain over the full dynamic range. In plot 11.7 a linear function has been fitted to such data. It proves that the chain *following* the cable receiver, consisting of peakdetector, sample&hold and ADC, is linear over the full range of signals up to the ADC conversion endpoint at 4096 channels.

Table 11.1 gives the dates of charge injection runs during 1994 data taking after replacement of the front end electronics. At about 20 different settings of the voltage U_T, 1000 events have been taken each. The rate has been set to $15\,Hz$, when no beams were present in HERA. The mean of the signal read out is determined by fitting a Gaussian to the data of the different settings for U_T. The results of fits to those mean values of the form $ADC = P_1 + P_2 \cdot U$ are also shown.

The charge injection runs show a stable performance of the readout system. However, since the charge injection does not check the perfomance of the diodes, which were subject to considerable radiation (see section 11.10), a different approach is used to check the long term stability of the whole system of diodes and readout system, see section 9.3; the result is that it was stable to within 2.5%.
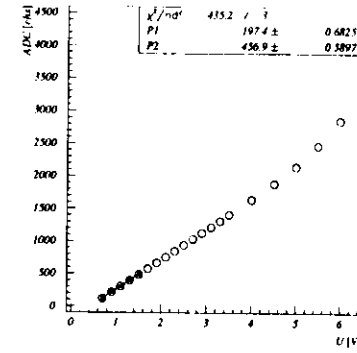
Figure 11.6: Mean ADC signal versus different testpulser voltages
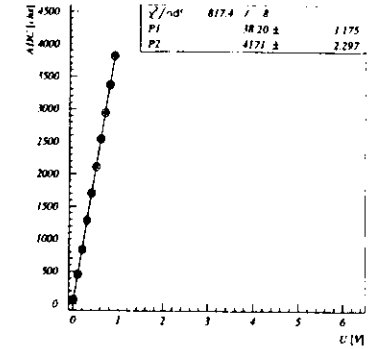
Figure 11.7: Small signal behaviour of the readout system (Additional amplifier, see section 11.4)

11.5 Electronics noise

The noise of the readout system has been determined by using the charge injection runs. The noise σ_Q of the readout system is determined by fitting a Gaussian to the 1000 events taken for a fixed charge being injected. The relative noise $\sigma_Q/\bar{Q}$ plotted versus U_T is shown in figure 11.8. Fitting a function of the form

$$f(U) = a \cdot (U_T)^b, \tag{11.4}$$

where a and b are free parameters, gives

$$\left(\frac{\sigma_Q}{\bar{Q}}\right)_{Noise} = 4.1\% \cdot (U_T)^{-1.41} \qquad U_T \text{ measured in } V. \tag{11.5}$$

Using the testpulser calibration and the energy calibration from equation (9.7) this translates into

$$\left(\frac{\sigma_Q}{\bar{Q}}\right)_{Noise} = \frac{2.91}{(E + 1.7\,GeV)^{1.41}}, \tag{11.6}$$

where E is in GeV. For energies greater than $10\,GeV$ the noise of the readout system is less than that given by the sampling fluctuations in the calorimeter. The curve of the readout noise in comparison with the noise due to sampling fluctuations is drawn in figure 11.9.
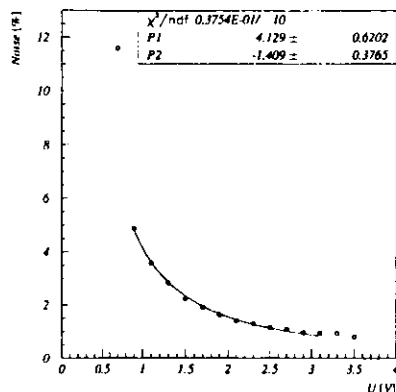
Figure 11.8: Relative noise σ_Q/Q of the readout system
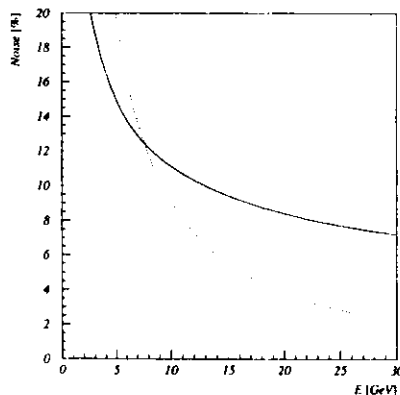
Figure 11.9: Contributions to energy resolution σ_E plotted versus the beam energy E. The solid line is the contribution from sampling fluctuations within the calorimeter, the dashed line represents the noise of the readout electronics.

11.6 Beampipe calorimeter trigger in 1994

The beampipe calorimeter participates as an independent component in the ZEUS trigger system [76]. As described in section 5.2.2, the BPC provides data already at the first trigger stage. These data are composed of timing information with a resolution of 5 ns (resolution of the TDC) and information whether the signal of the calorimeter surpassed a certain threshold. Both informations are derived from the inverted calorimeter analog sum signal fed into a constant fraction discriminator. The timing resolution of the calorimeter is 1.8 ns, the timing resolution of the discriminator is much better; the limiting factor is the TDC on the interface to the global first level trigger. The threshold of the discriminator has been set to a nominal value of $7\,GeV$ (uncalibrated). As one can deduce from figure 11.16 after calibration the data starts at energies of $9\,GeV$. The entries at zero energy are due to triggers when the ADC readout could not convert data, as discussed in section 11.8 about deadtime.

The ZEUS Global First Level Trigger (GFLT) has three trigger 'slots' reserved for BPC data. At the second and third level trigger stage BPC data is taken by data streams of the soft and hard photoproduction and the deep inelastic study groups.

The following sections describe the triggers that were used for data acquisition in this analysis.

11.6.1 FLT

The three slots with beampipe calorimeter triggers at the first level trigger stage are two slots for data taking and one for monitoring purposes. The monitoring slot 31 triggers in case the energy threshold in the beampipe calorimeter is surpassed and the timing provided by the BPC is in accordance with a positron-proton collision ($t_{BPC} > -15\,ns$). As can be found in table C.1 in appendix C, some vetoes are applied as well. Timing cuts and vetoes reduce the rate from $500\,Hz$ as raw rate at the discriminator in the BPC readout to $84\,Hz$ for a luminosity of $L = 1.3 \cdot 10^{30}\,cm^{-2}\,s^{-1}$ (run 9650).

In figure 11.10 the distribution of the time of a hit in the BPC is plotted for the monitoring trigger. The events with a time corresponding to proton beam related background events are already cut out effectively by the timing information provided by the BPC to the global first level trigger stage. They would occur at $-20\,ns$.

In figure 11.12 the average trigger rate of the monitoring slot 31 in a given run is plotted versus the average luminosity for that run. To not overload the second stage trigger, this GFLT slot is prescaled by a factor of 512. Clearly the rate increases with luminosity. Since the underlying physics rate is on the order of $0.1\,Hz$ (elastic scattering, see [53]) for 1994 luminosities ($L \approx 10^{30}\,cm^{-2}\,s^{-1}$) the rate is almost entirely due to background events.

In an attempt to further illuminate this situation, the rate of slot 31 is also plotted versus the squared current of the positron beam in figure 11.13. The rate shows a more linear dependence on the squared current than on the current itself. This is expected since the rate due to interactions of the positron beam with the residual gas in the beampipe grows linearly with the current. Nevertheless, if the current increases, more gas molecules become desorbed from the beampipe walls due to synchrotron radiation. This increase in gas pressure has to be folded into the background rate.

Figure 11.11 shows the energy spectrum of the monitoring trigger for the runs 9560-9624, which shows a steep decrease starting from low energies. The events at energy zero are from triggers while the BPC readout system was busy recording the previous trigger. It is interesting to note that the monitoring events center in a small area close to the beampipe, at values of y in agreement with the average vertex position as stated in equation (11.3) on page 65. This is shown in figure 11.14 which is a contour plot of the hit position of the most energetic cluster with the cluster quality cuts of section 12.2 already applied, taken by the monitoring trigger. The empty regions at $y = -5.1\,mm$ and $y = -17.1\,mm$ are due to dead strips.

Figure 11.10: Timing distribution of BPC events in the GFLT monitoring trigger 31
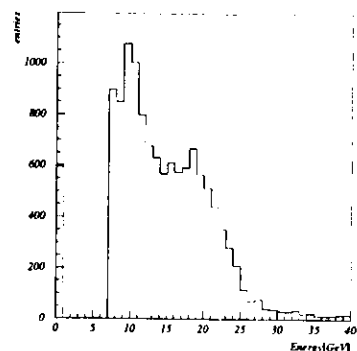
Figure 11.11: Calibrated energy spectrum of the beampipe calorimeter for the first level monitoring trigger 31

An excerpt of the trigger setup at the Global first level trigger from the GFLT homepage [62] in the Worldwide Web can be found in appendix C. The data taking triggers at the GFLT are slots 32 and 34. The exact definitions can be found in tables C.1 and C.2. Slot 32 requires a BPC hit with timing compatible with e-p collisions ($t_{BPC} > -15\,ns$) and a hit in the ZEUS uranium calorimeter. The requirement on the uranium calorimeter is:

more than $464\,MeV$ in the RCAL EMC section (excluding 8 towers around the beampipe)

or more than $1.25\,GeV$ in the RCAL EMC section including the beampipe towers (this trigger's resolution is coarser than the above)

or more than $1.25\,GeV$ in the FCAL EMC section including the beampipe towers

or

more than $1.25\,GeV$ anywhere in the uranium calorimeter in coincidence with a track in the central drift chamber

In addition, the event must not be vetoed by either the C5 counter, the vetowall nor the SRTD. The differences among the different configurations in table C.1 stem from different quality criteria on tracks and vetowall veto. The rate of trigger slot 32 plotted versus the average luminosity in a given run can be seen in figure 11.17.

The time distribution of the triggers in slot 32 can be found in figure 11.15. The time offset is adjusted in such a way that positron-proton collisions occur at $t = 0\,ns$. Proton background hits the beampipe calorimeter $20\,ns$ earlier.

The energy spectrum of particles hitting the BPC for this slot can be found in figure 11.16. The energy spectrum shows events at the kinematical peak which is at the positron beam energy E_e modified by radiative corrections and subtracted by the photon energy that is necessary to trigger the ZEUS main
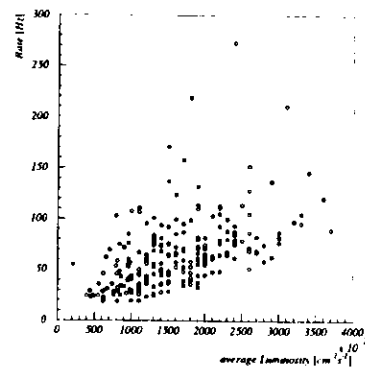
Figure 11.12: Rate of monitoring trigger versus average luminosity
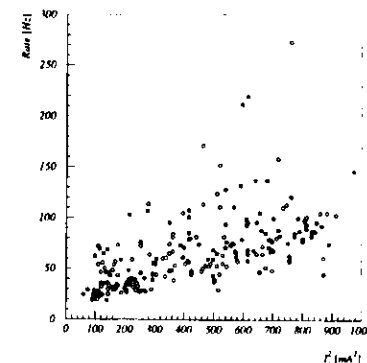
Figure 11.13: Rate of monitoring trigger versus positron current I_e^2

calorimeter. The second bump at lower energies is due to events that traverse the beampipe in the RCAL region before entering the BPC. The beampipe is made of $2\,mm$ steel, which at angles of $28\,mrad$ corresponds to additional four radiation lengths X_0. These positrons lose almost half their energy already in the beampipe. This effect will require some stringent position cuts in the data analysis.

The trigger slot 34 is quite similar: energy in the beampipe calorimeter with $t_{BPC} > -15\,ns$ and

more than $4.972\,GeV$ anywhere in the uranium calorimeter

and

a track in the central drift chamber

Again, the event must not be vetoed by either the C5 counter, the vetowall nor the SRTD. The differences among the different configurations for slot 34 in table C.1 are due to quality criteria on tracks (any track or good track) and vetowall veto.

11.6.2   SLT

The ZEUS Global Second Level Trigger (GSLT) does not impose cuts on the beampipe calorimeter data. It takes events from the GFLT slots 32 and 34. To reduce the rate, a prescale factor of 4 is applied. It does nevertheless global background rejection by cutting on global quantities like uranium calorimeter timing.

11.6.3   TLT

The ZEUS Third Level Trigger (TLT) takes the event from the GSLT. Depending on the preferences of the physics groups of ZEUS, different cuts are applied to the BPC data. The soft-photoproduction
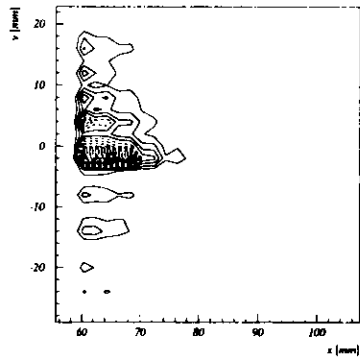
Figure 11.14: Contour plot of the hit position for monitoring trigger events

group opted to have a minimum bias sample and imposed no cuts but rather prescaled the events by another factor of 4. As for the GSLT, the TLT imposes some further background rejection cuts. Since at this stage the fully digitized information of ZEUS is available, these cuts can be more stringent than at the GSLT.

The effect of these cuts can be seen in figure 11.18, where the rate of events at the TLT output before prescaling can be found.

11.7   Trigger efficiency

As can be seen in table C.1 in appendix C the First Level trigger stage applied different cuts on different runs. For the determination of the total cross section only slot 32 is used. That slot had two distinct trigger configurations, namely 909032583 and 909032595 (noted as 583 and 595 in the following). The definition of these setups can be found in table C.2. The difference between configuration 583 and 595 is on the tracking requirements. Configuration 583 requires just any track in the central tracking detector in the branch in coincidence with energy anywhere in the uranium calorimeter (CAL_E). In the 595 setup, some quality requirement is on those tracks imposed.

There is no significant difference between the two configurations. Out of the 16 events that where taken in the 583 configuration, 13 events had a first level trigger multiplicity greater than zero. Out of those, only one event did not satisfy the more stringent requirements on the FLT track quality. Only 4% of the events in the final sample come through the part of the first level trigger slot 32 which imposes any requirement of the tracks. The inefficiency is therefore reduced to 0.3% which can be neglected.

The trigger efficiency of the beampipe calorimeter itself is difficult to determine since it had only one threshold level in its trigger logic and crosschecks with independent triggers have to take the incomplete Φ coverage into account. In order to stay clear of the region, where events might migrate over the trigger threshold, a three sigma cut is applied, fixing the lower energy cut at $11\,GeV$. It is assumed here that the trigger efficiency above $11\,GeV$ is 100%.
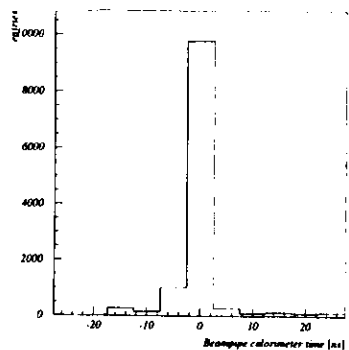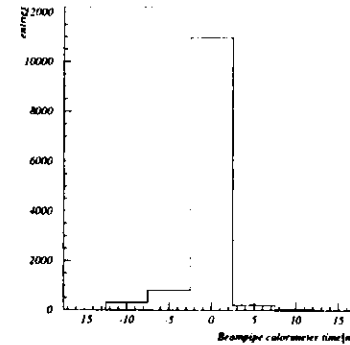

Figure 11.15: Timing distribution of BPC events in the GFLT trigger 32
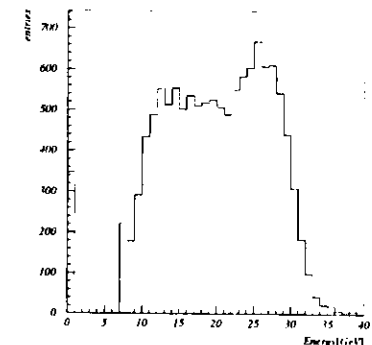
Figure 11.16: Calibrated energy spectrum of the beampipe calorimeter for the first level trigger slot 32

11.8   Deadtime determination

The datataking system of the ZEUS detector is designed so as to minimize deadtime in the front end readout by pipelining the analog information until the first level trigger decision has been calculated. In case of high rates the digitization of the pipelined data and the second and third level stage of the trigger system may introduce deadtime, when the data acquisition system can not accept new data. To take care of those situations, the deadtime is taken into account when calculating the accumulated luminosity by the ZEUS luminosity detector. The average deadtime in the run period used in this analysis (run 9560 – 10154) is 6.15%.

Since the beampipe calorimeter does not have a pipelined readout system, additional deadtime is introduced. In case an event[18] occurs while the preceeding one is still awaiting the GFLT decision the sample&hold circuitry is occupied. Inhibiting the GFLT until it has calculated the decision for the BPC trigger would make the ZEUS experiment experiencing the BPC deadtime as a whole, which is clearly not acceptable. Consequently the analog information of the new event cannot be sampled and is therefore lost. This situation has to be taken care of separately, and shall be called first order deadtime within this paragraph. Deadtime may also be introduced in case of a positive GFLT decision for which the BPC has data sampled. The ADC needs $330\,\mu s$ for a conversion of all channels, during which time the BPC readout system cannot sample the analog information of new events, this shall be denoted as second order deadtime.

12513 events satisfy the GFLT trigger slot 32 and the TLT bit 11 in the soft photoproduction stream (BPC trigger) and are the event pool used for this analysis. 12335 of those allow unambiguously[19] to identify the source of the interrupt in the state machine of the interface of the first level trigger, i.e. those events can be used for the deadtime determination. 141 events have no matching analog signal, when a positive trigger decision of the GFLT arrives for a trigger that originated from the BPC hardware, translating into 1.1% first order deadtime. An additional 79 events become accepted

---

[18]The beampipe calorimeter hardware signals the occurence of a trigger to the GFLT independent of the status of the BPC readout.

[19]No pile up has occured during the readout of the status of the interface.
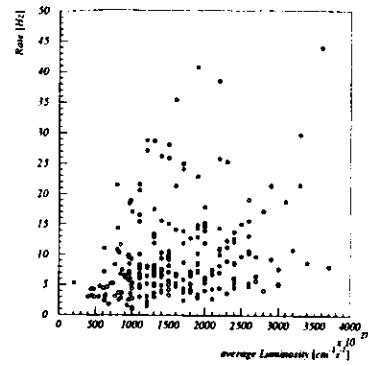
Figure 11.17: Rate of BPC trigger slot 32 at GFLT versus average luminosity
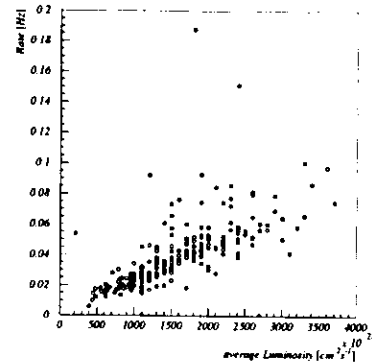
Figure 11.18: Trigger rate of BPC at third level photoproduction trigger versus average luminosity

by the GFLT while the BPC is still busy digitizing the previous event, resulting in 0.6% second order deadtime.

The total deadtime of the beampipe calorimeter is the sum of first and second order deadtime:

$$t_{dead} = 1.8 \pm 0.1\%. \tag{11.7}$$

11.9 Correction for the uranium calorimeter trigger

The first level trigger of the ZEUS uranium calorimeter (CFLT) overestimates the energy that is measured in the trigger cells. Therefore events below the nominal trigger threshold are accepted. In order to correct for this effect, the trigger simulation code is applied to the data as well. The trigger simulation code for the data uses as its input the correctly calibrated offline energy deposits in the calorimeter cells and assigns it to the trigger cells. Then the trigger algorithm is run on these trigger cells. Only events that satisfy this offline simulation are kept. The trigger simulation in Monte Carlo uses the calibrated energy as well. This allows a direct comparison of the data to the results from Monte Carlo studies.

The effect of the uranium trigger correction is small, only one event in the final data sample is rejected by the offline trigger simulation.

11.10 Radiation dose measurement

The beampipe calorimeter is fixed to the beampipe. It is hit by high energetic electromagnetic interacting and hadronic particles. Unlikely the main calorimeter of ZEUS, which is retracted by 40 cm during particle injection and ramping in HERA, the BPC is exposed to radiation during such times when backgrounds are particularly high. The dose due to ionizing radiation has been measured inclusively by glass dosemeters, type RPL R1T, that have been attached to the beampipe calorimeter and the beampipe itself. The dosemeters were obtained and analysed by the DESY radiation safety group D3.

Nine dosemeters were installed on January, 10th 1994, that is before HERA operation resumed in 1994. They were removed on June 6th during an access for taking out the BPC for repair. After replacement of the diodes and the front end electronics new dosemeters had been installed on July, 18th when the BPC was put back into ZEUS. Those dosemeters were replaced for the rest of the 1994 running period on August 30th. A tenth dosemeter remained in an office room as a control dummy.

The position of the dosemeters can be found in figure 11.19 and in [56]. Dosemeters 1 to 4 were sitting on the front plate of the beampipe calorimeter facing the interaction region.
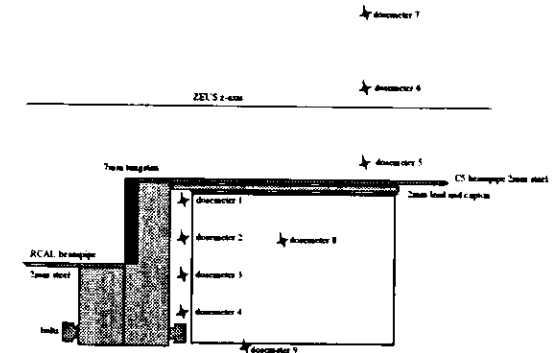
Figure 11.19: Position of the radiation dosemeters on the BPC

The distance of the dosemeters from the nominal beam center and their dose readings can be found in table 11.2.

Dosemeter	Distance from beam	Radiation dose			
		10.1.-6.6.	18.7.-30.8.	30.8.-5.12.	total 1994
#	[mm]	[Gy]	[Gy]	[Gy]	[Gy]
1	52	951	3400	3500	7851
2	72	468	1600	1000	3068
3	92	25	110	280	415
4	112	6	27	39	72

Table 11.2: Radiation dosemeters readings in 1994 (front dosemeters)

Since the diodes and the front end electronics of the calorimeter had to be replaced in summer 94, the accumulated dose for the diodes and the front end electronics has to be calculated from 18.7.94 on only.

The strip detector electronics have been replaced during the winter shutdown 1993/94 and therefore received the full 1994 dose.

Three dosemeters were placed on top of the beampipe itself, in front of the C5 collimator (seen from the interaction point). Their readings can be found in table 11.3.

There were two more dosemeter positions: one (= #8) on top of the beampipe calorimeter, 60 mm away from the front face and 40 mm away from the beampipe side. The other (= #9) was mounted

Dosemeter	Distance from beam	Radiation dose			
		10.1.-6.6.	18.7.-30.8.	30.8.-5.12.	total 1994
#	[mm]	[Gy]	[Gy]	[Gy]	[Gy]
5	40	246	700	640	1586
6	50	17	65	80	162
7	78	20	32	10	62

Table 11.3: Radiation dosemeters readings in 1994 (dosemeters on top of BPC)

on the side of the beampipe calorimeter facing away from the beampipe, near the power regulators.

Dosemeter	Radiation dose			
	10.1.-6.6.	18.7.-30.8.	30.8.-5.12.	total 1994
#	[Gy]	[Gy]	[Gy]	[Gy]
8	1.9	8.7	10.0	20.6
9	1.8	9.0	5.5	16.3

The control dosemeter in the office room had received a non measurable dose of < 0.1 Gy during all times.

The strip detector itself has been in the beampipe calorimeter since the datataking of ZEUS started in 1992. Table 11.4 shows the measured dose for 1993 and 1992 for locations comparable to the dosemeter positions in 1994. They exhibit the same exponential decrease with distance as in 1994. The overall dose is a factor 4 less in 1993 and factor 10 less in 1992. Most of the dose is being received during injection of the beams into HERA, which is indicated by the high counting rates of the C5 counter during injection. It consists of plastic scintillator, counting ionizing particles. Since the beampipe calorimeter, unlike the main calorimeter of ZEUS, cannot become retracted from the beampipe, it is hit by the beam halo particles when the collimators are still open.

Dosemeter	Radiation dose 1993	Radiation dose 1992
#	[Gy]	[Gy]
1	1903	910
2	627	
3	40.4	32
4	13.5	
8	9.7	
9	5.5	

Table 11.4: Radiation dosemeters readings in 1992 and 1993

The integrated electromagnetic doses are in the region where the performance of the diodes should start to degrade, see [60]. It is possible that the breakdown of the frontend electronics is due to radiation damage. Since the neutron flux could not be measured radiation damage might be even larger than indicated by the measured doses. It is also difficult to estimate it and the lifetime predictions of [60] for the diodes inside the beampipe calorimeter have a rather large error.

An attempt has been made to measure the dark current of the old diodes after replacing them. The dark current of all diodes was outside the range of the measuring station, which ends at $20\,\mu A$, except for the last layer, where the dark current could be measured to $4.5\,\mu A$. These values have to be compared to the dark current of a reference diode of the same production batch which showed a dark current of $27\,nA$.

When replacing the diodes, some solvent of a silicon paste used for making thermal contact of the diode ceramic card mounts with the tungsten of the calorimeter were found on the diode surface. This was possible due to capillary forces between the diode surface and a capton cover used for electrical insulation, probably speeded up by heat produced by the preamplifiers on the same ceramic cards. It is not known how well the lacquer shielding of the diodes is resistent to the solvents. The replacement diodes consequently were installed without using silicone paste.

12 Data selection

A number of cuts have been imposed for selecting the events in data and Monte Carlo.

12.1 Clustering

In figures 12.1 and 12.2 the energy in a cluster in equivalent charge is plotted for the three most energetic clusters. Only clusters of at most four hit strips in each strip detector plane are allowed. By doing so, one obtains good efficiency, while still requiring a small cluster, see table 8.1. The energy deposit is very similar to the one for $5\,GeV$ electrons in the testbeam (see figure 8.5), except that the mean is shifted to higher values since the positrons have up to $27.5\,GeV$.
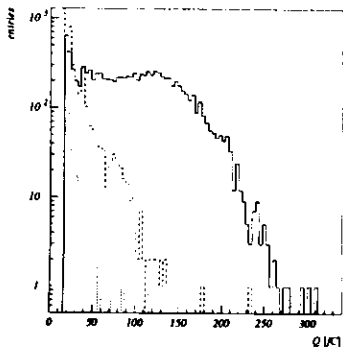
Figure 12.1: Energy deposited in the strips of a cluster in x for data in equivalent charge. The solid line is the most energetic cluster, the dashed lines are the second and third most energetic cluster.
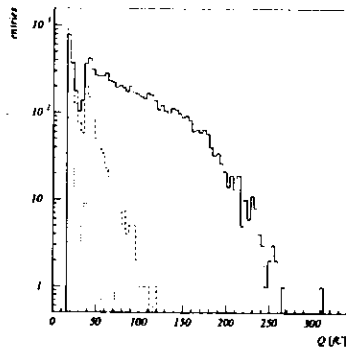
Figure 12.2: Energy deposited in the strips of a cluster in y for data in equivalent charge. The solid line is the most energetic cluster, the dashed lines are the second and third most energetic cluster.

Figures 12.5 and 12.6 show the distribution of the position of the most and second energetic cluster (up to four strips are allowed) in x. The shape of the hit distribution of the most energetic cluster is due to physics and detector geometry (see section 12.3). The hit distribution of the second cluster in x is flat with some enhancement around $85\,mm$, the position of the RCAL beampipe shadow.

The same is plotted for y in figures 12.7 and 12.8, both distributions flat except around $y = -5.1\,mm$ and $y = -17.1\,mm$, the positions of dead strips 7 and 10. The relative efficiency of

$$\epsilon_{rel} = 82\% \tag{12.1}$$

of the position finding of the y strips compared to the x plane is due to the two dead strips, which has to be compared with a theoretical relative efficieny of 83%.

The above leads to the conclusion, that the second cluster, which has significantly less energy than the first one, is mainly due to stray particles. Therefore it is sufficient to consider only the most energetic cluster for determining the position of the hit.
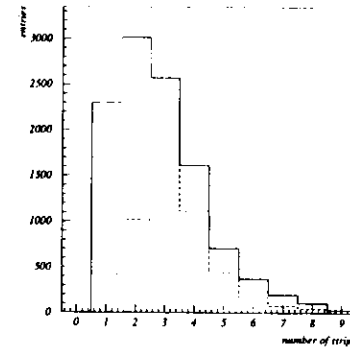
Figure 12.3: Distribution of number of hits in the most energetic cluster in x. Solid line for all positions, dashed lines with position cuts from section 12.3
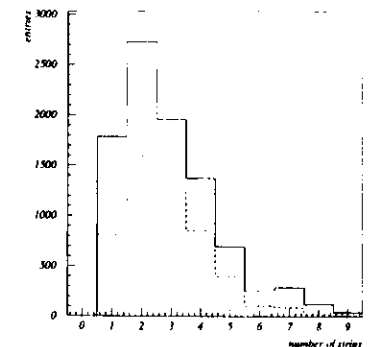
Figure 12.4: Distribution of number of hits in the most energetic cluster in y. Solid line for all positions, dashed lines with position cuts from section 12.3

In figures 12.3 and 12.4 the number of strips in the most energetic cluster is plotted. The solid line is for all positions, the dashed line with the position cuts of section 12.3. Compared to the result from the testbeam exposure (see figure 8.7) the maximum is shifted by one strip, which is not surprising since the positrons have higher energies than available in the testbeam. The y-strips have a reduced multiplicity due to the two dead strips.

12.2 Cluster quality cuts and position detector efficiency

The position finding efficiency is the product of the position finding efficiencies in the x and y planes. The cut of the strip multiplicity in a cluster is driven by the requirement of having a narrow cluster to ensure a good positron hit without much preshowering and to obtain a good efficiency at the same time. Keeping in mind the Molière radius $\rho_M \approx 9\,mm$, a good compromise is to allow at most 4 strips in the cluster in each plane.

The efficiency of finding such a cluster in each plane is given in table 8.1 on page 46 to

$$\eta_{plane} = 88.3 \pm 0.7\%. \tag{12.2}$$

Taking the relative efficiency $\eta_{rel} = 82\%$ between the x and y plane into account (see equation (12.1)), one obtains the position finding efficiency:

$$\eta_{pos} = \eta_{plane}^2 \cdot \eta_{rel} = 63.9 \pm 1.3\%, \tag{12.3}$$

where the error on the relative efficiency has been estimated to be 1%.

To check that the cluster quality cuts are independent of the energy deposit in the BPC, the percentage of events satisfying the cluster quality cuts is determined in different energy bins. To have enough statistical accuracy, the raw data sample with a hit position of $65\,mm < x < 80\,mm$ (to stay clear of

Figure 12.5: Positron position in x as determined by cluster algorithm for the most energetic cluster on raw data

Figure 12.6: Positron position in x as determined by cluster algorithm for the 2nd most energetic cluster on raw data

the beampipe shadow) is used. The bins and the ratio R of events satisfying the cluster quality cuts of at most 4 strips in the cluster in each plane is shown in table 12.1.

There is no systematic dependence on the energy. The mean value of 75.7% is higher than the result from the testbeam, since the raw data sample contains background events.

To check that the cluster finding efficiency from the testbeam measurement quoted in equation (12.3) is the same in data, the cluster quality cuts have been lifted in the final event sample. This procedure yields that $65.9 \pm 5.9\%$ of the events satisfy the cluster quality cuts, the error quoted is by statistics. This value agrees with the testbeam measurement.

12.3   Cuts on position coordinates in data

Restrictions in x come from the boundaries of the diodes and the RCAL beampipe shadow. Particles hitting the BPC traverse the 2 mm of steel of the beampipe at angles of $\approx 28\,mrad$. At those small angles the beampipe represents $4\,X_0$ dead material. The shadow of the RCAL beampipe can be seen in the data in figure 12.5 where the position of the most energetic cluster of at most four strips is plotted. The sharp cut at $x = 85\,mm$ is due to the shadow of the RCAL-beampipe in front of the BPC. This dictates the highest x for which events can be taken. Staying 8 mm away from that shadow fixes the upper cut on x at $x = 77.0\,mm$. This value has to be modified by position cuts dictated by the detector simulation in Monte Carlo, see section 12.4.

The lower cut on x is determined by the fiducial cut due to the migration effect in the position reconstruction described in section 10.3. The edge of the position detector at $x = 57.4\,mm$ plus the fiducial cut of 8 mm in x fixes the cut on x at $x = 65.4\,mm$.

In y no shadow is present, as can be seen in figure 12.7 showing the distribution of hits and figure 12.10, the mean energy deposit in data. The small dip in the distribution of the mean energy deposit is due to a small gap in between the calorimeter diodes present in the 1994 configuration.

The response is constant within the limits set by the energy resolution of the calorimeter, therefore no particular restriction on the y-hit position is necessary, except the cut for the migration effect of

E_{BPC} [GeV]	R [%]
11–23	75.7
7–11	79.3
11–13	79.9
13–15	72.2
15–17	72.5
17–19	75.4
19–21	76.4
21–23	77.8
23–25	79.1
25–27	72.9
27–29	73.6

Table 12.1: Percentage R of events in the raw data sample, satisfying the cluster quality cuts.

4 mm on both boundaries, leading to

$$-23.1\,mm < y_{hit} < 16.9\,mm. \tag{12.4}$$

12.4   Position cuts in Monte Carlo

The position cut for the Monte Carlo events used in the acceptance calculation, should be the same as in the data. Nevertheless it has to be checked whether there are further restrictions, since in the Monte Carlo detector simulation program Mozart version 12 used in this analysis, the RCAL beampipe was at a position of $x = 75\,mm$.

In figure 12.11 the mean energy deposit as a function of x is shown. The sharp drop at $x = 75\,mm$ is due to the shadow of the beampipe. The difference in shape to the corresponding plot for the mean energy deposit in data, figure 12.9, is due to the trigger. In data taking a coincidence with the ZEUS uranium calorimeter is required, therefore its acceptance causes the deformation in shape.

The position of the beampipe is different from the real situation and is corrected for in newer versions of the code (Mozart version ≥ 13.2). The beampipe position determines the maximum scattering angle up to where particles from the interaction point reach the BPC unobstructedly. The maximum x that can be used in the Monte Carlo is given by the position of the beampipe and the uncertainty (equation (8.2)) due to the position determination, and it is $x < 73\,mm$. This cut is lower than the one allowed by the data. Since the vertex offset of the data and the beam tilt are not present in the Monte Carlo (see section 12.5), this cut can be relaxed to $x < 75.3\,mm$ when transformed to the cuts for the real data, since

$$\Delta x = x_{data} - x_{MC} = x_{vtx} + z_{BPC} \cdot \tan\Theta_{tilt} = 2.3\,mm, \tag{12.5}$$

where z_{BPC} is taken from table 4.1 on page 23. In y and z the difference is governed by the vertex offset alone, since no vertical beam tilt has been observed.

$$\Delta y = y_{data} - y_{MC} = y_{vtx} = -1.3\,mm \tag{12.6}$$
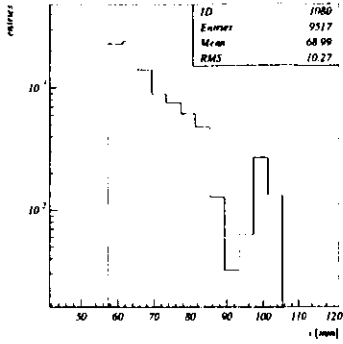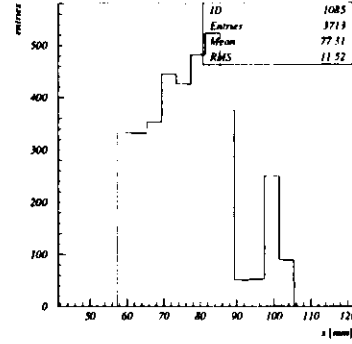
$$\Delta z = z_{data} - z_{MC} = z_{vtx} = -6.0\,mm \tag{12.7}$$
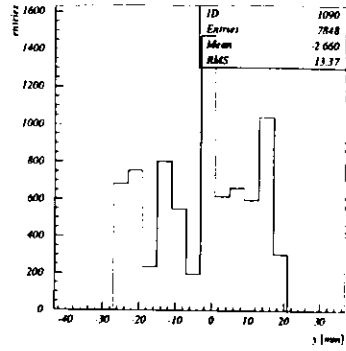
Figure 12.7: Positron position in y as determined by cluster algorithm for the most energetic cluster on raw data. The two dips at $-5.1\,mm$ and $-17.1\,mm$ are due to dead strips. The large number of entries around $y = 0$ are due to the 'hot spot' in raw data, compare with figure 11.14.
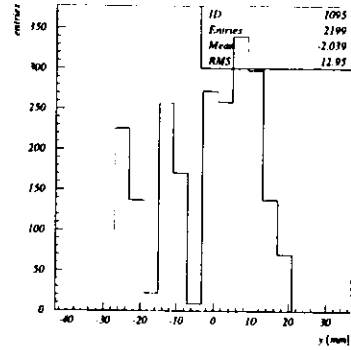
Figure 12.8: Distribution of hit position in y for raw data using the 2nd cluster. The two dips at $-5.1\,mm$ and $-17.1\,mm$ are due to dead strips.

The lower limit on x from the energy response in Monte Carlo is taken at that x for which the deviation from the mean energy deposit is within the limit given by the calorimeter energy resolution. At $20\,GeV$ the one standard deviation is $\sigma_E = 1.3\,GeV$. This allows to set the limit $x > 51\,mm$, which is much lower than that for data and can be well explained by the position of the BPC also being incorrect in the Mozart version used here.

The energy response in y is within one standard deviation, as allowed by the energy resolution of the BPC, therefore no restrictions are necessary:

$$-24\,mm < y < 24\,mm.$$

12.5 Final position cuts

The position cuts allowed by data (section 12.3) and Monte Carlo (section 12.4) differ significantly. The overlap of both determines the final cuts applied to data and Monte Carlo simulation.

The result for the position cuts on data are:

$$65.4\,mm \; < x < \; 75.3\,mm \tag{12.8}$$
$$-23.1\,mm \; < y < \; 16.9\,mm. \tag{12.9}$$

To transform these cuts to Monte Carlo use equations 12.5, 12.6, and 12.7.
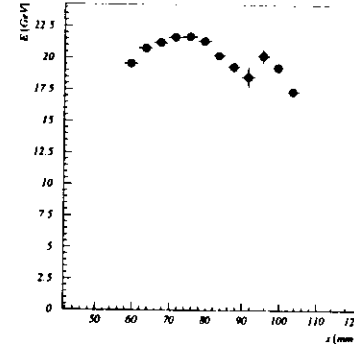
Figure 12.9: Mean energy response of the BPC versus hit position in x for data
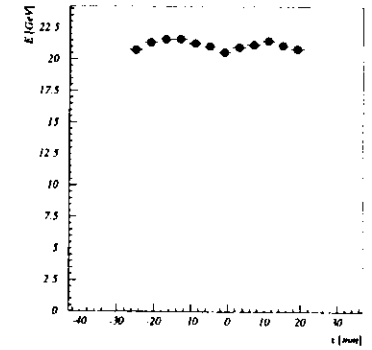
Figure 12.10: Mean energy response of the BPC versus hit position in y for data
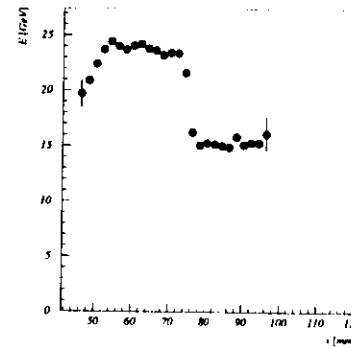
Figure 12.11: Mean energy response of the BPC versus hit position in x for Monte Carlo
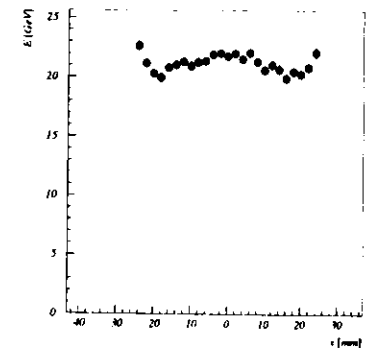
Figure 12.12: Mean energy response of the BPC versus hit position in y for Monte Carlo

12.6 Cuts on scattering angle

The crucial quantities for the cross section calculation as a function of Q^2 are the energy of the scattered positron E_e' and the scattering angle Θ. The cuts on the energy have been determined in section 12.7.

The range in scattering angle Θ is determined by the BPC geometry, which is shown in figure 12.13, where the area allowed by the position cuts of section 12.5 is marked. To get a uniform response in Θ, the minimum scattering angle Θ_{min} is governed by the minimum radius in the xy plane around the interaction point, that touches the upper and lower y boundary.

$$\Theta_{min} = 21.9\,mrad. \tag{12.10}$$

The maximum scattering angle Θ_{max} is determined by the radius at maximum x allowed.

$$\Theta_{max} = 23.9\,mrad. \tag{12.11}$$

These two values restrict the range of scattering angles taken in Monte Carlo and data. The sector in azimuth is not constant but varies with r. It is automatically taken care of in the acceptance calculation.
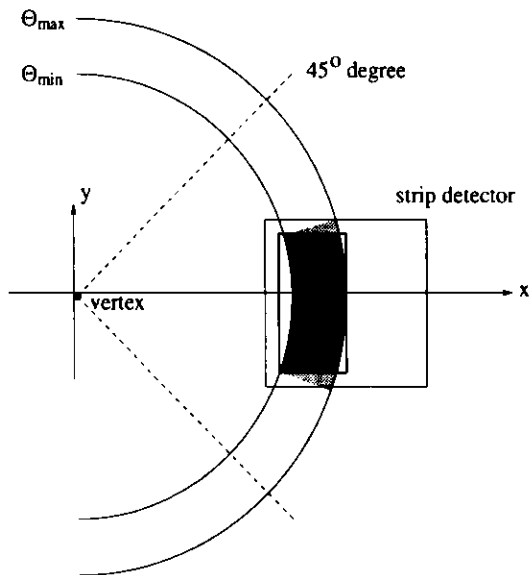
Figure 12.13: Determination of Θ_{min} and Θ_{max} for the acceptance calculation. The active area of the BPC is outlined by the thin solid line. The position cuts of equations 12.8 and 12.9 restrict the area to the box of the thick solid line.
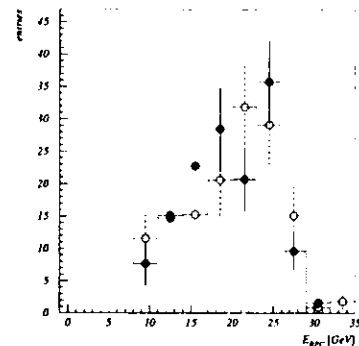
Figure 12.14: Energy distribution of the hits in the beampipe calorimeter. All final selection cuts except on the energy are applied. Filled circles are data. The open circles are from Monte Carlo, the dashed line is the Monte Carlo without cuts on the energy.
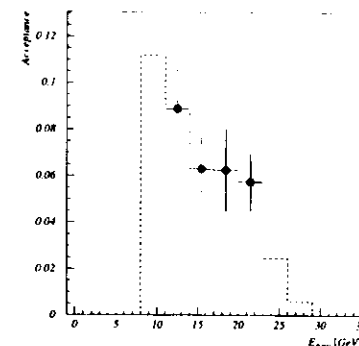
Figure 12.15: Energy acceptance for the events hitting the beampipe calorimeter. The histogram is the full energy range in Monte Carlo, the marks are shown for the energy range allowed by the cuts of equation (12.12)

12.7 Cut on BPC energy

The energy spectrum of the events when all cuts except on the beampipe calorimeter energy are applied is shown in figure 12.14, with filled circles for data. The spectrum as obtained from the Monte Carlo simulation is overlaid in open circles.

Dividing the data of the events accepted in Monte-Carlo (open circles in figure 12.14) by the number of events generated in the same energy bins in the Monte-Carlo simulation before application of the detector and trigger simulation yields the acceptance as a function of energy deposit in the BPC. This is plotted in figure 12.15. The rapid decrase of the acceptance above $23\,GeV$ is due to the acceptance of the main ZEUS calorimeter trigger. This fixes the upper boundary for the energy cut for the events used in the analysis. Also using the lower energy cut motivated by the BPC trigger efficiency (section 11.7), one obtains:

$$11\,GeV < E < 23\,GeV. \tag{12.12}$$

12.8 Timing

Halo particles stemming from interactions of the beams with the residual gas in the HERA beampipe accompany the colliding packets in- and outside of the beampipe. It is possible to suppress the hits by halo particles of the proton beam by using timing information from the TDC of the beampipe calorimeter readout system. In case those particles reach the BPC, they occur $\Delta t = 2 \cdot z_0/c = 20.4\,ns$ before the particles from an interaction at the vertex arrive at the beampipe calorimeter. The cut is already applied at the Global first level trigger at $t_{BPC} > -20\,ns$. The timing plot after the GFLT can be found in figure 11.15. For the final selection it is tightend to

$$|t_{BPC}| \le 10\,ns \tag{12.13}$$
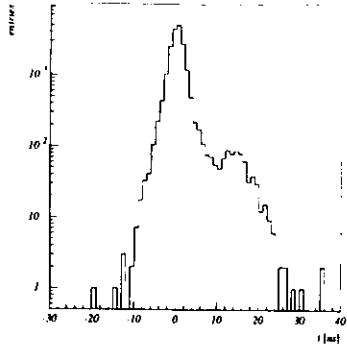
Figure 12.16: Timing distribution of particles arriving at FCAL

Figure 12.17: Distribution of energy deposits in the γ-tagger of the luminosity monitor of the raw data sample. The dashed line is the result of a Monte Carlo study that included radiative corrections on the generator level. The histogram is normalized to 1 in the first bin of the data.

Particles coming from interactions of the positron beam with the residual gas arrive at the same time as the products of the positron-proton collision at the BPC and can not be distinguished by timing of the BPC. But for the FCAL, sitting of the opposite side of the interaction point, the reverse is true. The same timing cut as on the protons can be done with the FCAL on the positrons. The timing distribution of the FCAL for all events is shown in figure 12.16. The arrival time of particles from the interaction is centered around zero. The second peak at around $15\,ns$ is due to positrons hitting the FCAL earlier (opposite timing convention compared with BPC). The timing cut imposed on the FCAL is therefore

$$t_{FCAL} \leq 10\,ns, \tag{12.14}$$

if the FCAL provides timing information.

Due to the aperture of the FCAL, not all positron beamgas events hit the calorimeter. Those beamgas events can be taken care of only by statistical subtraction as described in section 14.2.1.

12.9 Vertex cut

From figure 11.1, one can deduce the cuts on the vertex position. For this analysis, the cuts are choosen at plus/minus three standard deviations around the central value (in ZEUS coordinates).

$$
\begin{aligned}
|vtx_x - 1.5\,mm| &< 3.7\,mm \\
|vtx_y + 1.3\,mm| &< 3.2\,mm \\
|vtx_z - 6.0\,mm| &< 307.0\,mm
\end{aligned}
\tag{12.15}
$$

Since the vertex distributions in figure 10.10 for the Monte Carlo simulation are similar, the same cuts are used there, with a different offset, of course:

$$
\begin{aligned}
|vtx_x - 0\,mm| &< 3.7\,mm \\
|vtx_y - 0\,mm| &< 3.2\,mm \\
|vtx_z + 17\,mm| &< 307.0\,mm
\end{aligned}
\tag{12.16}
$$

12.10 Cut on $E - p_z$

By energy and momentum conservation

$$E - p_z = 2 \cdot E_e. \tag{12.17}$$

E is the total energy recorded by the calorimeters of the detector. To obtain p_z the individual energy deposits are multiplied by $\cos\theta$ and summed thereafter, where θ the polar angle with respect to the proton beam direction. This formula is sensitive mostly to energy deposits in the backward direction. Energy deposits in the FCAL beampipe region cancel, in the RCAL beampipe region contribute twice ($\cos\theta \approx -1$). From this it is clear that $E - p_z$ is insensitive to energy leakage through the forward beampipe hole whereas the opposite is true for particles escaping through the RCAL beampipe hole. By reaction kinematics (low Q^2) it is expected that the photon remnant will most likely show up in the RCAL beampipe region. Therefore, no low $E - p_z$ cut is applied.

For high $E - p_z$ the cut suppresses overlay events, where two events (e.g. physics and positron beamgas) occur during the same bunch crossing. The width of the $E - p_z$ distribution for all events in this analysis before the event selection is applied is determined by fitting a Gaussian. The maximum allowed $E - p_z$ is 3σ of this distribution away from $2E_e$ which results in

$$E - p_z < 72.5\,GeV. \tag{12.18}$$

12.11 Bremsstrahlung and luminosity monitor coincidences

The Bremsstrahlung process $ep \to e'p\gamma$ has a very high cross section. Since it decreases very rapidly with scattering angle ($\sim \theta^{-3}$), direct hits of the BPC have a negligible rate. To veto accidental coincidences some cuts on the counters of the ZEUS luminosity monitor are imposed.

The photon and the positron of a Bremsstrahlung event can end up in the gamma- respectively the positron-tagger of the ZEUS luminosity monitor. In 0.7% of the events of the initial sample (no selection cuts applied) the sum of the energies in the positron- and γ-tagger of the luminosity monitor is between $25\,GeV$ and $30\,GeV$. This gives an estimate of the rate of accidental coincidences. To get the actual rate, this value has to be divided by the acceptance of the luminosity monitor in coincidence mode, which is

$$A_{Lumi} = A_e \cdot A_\gamma. \tag{12.19}$$

The acceptance of the γ-tagger $A_\gamma = 99\%$ is given by geometry [66]. The acceptance of the electron tagger A_e is taken from an acceptance study for photoproduction events at very small Q^2 to $A_e \approx 100\%$ [57]. Therefore events that have an accidental Bremsstrahlung coincidence in the same bunch crossing can be effectively vetoed by imposing

$$E_\gamma^{Lumi} < 1\,GeV \tag{12.20}$$

$$E_e^{Lumi} < 1\,GeV. \tag{12.21}$$
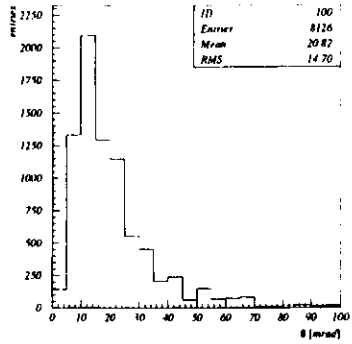
Figure 12.18: Angle between photon and outgoing positron for initial state radiation
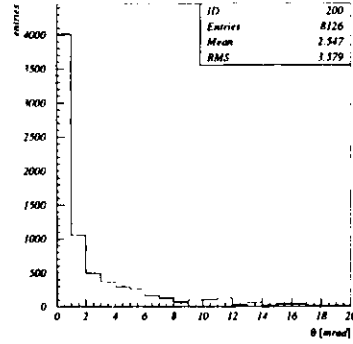
Figure 12.19: Angle between photon and outgoing positron for final state radiation

12.12 Radiative corrections

The distribution of energy deposits E_γ in the luminosity γ-tagger of the initial event sample (no selection cuts applied) is shown in figure 12.17. Not all of the events that have more than $1\,GeV$ in the γ-tagger are due to overlays of Bremsstrahlung events as mentioned in section 12.11. The Bremsstrahlung coincidence events are responsible for about 20% of the events with $E_\gamma > 1\,GeV$. The remainder stems from inital state radiation of photons by the incoming positron. The acceptance of the γ-tagger is about 50% [57] for these photons being scattered at very small angles. To estimate the necessary radiative corrections a Monte Carlo study is performed.

Inital and final state radiative events have been generated using HERACLES 4.4 [48] interfaced to LEPTO 6.1[46] via the program DJANGO6 [23]. The distribution of the angle between the radiated photon and the outgoing positron is shown in figure 12.18 for initial state radiative events and in figure 12.19 for final state radiation. For final state radiation the photon is almost collinear with the outgoing positron, the mean angle is only 2.5 mrad which corresponds to 7.6 mm at the beampipe calorimeter. The cuts on the beampipe calorimeter hit position ensure, that the photon is hitting the calorimeter as well as the positron for those events. Therefore the effect from final state radiation is small. For initial state radiation, the mean angle is 20.8 mrad. This leads to the photon escaping through the beampipe while the positron is entering the e-p collision at reduced energy.

The energy spectrum of energy deposits in the γ-tagger for Monte Carlo events is shown as the dashed line in figure 12.17. The agreement with data is good. The cut on the energy deposited in the γ-tagger in (12.20) removes the radiative events which deposit energy there.

As Monte Carlo studies [49, 22] and photoproduction data analysises [17, 57] have shown, another cut to suppress radiative corrections is to require some energy deposited in the RCAL. The cut used there is

$$E_{RCAL} > 1\,GeV. \tag{12.22}$$

This ensures by energy and momentum conservation that the exchanged photon has a least an energy of $E_{\gamma^*} = 1\,GeV$. The effect of this cut on the data can be seen in figure 12.20, 39% of the events are removed when imposing (12.22).
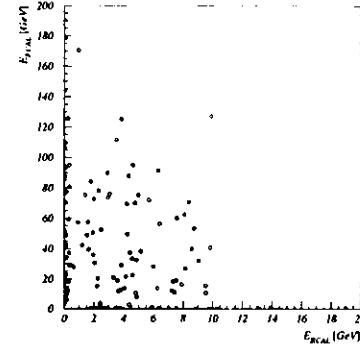
Figure 12.20: Energy in the FCAL versus energy in the RCAL for the final selection of events in data when the $E_{RCAL} > 1\,GeV$ cut is not applied.
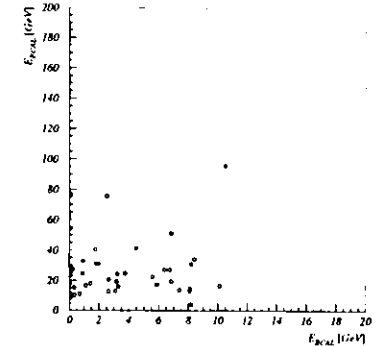
Figure 12.21: Energy in the FCAL versus energy in the RCAL for the final selection of events in Monte Carlo with radiative corrections when the $E_{RCAL} > 1\,GeV$ cut is not applied. (DJANGO generator, not including diffraction)

The Monte Carlo study with radiative corrections included shows within statistics the same behaviour as can be seen in figure 12.21. The difference in the spectrum of energy deposits in the FCAL between the data and this Monte Carlo is due to diffractive events. There exists no Monte Carlo program for diffractive events at the moment that has radiative corrections included. The Monte Carlo that is used in the acceptance calculation (Pythia and Herwig, see section 13) has the diffractive events included but, unfortunately, no radiative corrections. The event distribution for those Monte-Carlo events can be seen in figure 12.22. The spectra in FCAL and RCAL agree with data when the cut of equation (12.22) is applied.

From these Monte Carlo studies it is estimated that while $10 \pm 4\%$ of the non-radiative events are lost, $62 \pm 35\%$ of events with radiative corrections are suppressed. The conclusion is that in the final event sample $11 \pm 7\%$ of the events will have a photon radiated from the incoming electron.

12.13 Spectra of measured quantities

Figure 12.23 shows the quantity $E - p_z$, which by conservation laws should be $2 \cdot E_e$. The distribution does not peak at the theoretical value of $55.0\,GeV$ which is due to the photon remnant escaping partially undetected the ZEUS detector. This is demonstrated by the Monte Carlo distribution shown as an overlay.

Figure 12.24 shows the time of the events in the BPC versus the time from the corresponding hits in RCAL. The energy spectrum in the range used for the cross section analysis is shown in figure 12.25.

The distribution of the scattering angle of the positron in data and Monte Carlo can be found in figure 12.27. The scattering angle is calculated by the hit position of the BPC, figure 12.26, seen from the vertex position of $x = 1.5\,mm$, $y = -1.3\,mm$ corrected for the beamtilt. Due to the position reconstruction resolution of $\sigma_x = \sigma_y = 1.9\,mm$ only two bins are employed. Together with the energy this yields the Q^2 spectrum, which can be found in figure 12.28.
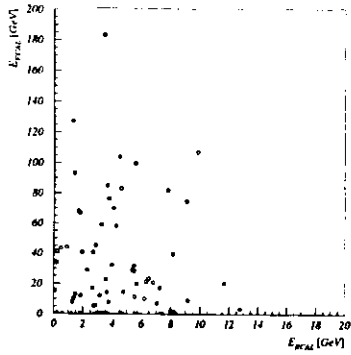
Figure 12.22: Energy in the FCAL versus energy in the RCAL for the final selection of events in Monte Carlo without radiative corrections when the $E_{RCAL} > 1\,GeV$ cut is not applied. (Pythia and Herwig, including diffractive events)
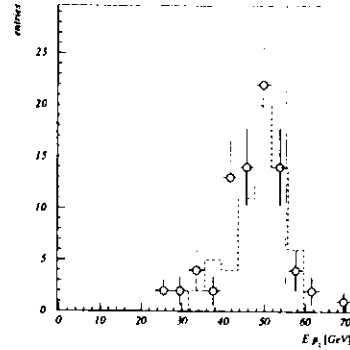
Figure 12.23: Distribution of $E - p_z$ in the final event sample, the line is at $2E_e = 55.04\,GeV$. The dashed line is the result of the Monte Carlo simulation.

The center of mass energy W of the γ^*p system is shown in figure 12.29. It is computed by

$$W = \sqrt{y \cdot s},\tag{12.23}$$

where y is determined by the energy deposit in the BPC and $s = 9 \cdot 10^4\,GeV^2$ the center of mass energy squared of the positron proton collision.
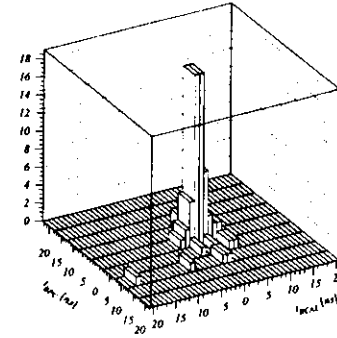
Figure 12.24: Beampipe calorimeter timing versus RCAL timing for events in the final sample
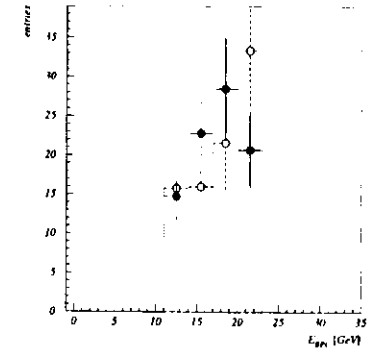
Figure 12.25: Energy distribution of the final event sample in the beampipe calorimeter. Filled circles are data, the open circles are from Monte Carlo simulation.
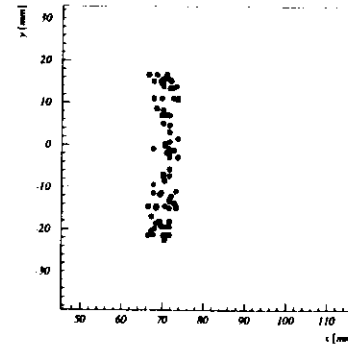
Figure 12.26: Distribution of hit position of events in the final sample
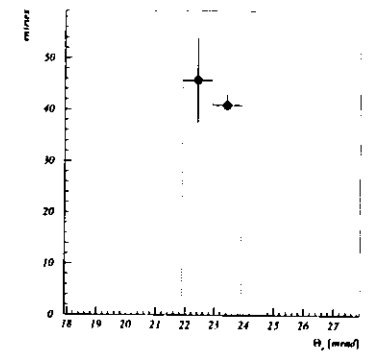
Figure 12.27: Distribution of the scattering angle for hits in the beampipe calorimeter. Filled circles are data, the Monte Carlo result is shown as a dashed line.
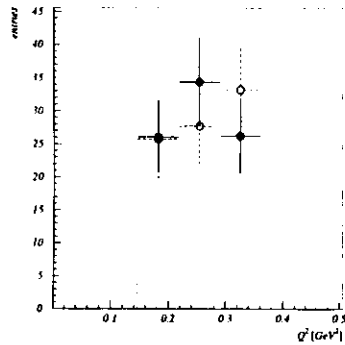
Figure 12.28: Q^2 spectrum of the final event sample plotted as full circles, corrected for strip detector acceptance (table E.1). The dashed line represents the result from the Monte Carlo simulation.
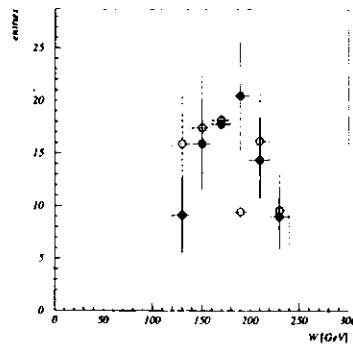
Figure 12.29: $\gamma^* p$ center of mass energy W of the final event sample. The dashed line is from the Monte Carlo simulation.

13 Acceptances

The acceptance is defined as the number of Monte-Carlo events satisfying the event selection criteria, applied in exactly the same way as on the data, divided by the number of generated events in the same kinematical range. Therefore the response of all detectors, e.g. BPC, uranium calorimeter, drift chambers, to the particles from the event generators has to be simulated.

The trigger is simulated as well, using the ZEUS trigger simulation program ZGANA. Since the second and third level trigger stage did not make any cuts but applied only prescale factors to the data used for the determination of the total ep cross section, only the first level trigger stage simulation has to be used.

The events used in the acceptance simulation have been produced using Pythia [74] and Herwig [58] Monte-Carlo event generators. The following processes are taken into account with relative contributions as determined in [85]:

Non-diffractive events: 64%

Elastic diffraction: 13%
The three lightest vector mesons are generated with a ratio of $\rho : \omega : \phi = 17.2 : 1.5 : 1$ (Pythia default)

Inelastic diffraction: 23%
The individual contributions are:

40% γ dissociation

40% proton dissociation

20% double dissociation

The non-diffractive events have been simulated using Herwig version 5.8. This is a minimum bias event generator, using a cylindrical phase phase and a parametrization of particle multiplicities and p_t distributions. The number of charged particles n in the final state is chosen according to a negative binomial distribution. The mean value $\langle n \rangle$ of that distribution is a function of the center of mass energy W of the hadronic system reduced by the mass of the two colliding particles $M = W - m_1 - m_2$:

$$\langle n \rangle = 0.207 \cdot (\log M)^2 + 0.431 \cdot \log M + 0.86 \tag{13.1}$$

It has been deduced from a fit to ZEUS photoproduction data and hadron-hadron results.

The transverse momenta of the particles are taken from the probability distribution

$$\frac{dP}{dp_t^2} \sim \exp(-5.1 \cdot \sqrt{p_t^2 + m^2}), \tag{13.2}$$

where m stands for the mass of the particle. The longitudinal momenta are generated flat in rapidity space.

Pythia version 5.6 is being used for generating the diffractive processes. In order to make Pythia simulate scattering of virtual photons off the proton in ep collisions in the kinematical range the BPC is operating at, some modifications have become necessary since standard Pythia allows only for direct and resolved hard photon proton processes. Also, the scattered positron is fixed to be collinear with the initial one. To allow the simulation of soft processes, the following strategy is being pursued: first, a scattered positron is generated using the ALLM cross section parametrization [1]. The four-vector

of the scattered positron is computed, assuming $m_\gamma = 0\,GeV$. At the Q2 range of the BPC, this leads to violations of momentum conservation on the order of 50 MeV. The generated photon is fed into Pythia and a real photon proton process is generated.

The radiative corrections have been computed using HERACLES [48] interfaced to LEPTO [46] via the program DJANGO6 [23].

In order to speed up the calculation of the BPC acceptance the diffractive events have been restricted to the kinematical range of $0.05 < Q^2 < 1\,Gev^2$ and $3.0 \cdot 10^{-4} < y_{Bj} < 0.8$. The scattering angle of the positron has been restricted in azimuth to $\pm45°$ around the positive x axis. The non-diffractive events fill the phase space of $0.05 < Q^2 < 1\,Gev^2$ and $0.01 < y_{Bj} < 1$, while no restriction on the scattering angle has been imposed. The events for studies of radiative corrections are generated with $Q^2 > 0.05\,Gev^2$ and $0.05 < y_{Bj} < 0.8$.

All the aforementioned physics processes have been generated separately. For the acceptance calculation the events have been mixed with appropiate weights to reproduce the correct event fractions. The number of events in a fixed kinematical range $(0.1 < Q^2 < 0.5\,Gev^2$ and $0.05 < y_{Bj} < 0.6)$ and with the restriction of the scattering angle of the positron of $\pm45°$ around the positive x axis have been determined for each process.

The weights for the events of the different processes have been calculated in such a way that the weighted number of events of all processes end up to the total number of events generated and the weighted number of events for each individual process represents the right fraction as given above. The result can be found in table D.1 in appendix D.

13.1 Clustering acceptance

As already described in section 10.3, the acceptances for the reconstructed cluster positions have been calculated on a $4 \times 4\,mm^2$ grid from a special Monte Carlo. The result can be found in table E.1 in appendix E. For the cross section calculations these acceptances are taken into account on an event by event basis.

The overall clustering acceptance shall be estimated in the following: the clustering algorithm leads to migrations in the hit positions at the edges of the strip detectors. Events that have their true hit position outside the area defined by the final position and angular cuts (section 12.5 and 12.6) may have a reconstructed position inside, and vice versa. The final position cuts (equations 12.8 and 12.9) applied to the true hit position result in 16001 hits. To be independent of the cluster finding efficiency, the cluster quality cuts (less than 4 strips in x and y in the most energetic cluster) are already applied. Requiring the reconstructed cluster position to be within the position cuts yields 16064 hits. This is a migration of 0.4%. If the angular cuts of equations (12.10) and (12.11) are required in addition, 9997 events become accepted in the true quantities, compared to 10600 events after the clustering. The net clustering acceptance is therefore

$$A_{clust}^{net} = 106.0\%. \tag{13.3}$$

13.2 Q^2 binning

Q^2 is measured by

$$Q^2 = 2 \cdot E_e \cdot E_{BPC} \cdot (1 - \cos\Theta_{BPC}), \tag{13.4}$$

where $E_e = 27.52\,GeV$ the energy of the positrons in HERA.
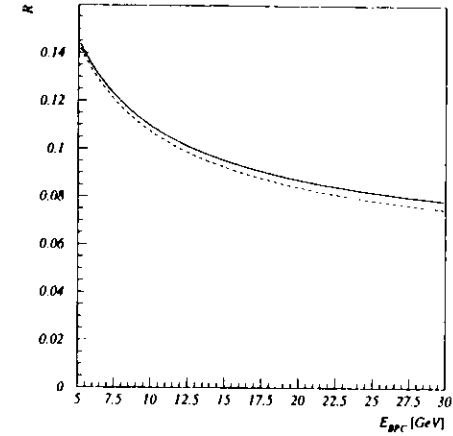
Figure 13.1: Q^2 resolution of the beampipe calorimeter. Plotted is $R = \sigma_{Q^2}/Q^2$ versus energy in the BPC. Solid line for largest possibles scattering angle Θ, dashed line for smallest Θ.

The accessible range of scattering angles is determined by the cuts in section 12.6. The minumum Q^2 follows from the minimum energy allowed by equation (12.12) and Θ_{min}:

$$Q^2_{min} = 0.15\,GeV^2, \tag{13.5}$$

the maximum is given by the maximum energy allowed by equation (12.12) and Θ_{max}:

$$Q^2_{max} = 0.36\,GeV^2. \tag{13.6}$$

The width of the Q^2 bins is determined by the position and energy resolution of the beampipe calorimeter. The resolution is given by

$$\sigma_{Q^2} = \sqrt{\left(\frac{\partial Q^2}{\partial E'} \cdot \sigma_{E'}\right)^2 + \left(\frac{\partial Q^2}{\partial x} \cdot \sigma_x\right)^2 + \left(\frac{\partial Q^2}{\partial y} \cdot \sigma_y\right)^2} \tag{13.7}$$

The relative resolution $R = \sigma_{Q^2}/Q^2$ is plotted in figure 13.1 versus the energy in the BPC. The solid curve corresponds to the hit positions at smallest scattering angle Θ_{min} ($x = 65.4\,mm, y = -23.1\,mm$). The dashed line corresponds to Θ_{max} ($x = 75.3\,mm, y = -1.3\,mm$) allowed by the box cuts of section 12 for an interaction point at the equivalent vertex position (equation (11.3)).

Since the events taken are above $11\,GeV$, 10% relative Q^2 resolution is used for the uncertainty in the Q^2 determination. The Q^2 bins are choosen to be twice as wide. Taken at Q^2_{max} an upper limit for the bin width is derived: $0.07\,GeV^2$. Table 13.1 gives the bin boundaries.

	lower bound	upper bound
bin 1	0.00	0.07
bin 2	0.07	0.15
bin 3	0.15	0.22
bin 4	0.22	0.29
bin 5	0.29	0.36
bin 6	0.36	0.44
bin 7	0.44	0.51

Table 13.1: Q^2 bin boundaries

13.3 Q^2 acceptance

Dividing the distribution of events being accepted in Monte Carlo by the generated Q^2 distribution with the cuts on energy and polar angle Θ at the generator level applied yields the acceptance for the total cross section determination in bins of Q^2. This is done at various steps of the data selection to discriminate between the different cuts.

The same cuts that are applied to the data are used on the reconstructed quantities in the Monte Carlo, as described in section 12. To simulate the effect of the trigger, the requirements of the FLT slot 32 are applied to the trigger data provided by the ZGANA trigger simulation. The details can be found in appendix C, here the configuration '595' is used.

The acceptance averaged over the range $0.15 < Q^2 < 0.36$ is

$$\mathcal{A}_{Q^2} = 6.3 \pm 0.9\%. \tag{13.8}$$

The number of events[20] and their associated statistical error, both for generated and accepted events, are shown in table 13.2. The resulting overall acceptance $\mathcal{A}_{Q^2}$ with statistical errors is listed as well.

Q^2 [GeV^2]	events accepted	events generated	$\mathcal{A}_{Q^2}$ [%]
0.145–0.218	19.1±4.5	209.5±18.9	9.13±2.28
0.218–0.290	20.6±5.0	425.1±28.0	4.85±1.21
0.290–0.363	24.7±5.2	395.5±26.4	6.24±1.38
0.145–0.363	64.4±8.5	1030.2±42.9	6.26±0.86

Table 13.2: Acceptance of the beampipe calorimeter for the bins in Q^2 used for the determination of the total cross section. The error on the events is statistics folded with the relative weights of the samples from the different generators. Trigger simulation and data selection cuts are explained in the text.

The decomposition of the acceptance from

$$\mathcal{A}_{Q^2} = A_{geom} \cdot \mathcal{A}_{trig} \cdot \mathcal{A}_{cuts} \tag{13.9}$$

with A_{geom} being the geometrical acceptance, $\mathcal{A}_{trig}$ the trigger acceptance, and $\mathcal{A}_{cuts}$ the acceptance of the remaining data selection cuts of section 12 is listed in table 13.3. The acceptance of each level is taken after the cuts of the preceeding data selection are already applied.

[20]The number of events are the number of entries in each bin weighted by the appropiate weight of the generator sample, see table D.1 in appendix D.

Q^2 [GeV^2]	A_{geom} [%]	$\mathcal{A}_{trig}$ [%]	$\mathcal{A}_{cuts}$ [%]	$\mathcal{A}_{Q^2}$ [%]
0.145–0.218	12.2±2.7	90.7±26.4	82.2±25.9	9.13±2.28
0.218–0.290	8.1±1.5	80.6±21.9	74.2±23.4	4.85±1.21
0.290–0.363	25.3±3.1	85.2±12.0	28.9± 6.9	6.24±1.38
0.145–0.363	15.6±1.3	85.7± 9.9	47.3± 7.1	6.26±0.86

Table 13.3: Acceptance decomposition. The total acceptance $\mathcal{A}_{Q^2}$ is divided into acceptance after applying the geometry cuts A_{geom}, the acceptance after the trigger simulation $\mathcal{A}_{trig}$ and the acceptance of the remaining data selection cuts $\mathcal{A}_{cuts}$ using $\mathcal{A}_{Q^2} = A_{geom} \cdot \mathcal{A}_{trig} \cdot \mathcal{A}_{cuts}$. Errors by statistics only.

13.4 Check of the acceptance calculation

To check the acceptance calculation, a second, different method is used. The idea is to use all Monte Carlo events that are accepted in the ±45° sector between Θ_{min} and Θ_{max} in figure 12.13 and rescale that acceptance by the theoretical geometrical acceptance of the BPC area allowed by the data selection cuts. Since the BPC occupies less than 45° in Φ, the cuts for the BPC have to be applied on true quantities at the generator level.

The events become accepted, if the true scattering angle Θ_{true} of the positron seen from the interaction vertex is

$$\Theta_{min} < \Theta_{true} < \Theta_{max}, \tag{13.10}$$

where Θ_{min} and Θ_{max} are given by equations 12.10 and 12.11. A cut on the azimuthal angle Φ is applied as well to account for the fact that the beams pass off axis through the ZEUS detector. The events have to satisfy

$$\Phi_{true} \in [-45°, 45°]. \tag{13.11}$$

The data selection cuts of section 12 are imposed as long as they are not concerning BPC quantities. The trigger simulation of ZEUS must also give a positive decision. The acceptance is determined as a function the true positron energy. On the generated events only the cut on the scattering angle Θ_{true} is applied.

To reduce the influence of bin to bin migrations, the acceptance is averaged over energies from $11\,GeV$ to $23\,GeV$. The acceptance for an event to hit the BPC at the generator level and to trigger ZEUS is given by

$$\mathcal{A}_{sel} = 18.3 \pm 1.6\%. \tag{13.12}$$

The theoretical geometrical acceptance for the events with the cuts on Θ and Φ as described in equations 13.10 and 13.11 is

$$A_{\pm 45°} = 25\%. \tag{13.13}$$

The difference between this number and the acceptance $\mathcal{A}_{sel}$ is the effect of the ZEUS trigger and the data selection cuts, i.e. 27% of the events are lost due to the trigger acceptance and cuts on quantities like timing and energy deposits in the main calorimeter of ZEUS and vertex position.

The acceptance of the BPC by geometry alone is the dark shaded area allowed by the data selection cuts in figure 12.13 divided by the area enclosed between Θ_{min} and Θ_{max}. It is

$$A_{area} = 9.35\%. \tag{13.14}$$

To get the final acceptance A_{sel} has to be scaled. The scaling factor is the geometrical acceptance A_{area} divided by the acceptance $A_{\pm 45°}$:

$$f = \frac{A_{area}}{A_{\pm 45°}} = 0.37, \tag{13.15}$$

resulting in

$$A = f \cdot A_{sel} = 6.84 \pm 0.60\%. \tag{13.16}$$

The numbers obtained here differ somewhat from the values obtained in table 13.3. But this is understandable since this cross check is free of migration effects. It is worth noting that the final values of the average acceptance in equation (13.16) and (13.8) agree within statistics, i.e. the effect of the migrations is handled correctly.

14 Determination of the total $\gamma^* p$ cross section

The total cross section for electroproduction σ_{ep} will be calculated in this chapter. Starting from there, it is possible to calculate the cross section for the reaction of virtual photons with protons $\sigma_{\gamma^* p}$. This can be compared to measurements by other experiments. Invoking the vector dominance model it is possible to compare with the real photoproduction cross section.

14.1 Luminosity determination

The total luminosity accumulated by ZEUS in the runs used in this analysis is $1.94\,pb^{-1}$, where the ZEUS deadtime has already been taken into account. For details see [66]. The beampipe calorimeter triggers had been prescaled. The nominal prescales at the first, second and third level of the trigger was 4 at each level, amounting to a total of 64. This number has to be corrected for a peculiarity in the third level trigger stage, which ran as a parallel processing farm. Each of the processors applied its own prescaling accounting, which is done by a random number generator. Nonetheless, the first event showing up on each of the processors was taken without the prescaling being applied. For shorter runs with only few events from the beampipe calorimeter trigger being written out, these 'first' events account for a sizeable fraction of the total event sample, therefore reducing the effective prescale. In figure 14.2 the effective prescale factor for the whole trigger chain versus integrated luminosity in the run is plotted. For some runs, the TLT prescaling was turned off, rendering a constant overall prescale factor of 16. The effective overall prescale factor for the events in this analysis is 49.6.

For calculating the effective integrated luminosity the effective prescale factor has been applied on a run by run basis. The effective integrated luminosity of all runs in this analysis is then

$$\mathcal{L}_{eff} = 39.2 \pm 0.4\,nb^{-1}. \tag{14.1}$$

14.2 Background studies

The main sources of background are beamgas reactions and photoproduction events with $Q^2 = 0\,GeV$. In beamgas events the incoming electron does not collide with a proton but the residual gas in the beampipe. In photoproduction events the photon remnant may hit the BPC and can be therefore be mistaken as the scattered electron.

14.2.1 Beamgas events

Beamgas events are hard to discriminate from ordinary events, if they occur close to the interaction point. To account for these beamgas events, statistical subtraction using the pilot bunches has to be employed. Pilot bunches are unpaired positron or proton bunches, where the bunch of the other particle species is not filled. HERA operated in 1994 with slighthly varying pilot bunch configurations, most of the times it has been filled with

- 153 positron-proton bunches
- 15 positron pilot bunches
- 17 proton pilot bunches.

The statistical background subtraction looks for events that survive all selection cuts and still originate from a pilot bunch. Such events get a negative weight of the current contained in all positron-proton bunches devided by the current in all pilot bunches of the corresponding type (electron or proton).:

$$\mathcal{W} = \frac{I_{ep}}{I_{pilot}}. \tag{14.2}$$

In the final event sample no events stem from pilot bunches. But it is a problem of statistics since there is about ten times more current in the colliding bunches than in the pilot bunches. To estimate the background a bigger sample has to be choosen. The cuts on the hit position and the energy deposit of the BPC should not cut strongly into the beamgas spectrum above the BPC trigger energy threshold. Therefore all hits on the ZEUS detector quantities are used (calorimeter energy and timing, vertex, FLT trigger slot 32, TLT slot SPP11) while on the BPC only the timing cut is applied. 1993 events remain, with no events coming from the proton pilot bunches and 14 stemming from positron pilot bunches, which have a negative weight of $W = 9.25$. The beamgas contamination is therefore

$$C_{bkg} = 6.5 \pm 1.7\%. \tag{14.3}$$

This amount of background corresponds to 0.59 ± 0.16 events in the final sample of 81 events, which is in agreement with no event found associated with pilot bunches.

14.2.2 Photoproduction background

Photoproduction background is studied, by subjecting Monte Carlo event samples to the selection cuts of this analysis. Different Monte Carlo samples are used, namely HERWIG diffractive and nondiffractive [58], and a Monte Carlo based on the Nikolaev-Zakharov model [36] as a cross check for model dependence. The Q^2 range is $0 < Q^2 < 0.02\,GeV^2$ and the range in $y_{Bjorken}$ is $0.35 < y < 0.56$.

Of the 17667 nondiffractive and 19516 diffractive HERWIG events none satisfies the data selection cuts. Taking into account that the events have been given different weights according to their contribution to the total cross section, this leads to an upper limit of the acceptance for photoproduction events:

$$A_{SPP} < 1.8 \cdot 10^{-5}. \tag{14.4}$$

The total photoproduction positron-proton cross section in this kinematical range is $\sigma_{ep}^{SPP} = 1.3\,\mu b$. The expected number of events from photoproduction background is therefore:

$$N_{SPP} < \sigma_{ep}^{SPP} \cdot A_{SPP} \cdot \mathcal{L}_{eff} = 0.9 \tag{14.5}$$

Of the 20000 Nikolaev-Zakharov events none becomes accepted either, leading to an upper limit due to the diffractive photoproduction events alone of

$$A_{diff} < 5 \cdot 10^{-5}. \tag{14.6}$$

The upper limit of expected events from diffraction alone is (with $\sigma_{ep}^{diff} = 0.39\,\mu b$ from the Monte Carlo)

$$N_{diff} < \sigma_{ep}^{diff} \cdot A_{diff} \cdot \mathcal{L}_{eff} = 0.8, \tag{14.7}$$

which agrees with the result from HERWIG.

As a check on the rejection power of the cuts, the cuts on the hit position of the BPC and the vetoes from the luminosity detector are lifted. A single event survives in the HERWIG sample, depositing $11.1\,GeV$ in the BPC, and 14.52 in the electron tagger of the luminosity monitor. The hit position on the BPC is $(x, y) = (57.6\,mm, -2.35\,mm)$. Both the position cuts and the luminosity detector vetoes safely reject this event. In the Nikolaev-Zakharov sample no events survive the loosend cuts.
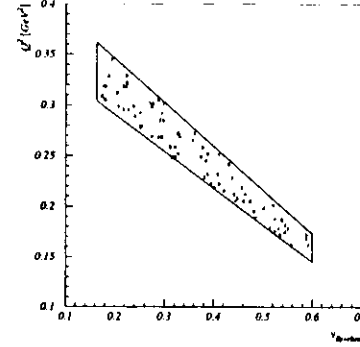
Figure 14.1: Area in Q^2, y_{Bj} plane occupied by the final event sample
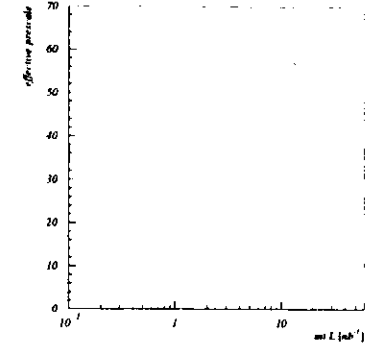
Figure 14.2: Effective prescale factors versus integrated luminosity for the events accepted by TLT bit SPP 11 bit. The values at a prescale factor of 16 are independent of the luminosity since the TLT did not prescale for those runs.

14.3 Flux factors

Knowing the flux $\mathcal{F}$ of photons of a given virtuality Q^2 being emitted from a positron, it is possible to calculate the photon-proton cross section from the cross section for electroproduction. Equation (2.38) relates the cross section for electron-proton collisions to the cross sections of longitudinally and transversely polarized photons with protons. To obtain the total cross section for photon-proton reactions $\sigma_{\gamma^* p} = \sigma_{\gamma^* p}^T + \sigma_{\gamma^* p}^L$, one has to make an assumption about the contribution of the longitudinally polarized photons, which may be significant. The relation between $\sigma_{\gamma^* p}^T$ and $\sigma_{\gamma^* p}^L$ is parametrized by equation (2.73). The mass of the vector meson put into the formula here is the mean of the ρ, ω and ϕ vector mesons, according to their abundance in the vector meson dominance model, here taken from the Pythia Monte Carlo generator: $\rho : \omega : \phi = 17.2 : 1.5 : 1$. That results in $m_V = 0.78\,GeV$. For a mean $Q^2 = 0.25\,GeV^2$, $\sigma_{\gamma^* p}^L$ is 41% of $\sigma_{\gamma^* p}^T$, which must not be neglected.

The flux factors $\mathcal{F} = \sigma_{ep}/\sigma_{\gamma^* p}$ for the different Q^2 bins have been determined by numerical integration. The kinematical range occupied by the final event sample can be found in figure 14.1. That area defines the boundaries for the integration.

The dependence of the cross section σ_T on $y = y_{Bjorken}$ has been measured to be weak [42, 85]. $\sigma_{\gamma^* p}$ is assumed to be independent of y. This allows to write equation (2.38) in the following way:

$$\frac{d^2\sigma_{ep}(y, Q^2)}{dy dQ^2} = \frac{\alpha}{\pi} \cdot \frac{1}{Q^2} \left[\left(\frac{1}{y} - 1 \right) \left(\sigma_{\gamma^* p}^T(Q^2) + \sigma_{\gamma^* p}^L(Q^2) \right) + \frac{y}{2}\sigma_{\gamma^* p}^T(Q^2) \right] \tag{14.8}$$

Using equation (2.73) and setting $\xi = 1$, the total cross section can be written as

$$\sigma_{\gamma^* p} = \sigma_{\gamma^* p}^T + \sigma_{\gamma^* p}^L = \left(1 + \frac{Q^2}{m_V^2} \right) \sigma_{\gamma^* p}^T. \tag{14.9}$$

Integration then yields the flux factor $\mathcal{F}$:

$$\mathcal{F} = \frac{\sigma_{ep}}{\sigma_{\gamma^*p}} = \int_{Q^2_{low}}^{Q^2_{high}} \frac{\alpha}{\pi} \cdot \frac{1}{Q^2} \cdot \left[\ln \frac{y_{max}}{y_{min}} - y_{max} + y_{min} + \frac{y^2_{max} - y^2_{min}}{4(1 + \frac{Q^2}{m_p^2})} \right] dQ^2. \tag{14.10}$$

The boundaries of the integration are the minimum and maximum values of Q^2 allowed by the cuts, see equations (13.5) and (13.6). y_{min} and y_{max} are functions of Q^2 and are drawn in figure 14.1. They do not depend on the scattering angle θ at the given precision and can therefore be described by linear functions:

$$y_{max}(Q^2) = \begin{cases} 0.600 & \text{if } Q^2 < 0.173 \\ 0.600 - 2.305 \cdot (Q^2 - 0.173) & \text{if } 0.173 < Q^2 < 0.363 \end{cases} \tag{14.11}$$

$$y_{min}(Q^2) = \begin{cases} 0.600 - 2.756 \cdot (Q^2 - 0.145) & \text{if } 0.145 < Q^2 < 0.303 \\ 0.164 & \text{if } Q^2 > 0.303 \end{cases} \tag{14.12}$$

The result of the integration can be found in the following table 14.1, the flux factor for the whole kinematical range is:

$$\mathcal{F} = 3.82 \cdot 10^{-4}. \tag{14.13}$$

$Q^2\ [GeV^2]$	$\mathcal{F}$	$\mathcal{F}^{-1}$
0.145–0.218	$7.00 \cdot 10^{-5}$	14292.0
0.218–0.290	$1.53 \cdot 10^{-4}$	6534.5
0.290–0.363	$1.59 \cdot 10^{-4}$	6292.8
0.145–0.363	$3.82 \cdot 10^{-4}$	2618.4

Table 14.1: Flux factors for different Q^2 bins

14.4 Total γ^*p cross section

Starting from equation (14.10) the total photon-proton cross section σ_{γ^*p} can be expressed as

$$\sigma_{\gamma^*p} = \sigma^T_{\gamma^*p} + \sigma^L_{\gamma^*p} = \sigma_{ep} \cdot \mathcal{F}^{-1}, \tag{14.14}$$

the flux factor $\mathcal{F}$ as calculated in section 14.3. The ep cross section σ^i_{ep} in the different Q^2 bins i is given by:

$$\sigma^i_{ep} = \frac{N^i \cdot \eta_{bkg}}{A_{clust} \cdot A^i_{Q^2} \cdot \mathcal{L}_{eff} \cdot \eta_{pos} \cdot \eta_{dead}}, \tag{14.15}$$

where

N^i		: number of events in bin i, see table 14.2 on page 105
A_{clust}		: clustering acceptance, see table E.1 in appendix E
$A^i_{Q^2}$		: Q^2 acceptance, see table 13.2 on page 98
$\mathcal{L}_{eff}$	$= 39.2 \pm 0.4\,nb^{-1}$	: effective luminosity, see equation (14.1) on page 101
$\eta_{bkg} = 1 - C_{bkg}$	$= 93.5 \pm 1.7\%$	: background subtraction, see equation (14.3) on page 102
$\eta_{dead} = 1 - t_{dead}$	$= 98.2 \pm 0.1\%$	: deadtime correction, see equation (11.7) on page 76
η_{pos}	$= 63.9 \pm 1.3\%$	: position detector efficiency, see equation (12.3) on page 81

The quoted errors are by statistics only. The clustering acceptance A_{clust} is determined by the hit position of an event. It is taken into account on an event by event basis rather than using the net clustering acceptance of equation (13.3).

The result of the cross section calculation for each bin of Q^2 is given with statistical error in table 14.2. The Q^2 stated is the center of each bin. The quoted clustering acceptance is the average acceptance $\overline{A_{clust}}$ for the events in each Q^2 bin.

bin	Q^2 $[GeV^2]$	events	$\overline{A_{clust}}$ [%]	A_{Q^2} [%]	σ_{ep} $[nb]$	$\mathcal{F}^{-1}$	σ_{γ^*p} $[\mu b]$
1	0.18	27	100.0	9.1 ± 2.3	11.3 ± 3.6	14292	160.8 ± 52.1
2	0.25	32	107.4	4.9 ± 1.2	27.0 ± 8.6	6535	176.3 ± 56.0
3	0.33	22	98.0	6.2 ± 1.4	13.1 ± 4.2	6293	82.6 ± 26.4

Table 14.2: Electron-proton and total γ^*p cross sections

Because of the limited statistical accuracy, the total cross section is calculated by treating the accessible Q^2 range as a single bin. The mean acceptance as given by equation (13.8) is used, $A_{Q^2} = 6.3 \pm 0.9\%$. The average clustering acceptance for these events is $\overline{A_{clust}} = 102.4\%$. This being larger than 100% is due to bin migrations in the strip detector acceptances which are taken into account on an event by event basis.

The electroproduction cross section in the kinematical range R of this analysis shown in figure 14.1 is then

$$\sigma_{ep} = \iint_R \frac{d^2\sigma_{ep}}{dydQ^2} dy\, dQ^2 = 50.4 \pm 9.3\,nb. \tag{14.16}$$

The error quoted is the statistical error only. The mean Q^2 is $\langle Q^2 \rangle = 0.25\,GeV^2$, the mean γ^*p center of mass energy is $W = 183\,GeV$.

The total virtual photon-proton cross section σ_{γ^*p} at $\langle Q^2 \rangle = 0.25\,GeV^2$ is then given by the electroproduction cross section and the flux factor from equation (14.13), $\mathcal{F}^{-1} = 2618$:

$$\sigma^{tot}_{\gamma^*p} = \sigma_{ep} \cdot \mathcal{F}^{-1} = 132 \pm 24\,\mu b. \tag{14.17}$$

14.5 Systematic uncertainties

The main contributions to the systematic errors stem from uncertainties in the calibration of the beampipe calorimeter, the position of the strip detector, the position finding efficiency and the acceptance. The systematic errrors of the luminosity calculation, the background subtraction and the deadtime determination are small.

14.5.1 Systematic error induced by the uncertainty in the energy scale of the BPC

In sections 9.2 and 9.3 the uncertainty of the energy calibration and the longterm stability has been determined to be $\approx 5.5\%$. This is assumed to be a scale factor. To calculate the influence of the energy scale on the cross sections, the energy is rescaled by $\pm5.5\%$ in the event reconstruction and a new shifted $Q^{2\prime}$ of the events is determined.

The procedure to calculate the resulting error on the cross section is the following: the reconstructed energy of each accepted event is changed according to the systematic error in energy of $\pm5.5\%$. All other quantities remain fixed. The cross section calculated by equation (14.16) remains unchanged, but the kinematical variables change: $Q^2 \to Q^{2\prime}$ and $y \to y'$. These changes in Q^2 and y are used to calculate the change of the cross section $\sigma_{ep}(Q^2)$ at the nominal mean $Q^2 = 0.248 GeV^2$ of this analysis. In the following, all quantities computed at the shifted $Q^{2\prime}$ are denoted by a prime.

The flux factor $\mathcal{F}'(Q^{2\prime})$ is recomputed[21] for the kinematical area covered using the shifted $Q^{2\prime}$ and y' and yields the total γ^*p cross section at the shifted Q^2 value $Q^{2\prime}$:

$$\sigma'_{\gamma^*p}(Q^{2\prime}) = \mathcal{F}'^{-1}(Q^{2\prime}) \cdot \sigma'_{ep}(Q^{2\prime}). \qquad (14.18)$$

This cross section is then evolved to the cross section at the old value of Q^2 using equations (2.69) and (2.70) with $\xi = 1$. Here the dependence on W is neglected, which has been measured to be small [42, 85]:

$$\sigma_{\gamma^*p}(Q^2) = \left(\frac{m_V^2}{m_V^2 + Q^2}\right)^2 \left(1 + \frac{\xi Q^2}{m_V^2}\right) \left[\left(\frac{m_V^2}{m_V^2 + Q^{2\prime}}\right)^2 \left(1 + \frac{\xi Q^{2\prime}}{m_V^2}\right)\right]^{-1} \cdot \sigma'_{\gamma^*p}(Q^{2\prime}). \qquad (14.19)$$

This cross section is transformed back into an positron-proton cross section using the flux factor $\mathcal{F}$ from equation (14.13):

$$\begin{aligned}
\sigma_{ep}(Q^2) &= \mathcal{F}(Q^2) \cdot \sigma_{\gamma^*p}(Q^2) \\
&= \mathcal{F}(Q^2) \cdot \left(\frac{m_V^2}{m_V^2 + Q^2}\right) \cdot \left(1 + \frac{Q^{2\prime}}{m_V^2}\right) \cdot \mathcal{F}'^{-1}(Q^{2\prime}) \cdot \sigma'_{ep}(Q^{2\prime}),
\end{aligned} \qquad (14.20)$$

where $\xi = 1$ is assumed and $m_V = 0.784 GeV$, as before.

The difference $\Delta\sigma_{ep}$ between this cross section and the value for σ_{ep} in equation (14.16) is the systematic uncertainty of the cross section.

In the following table the resulting cross sections are listed:

	$Q^{2\prime}$ [GeV^2]	y'	$\mathcal{F}'^{-1}(Q^{2\prime})$	σ_{ep} [nb]	$\Delta\sigma_{ep}$ [nb]
$E' = 0.945 \cdot E$	0.234	0.405	3273.1	62.1	11.6
$E' = 1.055 \cdot E$	0.262	0.336	2035.3	39.8	−10.6

---

[21]Since y changes as well, the functions $y_{min}(Q^2)$ (equation (14.12)) and $y_{max}(Q^2)$ (equation (14.11)) have to be recomputed for the integration.

It might be surprising that an error of 5.5% in the energy results in an error of 23% in the cross section. The reason is the logarithm $\ln(y_{max}/y_{min})$ in the flux factor (see equation (14.10)). y is nonlinear in the beampipe calorimeter energy E'. For a fixed error on the BPC energy, the closer E' is to the beam energy, the bigger the error becomes on y. This is another reason to choose the upper limit on the beampipe calorimeter energy at $23 GeV$.

14.5.2 Systematic error due to position uncertainty

The same strategy as for the energy scale is used. The position accuracy of the beampipe calorimeter survey is $1.5 mm$ in x and y, see section 4.3. The value of Q^2 depends much stronger on x than on y. To account also for the effect of a shift in y the hit position in x of each event is shifted by $\pm2 mm$.

	$Q^{2\prime}$ [GeV^2]	y'	$\mathcal{F}'^{-1}(Q^{2\prime})$	σ_{ep} [nb]	$\Delta\sigma_{ep}$ [nb]
$x = x + 2 mm$	0.262	0.370	2647.8	51.8	1.3
$x = x - 2 mm$	0.235	0.370	2587.7	49.1	−1.3

14.5.3 Systematic error due to position finding efficiency

The position finding efficiency η_{pos} in section 12.2 uses the clustering efficiency as determined in the testbeam and the relative efficiencies of the x and y plane as determined from data. Cuts on the number of strips allowed in a cluster are imposed, guided by shower size considerations.

Varying the cuts on the strip multiplicities in the cluster allows to estimate the systematic errors of the position finding efficiency. If the cut on the strip multiplicity is tightened or relaxed, the position finding efficiency will change. The cross section calculation is repeated with the changed cuts and efficiencies and should ideally yield the same result.

First it is checked that the relative efficiency of the two position detector planes is independent of the cuts on the strip multiplicities.

The result of the cross section calculation with different numbers of strips allowed in the cluster is:

Multiplicity	η_{pos}	σ_{ep} [nb]	$\Delta\sigma_{ep}$ [nb]
3	0.50±0.02	38.2	−12.3
4	0.64±0.01	50.4	0.0
5	0.75±0.01	54.2	3.7

14.5.4 Systematic error due to uncertainties in the acceptance calculation

The acceptance calculation has been cross checked in section 13.4. By comparing equations 13.8 and 13.16 the error in the acceptance calculation is

$$\Delta\mathcal{A} = \mathcal{A}_{Q^2} - \mathcal{A}' = -0.59\%. \qquad (14.21)$$

The relative error in the cross section is therefore 9%, leading to $\Delta\sigma_{ep} = \pm4.7 nb$.

14.5.5 Radiative corrections

The effect of radiative corrections is determined by using the Monte Carlo program DJANGO and is discussed in section 12.12. The shift in Q^2 is determined on the generator level by events where a photon has been radiated in the initial state compared to such events where there was radiation in the final state or no radiation.

12% of the events surviving the selection cuts have initial state radiation that leads to shifting Q^2 by 1.8% towards smaller values, compared to events where no initial state radiation is present. Approximating

$$\sigma_{ep}(Q^2) \approx \frac{Q^{2'}}{Q^2} \cdot \sigma_{ep}(Q^{2'}), \tag{14.22}$$

leads to a cross section 1.8% smaller.

14.5.6 Other systematic uncertainties

The uncertainty in the background subtraction can be neglected. Only the relative bunch currents enter in the computation of the weights, equation (14.2). Any systematic error in the current measurement would cancel out.

Errors in the deadtime calculation have a small effect. Even doubling the deadtime to 3.6% would change the cross section by 1.9%.

The systematic error on the luminosity determination is stated [66] to be 1%.

The clustering acceptance uncertainty is estimated by comparing the net clustering acceptance of 106.0% as given by equation (13.3) and the average clustering acceptance $\overline{A_{clust}} = 102.4\%$ of the final event sample. The difference is attributed to the systematic error. This changes the cross section by 3.5%.

Adding these uncertainties in quadrature, a systematic error of 4% results.

14.6 Final result with total systematic error and radiative corrections

To obtain the total error, the positive and the negative contributions of the uncertainties are added in quadrature. Correcting the cross section for the radiative corrections as well, leads to a positron-proton cross section in the kinematic range of this analysis (see figure 14.1) of

$$\sigma_{ep} = 49.5 \pm 9.1(\text{stat}) \, {}^{+13.3}_{-17.1} \, (\text{syst}) \, nb, \tag{14.23}$$

for the cuts applied.

The mean of the events leads to $Q^2 = 0.25\,GeV^2$ and the $\gamma^* p$ center of mass energy is $W = 183\,GeV$. Using equation (14.10) this can be translated into the photon-proton cross section at a $\langle Q^2 \rangle = 0.25\,GeV^2$:

$$\sigma_{\gamma^* p}(Q^2 = 0.25\,GeV) = 130 \pm 24(\text{stat}) \, {}^{+35}_{-45} \, (\text{syst}) \, \mu b. \tag{14.24}$$

Assuming a Q^2 dependence of the cross section according to equations 2.69 and 2.70 with $\xi = 1$, this value can be extrapolated to the total cross section for photoproduction at $Q^2 = 0$:

$$\sigma_{\gamma p}(Q^2 = 0) = \left(1 + \frac{Q^2}{M_V^2}\right) \cdot \sigma_{\gamma^* p}(Q^2) = 183 \pm 34(\text{stat}) \, {}^{+49}_{-63} \, (\text{syst}) \, \mu b, \tag{14.25}$$

where $M_V = 784\,MeV$ is used.

This has to be compared to the recent measurements in photoproduction at HERA:

$\sigma_{\gamma p}$ μb	W GeV	reference
165±2±11	200	[42]
143±4±17	180	[85]
185±5±16	180	[57]

Table 14.3: Comparison of the photon proton cross sections measured in photoproduction at $Q^2 = 0$ at HERA. The first error quoted is due to statistics, the second one is due to systematics.

In figure 14.4 the total cross section $\sigma_{tot}^{\gamma^* p} = \sigma_T + \sigma_L$ for the scattering of virtual photons off protons is plotted for different values of Q^2 versus W^2 for comparison. The cross section $\sigma_{tot}^{\gamma^* p}(Q^2 = 0.25\,GeV^2)$ of this analysis, equation (14.24), is plotted as a star at $Q^2 = 0.25\,GeV^2$. The first two values from table 14.3 of the total photoproduction cross section at $Q^2 = 0$ are also plotted as solid circles. The solid line is the parametrization of equation (2.54), taken from [29].

14.7 Determination of F_2

Using the definition of the longitudinal structure function F_L in equation (2.35) the ep cross section (2.26) can be written as

$$\frac{d^2\sigma_{ep}(y, q^2)}{dy dQ^2} = \frac{4\pi\alpha^2}{Q^4} \frac{1}{2} \left[\frac{1}{y}(1 + (1-y)^2)F_2(x) - yF_L\right]. \tag{14.26}$$

Integrating both sides over y yields

$$\frac{d\sigma_{ep}(y)}{dQ^2} = \frac{4\pi\alpha^2}{Q^4} \left[\left(\ln\frac{y_{max}}{y_{min}} - y_{max} + y_{min} + \frac{y_{max}^2}{4} - \frac{y_{min}^2}{4}\right) F_2 + \left(\frac{y_{min}^2}{4} - \frac{y_{max}^2}{4}\right) F_L\right] \tag{14.27}$$

Equation (14.27) can now be integrated on both sides along the procedure described in section 14.3 over the kinematical area covered in this analysis. The value of F_L has to be choosen, since no measurement is available in this kinematical range. Being guided by the vector dominance model, equation (2.73), and the definition of the longitudinal structure function by (2.34) it is assumed that

$$F_L = 0.4 \cdot F_2. \tag{14.28}$$

The result for F_2 is

$$F_2 = 0.30 \pm 0.06(\text{stat}) \, {}^{+0.08}_{-0.10} \, {}^{+0.02}_{-0.01} \, (\text{syst}), \tag{14.29}$$
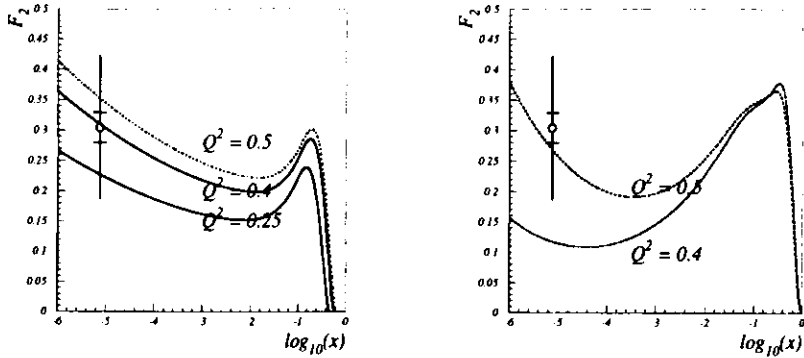
Figure 14.3: F_2 determined from the BPC data at $Q^2 = 0.25 GeV^2$ and $x = 7.4 \cdot 10^{-6}$. The smaller error is the error due to the uncertainty in F_L. For this, F_L has been varied between 0 and 100% of F_2. The bigger error is this error plus the total systematic and statistical error of this analysis added in quadrature. In the left plot, the parametrization of F_2 given by Donnachie and Landshoff [30] is plotted for values of $Q^2 = 0.25, 0.4,$ and $0.5 GeV^2$. In the right figure, the parametrization from Glück, Reya and Vogt [37](1995) is shown for $Q^2 = 0.4, 0.5 GeV^2$. At these values of Q^2 the parametrization has to be taken with caution, see text in section 14.7.

at a mean $\langle Q^2 \rangle = 0.25 GeV^2$ ($Q^2 = 0.15 \ldots 0.36 GeV^2$) and $\langle x \rangle = 7.4 \cdot 10^{-6}$ ($x = 3.05 \cdot 10^{-6} \ldots 24.5 \cdot 10^{-6}$). The first systematic error is due to the systematic error on the cross section, the second one due to the assumed uncertainty of F_L. It is derived by varying $F_L = 0 \ldots 100\% \cdot F_2$ in the integration procedure.

In figure 14.3 this value is plotted together with a parametrization for F_2 from Donnachie and Landshoff [30], see equation (2.58), and with the parametrization from Glück, Reya and Vogt (GRV) taken from [37](1995). The smaller error bars indicate the error due to the uncertainty of F_L. To get this error, the magnitude of F_L has been varied between 0 and 100% of F_2 in the integration procedure described above. F_2 is then in the range between 0.29–0.33. The larger error is the total systematic and statistical error of this analysis added in quadrature to the error due to the uncertainty of F_L.

The parametrization from Donnachie and Landshoff is based on Regge theory (see section 2.2) and works well at small values of Q^2. The GRV parametrization can, strictly speaking, not be applied at the Q^2 values of this experiment. At these small values of Q^2 the parametrization is dominated by the valence-like input structure functions, which can be seen by the 'bump' showing up at large x. Citing from their 1995 paper [37], the "parametrizations are then valid for $0.4 \lesssim Q^2 \lesssim 10^6 GeV^2$ [...] and $10^{-5} \lesssim x < 1$." They also state that one has to allow their evolution procedure to get away from the input structure functions. "Therefore, only well above the valence-like input scale μ, $Q^2 \gtrsim 0.5 - 0.6 GeV^2$ say, will our dynamical perturbative predictions become reliable and experimentally relevant."
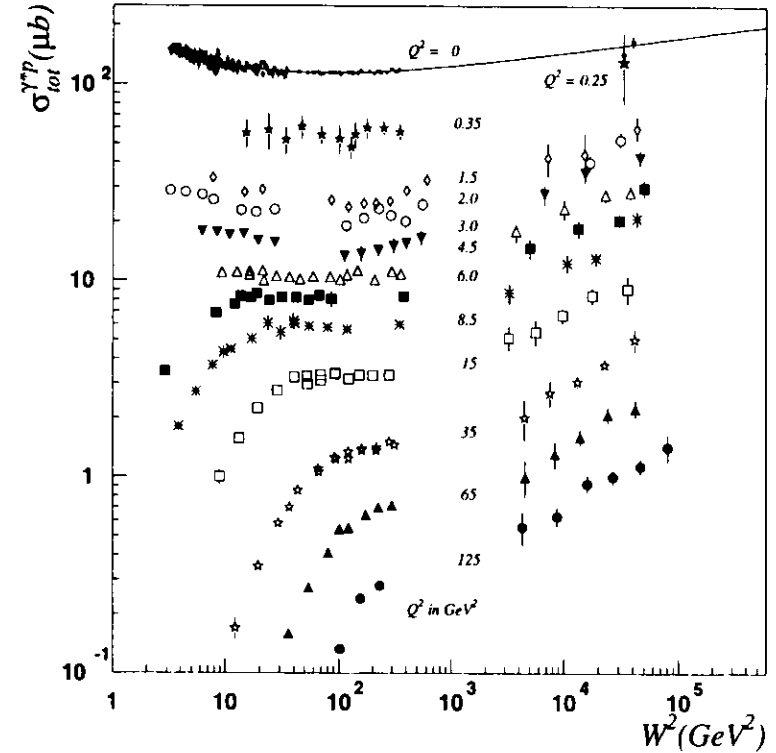
Figure 14.4: Total cross section for scattering of virtual photons off protons at different values of Q^2 plotted versus center of mass energy W^2 of the photon-proton system; adapted from [82]. The solid curve is the parametrization (2.54) for photoproduction at $Q^2 = 0$ from [29]. Photoproduction data is plotted as solid circles, the result of this analysis is shown as a star. The photoproduction points around $W^2 = 3.5 \cdot 10^4 GeV^2$ are taken from [42] and [85].

15 Conclusion

The feasibility of measuring inelastic positron-proton scattering at angles of $\approx 23\,mrad$ with a small tungsten calorimeter with Si-diode readout has been demonstrated. Main difficulties with working very close to the circulating positron and proton beams were lack of space and a large radiation background. During the 1994 measurements a total dose of several $1000\,Gy$ was accumulated at a distance of $5\,cm$ from the beams, which required exchanging part of the detector during that period. Careful monitoring of this background together with machine operations is required in this type of experiments.

As a result, the $e^+ p$ cross section has been measured at a mean Q^2 of $\langle Q^2 \rangle = 0.25\,GeV^2$ and a photon-proton center of mass energy of $\langle W \rangle = 183\,GeV$. This cross section can be translated into a virtual photon-proton cross section. One obtains

$$\sigma_{tot}(\gamma^* p) = \sigma_T(\gamma^* p) + \sigma_L(\gamma^* p) = 130 \pm 24(\text{stat}) \,^{+35}_{-45}\,(\text{syst})\,\mu b.$$

Extrapolated to $Q^2 = 0$ with the help of the vector dominance model one gets

$$\sigma_{tot}(\gamma p) = 183 \pm 34(\text{stat}) \,^{+49}_{-63}\,(\text{syst})\,\mu b.$$

These values fit well an interpolation of measurements made at $Q^2 = 0$ and at larger values of Q^2, and provide a first glimpse at the region between photoproduction and deep inelastic scattering. The errors are dominated by systematics, the biggest contribution coming from the energy calibration and the hit detection efficiency.

The proton structure function F_2, determined from these measurements at $\langle Q^2 \rangle = 0.25\,GeV^2$, $\langle x_{Bj} \rangle = 7.4 \cdot 10^{-6}$ is

$$F_2 = 0.30 \pm 0.06(\text{stat}) \,^{+0.08}_{-0.10}\,(\text{syst}) \,^{+0.02}_{-0.01}\,,$$

where the last error comes from the uncertainty in the longitudinal structure function F_L.

This value can be compared with an approach by Donnachie and Landshoff [30], which is based on Regge theory, and which was used to fit low energy data of the NMC collaboration. Extrapolation of this fit to HERA energies predicts F_2 at our values of Q^2 and x_{Bj}. One of the topical questions is, whether the Pomeron seen in very high energy experiments at HERA and the $p\bar{p}$ colliders is identical with the 'soft' Pomeron introduced a long time ago, or, whether a Pomeron with additional ('hard') properties is needed. Donnachie and Landshoff remark that "if the HERA experiments find results for νW_2 significantly larger at small x than our extrapolations, we claim that this will be a clear signal that they have discovered new physics." The experimental value found for $F_2 = \nu W_2$ is larger than their extrapolation, but the error is still too large to allow conclusions.

A Channel assignment

The assignment of the strips of the position detector to the readout channels can be seen from figure A.1.
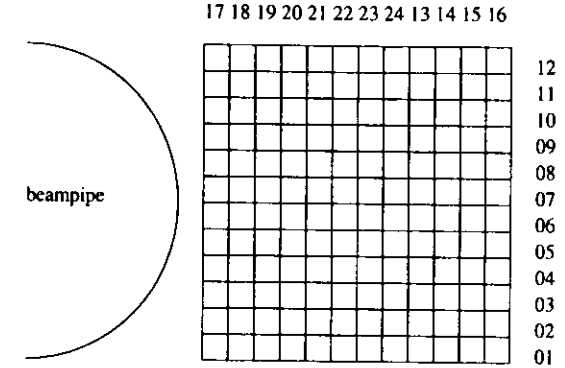
Figure A.1: Channel assignment of the position detector strips (as seen from the interaction region)

The calorimeter channel assignment is as follows. The numbering of the segments is the same as in section 5.1.1.

Analog-Sum:	Channel 31
Segment Ia:	Channel 30
Segment Ib:	Channel 27
Segment Ic:	Channel 29
Segment Id:	Channel 28
Segment II:	Channel 26
Segment III:	Channel 25

Table A.1: Calorimeter channel assignment

B Calibration constants of the strip detector during 1994 datataking

Strip number	Offset [ADC chs]	Slope [ADC chs/fC]	Position of strip centers in ZEUS coordinates x-strip [mm]	y-strip [mm]	Comment
1	-382.3	37.22		19.02	
2	-416.6	34.68		15.02	
3	-388.5	29.93		11.02	
4	-438.5	33.28		7.02	
5	-339.3	29.01		3.02	
6	-352.0	29.18		-0.98	
7	-499.1	35.76		-4.98	strip not connected
8	-397.9	32.03		-8.98	
9	-273.1	25.87		-12.98	
10	-15.0	0.21		-16.98	defunct amplifier
11	-412.7	30.75		-20.98	
12	-286.5	26.50		-24.98	
13	-150.5	29.85	91.48		noisy amplifier[a]
14	-189.0	30.18	95.48		noisy amplifier
15	-129.8	23.92	99.48		noisy amplifier
16	-131.4	24.01	103.48		noisy amplifier
17	-309.5	24.63	59.48		
18	-583.2	39.52	63.48		
19	-426.8	30.26	67.48		
20	-424.3	29.81	71.48		
21	-313.4	24.67	75.49		
22	-447.9	31.03	79.48		
23	-386.4	28.55	83.48		
24	-556.5	39.38	87.48		

Table B.1: Calibration constants of the strip detector during 1994 datataking

[a]Strips 13–16 used preamplifiers differently mounted than the rest.

C Configuration of BPC trigger slots in the GFLT

The following tables are excerpts from the ZEUS GFLT homepage [62] in the Worldwide Web.

In table C.1 the different configurations of the GFLT trigger slots pertaining to the BPC are listed. The definitions of the names can be found in table C.2. That table is organized following the trigger ID (last three digits). For the definition, C notation is used: '||' is a logical OR, '&&' is a logical AND. The '$n' is the nth variable in the argument list of the name.

slot 31:

Run			Id	Name	Prescale
9385	–	9627	909031558	BPCtiming14*vv	512
		9628	909031594	BPCtiming14*vvv	512
9631	–	9689	909031558	BPCtiming14*vv	512
9693	–	10149	909031594	BPCtiming14*vvv	512
		10150	909031594	BPCtiming14*vvv	0
10154	-	10263	909031594	BPCtiming14*vvv	512

slot 32:

Run			Id	Name	Prescale
9466	–	9627	909032583	BPCt*CALetc*vv(13,464,1250,1250,464)	4
		9628	909032595	BPCt*CALetcgTRK*vvv(13,464,1250,1250,464)	4
9631	–	9689	909032583	BPCt*CALetc*vv(13,464,1250,1250,464)	4
9693	–	10149	909032595	BPCt*CALetcgTRK*vvv(13,464,1250,1250,464)	4
		10150	909032595	BPCt*CALetcgTRK*vvv(13,464,1250,1250,464)	0
		10154	909032595	BPCt*CALetcgTRK*vvv(13,464,1250,1250,464)	4

slot 34:

Run			Id	Name	Prescale
9466	–	9627	909034560	BPCt*CAL_E*aTRK*vv(13,4972)	1
		9628	909034596	BPCt*CAL_E*gTRK*vvv(13,4972)	1
9631	–	9689	909034560	BPCt*CAL_E*aTRK*vv(13,4972)	1
9693	–	10149	909034596	BPCt*CAL_E*gTRK*vvv(13,4972)	1
		10150	909034596	BPCt*CAL_E*gTRK*vvv(13,4972)	0
		10154	909034596	BPCt*CAL_E*gTRK*vvv(13,4972)	1

Table C.1: List of BPC triggers slots at the GFLT for the 1994 runs in this analysis

BPCtiming14*vv

  id: 558

logic: 1

veto: C5v, VWiv, SRTDv, BPCemptyv

BPCt*CAL_E*aTRK*vv

  id: 560

logic: BEAMLINE_good_timing < \$1 && (CAL_E $\geq$ \$2) && _TRK_multiplicity $\geq$ 1

veto: C5v, VWiv, BPCemptyv, SRTDv

BPCt*CALetc*vv

  id: 583

logic: BEAMLINE_good_timing < \$1 && ((RCAL_EMC_E $\geq$ \$2 || RCAL_E_th $\geq$ \$3 || FCALth_LUMI $\geq$ \$4) || ((CAL_E $\geq$ \$5) && _TRK_multiplicity $\geq$ 1))

veto: C5v, VWiv, BPCemptyv, SRTDv

BPCtiming14*vvv

  id: 594

logic: 1

veto: C5v, VWiv, BPCemptyv, VWov, SRTDv

BPCt*CALetcgTRK*vvv

  id: 595

logic: BEAMLINE_good_timing < \$1 && ((RCAL_EMC_E $\geq$ \$2 || RCAL_E_th $\geq$ \$3 || FCALth_LUMI $\geq$ \$4) || ((CAL_E $\geq$ \$5) && (TRK_quality == 2 || TRK_quality == 3)))

veto: C5v, VWiv, BPCemptyv, VWov, SRTDv

BPCt*CAL_E*gTRK*vvv

  id: 596

logic: BEAMLINE_good_timing < \$1 && (CAL_E $\geq$ \$2) && (TRK_quality == 2 || TRK_quality == 3)

veto: C5v, VWiv, BPCemptyv, VWov, SRTDv

Table C.2: Trigger slot definitions of the BPC trigger at the ZEUS Global First Level Trigger

D   Weights of the samples from different physics generators

process	events	weight
non-diffractive	2501	1.267
elastic	809	0.796
γ dissociation	657	0.693
proton dissociation	648	0.703
double dissociation	336	0.678

Table D.1: Weight factors of the Monte Carlo events used in the acceptance calculation for σ_{tot}

E   Strip detector acceptances from the clustering Monte Carlo

The beampipe calorimeter acceptances in (x, y) are given by the effect of dead strips of the strip detector folded with the clustering position recontruction. The Monte Carlo used for this calculation is described in section 10.3. The result for the acceptances $\mathcal{A}_{clust}$ on a $4 \times 4\,mm^2$ grid is listed in the following table. The grid positions are the centers of the strips of the position detector.

y	x
	59.4	63.4	67.4	71.4	75.4	79.4	83.4	87.4	91.4	95.4	99.4	103.4
18.9	278.9	175.4	156.9	145.6	147.1	149.8	155.1	150.6	153.5	157.4	169.2	287.8
14.9	191.2	116.9	102.0	105.6	103.7	105.2	104.6	105.0	103.5	102.4	116.7	160.6
10.9	169.4	105.2	93.7	92.0	95.6	91.9	93.0	94.2	93.0	95.6	107.1	149.4
6.9	164.5	105.4	93.4	92.9	92.3	92.6	93.8	91.3	92.8	91.3	100.0	152.4
2.9	157.8	92.5	80.7	81.8	81.3	83.3	82.8	81.2	79.2	81.1	95.1	131.3
-1.1	221.1	130.3	116.8	116.3	118.2	115.3	120.1	117.4	119.8	121.7	132.9	191.4
-5.1	69.3	45.3	38.0	37.9	37.3	39.4	36.8	41.5	41.4	40.3	42.7	60.8
-9.1	202.5	120.8	106.5	102.8	106.9	108.3	106.1	104.0	106.9	103.9	120.1	168.8
-13.1	197.8	121.9	105.5	102.7	106.5	102.1	109.7	104.1	108.2	110.0	125.4	186.4
-17.1	71.9	38.7	38.3	40.8	36.6	40.0	39.1	37.0	35.2	38.2	40.6	57.1
-21.1	264.8	157.4	148.7	144.1	144.4	145.2	145.5	150.0	140.1	150.0	167.2	234.5
-25.1	222.8	142.7	126.7	130.5	125.0	125.7	126.0	124.2	145.1	120.6	145.4	210.2

Table E.1: Clustering acceptances $\mathcal{A}_{clust}$ in (x, y) bins given in per cent as determined from the clustering Monte Carlo described in section 10.3. The quoted position is the center of the bin in ZEUS coordinates.

References

[1] H. Abramowicz, E. Levin, A. Levy, U. Maor
A parametrization of $\sigma_T(\gamma^* p)$ above the resonance region for $Q^2 \geq 0$
Phys. Lett. **B269** (1991) 465–476

[2] N. Achasov, V. Karnakov
Production of hadrons by a longitudinal photon (small q^2)
Sov. J. Nucl. Phys **38** (1983) 736–741

[3] G. Akopdjanov et al.
Determination of Photon Coordinates in a Hodoscope Cherenkov Spectrometer
Nuclear Instruments and Methods, **140** (1977) 441–445

[4] G. Altarelli, G. Parisi
Asymptotic Freedom in Parton Language
Nucl. Phys. **B126** (1977) 298–318

[5] A. Andresen et al.
Construction and Beamtest of the ZEUS Forward and Rear Calorimeter
Nuclear Instruments and Methods in Physics Research, **A309** (1991) 101–142

[6] V. Barger
Reaction Mechanisms at High Energy
in *Proceedings of the XVII International Conference on High Energy Physics* (ed. J. Smith), London 1974
published by Rutherford Laboratory

[7] K.-H. Barth
Messungen zur Homogenität des ZEUS Hadron-Elektron-Separators
Diplomarbeit am Fachbereich Physik der Universität Hamburg, 1991

[8] T. Bauer, R. Spital, D. Yennie, F. Pipkin
The hadronic properties of the photon in high-energy interactions
Rev. Mod. Phys. **50** (1978) 261–436

[9] I. Baur
Ein Strahlrohrkalorimeter für das ZEUS-Experiment
Diplomarbeit am Fachbereich Physik der Universität Hamburg, August 1992

[10] U. Behrens, L. Hagge, F. Lohmann, E. Tscheslog, T. Schlichting, W. Vogel
Interfacing Component Subsystems with the Eventbuilder
ZEUS-Note 91-071

[11] U. Behrens, E. Tscheslog, W. Vogel
Data Flow from the Components to the Event Builder
ZEUS-Note 90-127

[12] E. Borchi, et al.
Systematic investigations of the local hardening effect and lateral electromagnetic-shower development
CERN-PPE/91-34

[13] H. Boterenbrood
User Software Documentation 2TP-VME module (MK4)
NIKHEF-H, Amsterdam 1990

[14] C. Bourrely, J. Soffer, T. Wu
Expanding protons seen by HERA
Phys. Lett. **B339** (1994) 322–324

[15] R. Brun et al.
GEANT 3.13
CERN DD/EE/84-1 (1987)

[16] L. Bugge
On the Determination of Shower Central Positions from Lateral Samplings
Nuclear Instruments and Methods in Physics Research, **A242** (1986) 228-236

[17] B. Burow
*A Measurement of the Total Photon-Proton Cross Section in the Center of Mass Energy Range
167 to 194 GeV*
Ph.D. Thesis (University of Toronto), 1993
DESY F35D-94-01

[18] Y. Bushnin et al.
The Measurement of the Spatial Coordinates of High Energy Photons with a Scintillation Hodoscope Spectrometer
Nuclear Instruments and Methods, **106** (1973) 493-498

[19] C. Callan, D. Gross
High Energy Electroproduction and the Constitution of the Electric Current
Phys. Rev. Lett. **22** (1969) 156–159

[20] *Parallel C User Manual*
Caplin Cybernetics, ZDV-C-USM-4

[21] CDF-collaboration: F. Abe et al.
Measurement of the antiproton-proton total cross section at $\sqrt{s} = 546\,GeV$ and $1800\,GeV$
Phys. Rev. **D50** (1994) 5550–5561

[22] K. Charchula, J. Gajewski
Numerical Study of Radiative Corrections in the Low Q^2 Region at HERA
DESY 92-173

[23] K. Charcula, G. A. Schuler, H. Spiesberger
*Combined QED And QCD Radiative Effects in Deep Inelastic Lepton-Proton Scattering: the
Monte Carlo Generator DJANGO6*
Comp.Phys.Commun. **81** (1994) 381-402

[24] G. Chew, S. Frautschi
Principle of Equivalence for all strongly interacting particles within the S-Matrix framework
Phys. Rev. Lett. **7** (1961) 394–397

[25] P. Collins
An Introduction to Regge Theory and High Energy Physics
Cambridge University Press, Cambridge, 1977

[26] M. Derrick et al.
Design and Construction of the ZEUS Barrel Calorimeter
Nuclear Instruments and Methods in Physics Research, **A309** (1991) 77-100

[27] Y. Dokshitzer
Calculation of Structure Functions of Deep-Inelastic Scattering and e^+e^- Annihilation by Perturbation theory in Quantum Chromodynamics
Sov. Phys. JETP. **46** (1977) 641–653

[28] A. Donnachie and P. Landshoff
Elastic Scattering and Diffractive Dissociation
Nucl. Phys. **B244** (1984) 322–336
P. Landshoff
Nonperturbative effects at small x
Nucl. Phys. B(Proc. Suppl.)**18C** (1991) 211–219

[29] A. Donnachie and P. Landshoff
Total cross sections
Phys. Lett. **B296** (1992) 227–232

[30] A. Donnachie and P. Landshoff
Proton structure function at small Q^2
Z. Phys. **C61** (1994) 139–145

[31] M. Drees and K. Grassie
*Parametrizations of the photon structure and applications to supersymmetric particle production
at HERA*
Z. Physik **C28** (1985) 451–462

[32] B. Foster
Tracking Summary
Talk given during ZEUS Meeting at DESY on 2.11.1994

[33] J. Fraser
private communication

[34] M. Froissart
Asymptotic Behaviour and Subtractions in the Mandelstam Representation
Phys. Rev. **123** (1961) 1053-1057

[35] M. Gell-Mann, F. Zachariasen
Form Factors and Vector Mesons
Phys. Rev. **124** (1961) 953–964

[36] M. Genovese, N. Nikolaev, B. Zakharov
Direct calculation of the triple pomeron coupling for diffractive DIS and real photoproduction
KFA-IKP-TH-1994-36, Oct 1994.

[37] M. Glück, E. Reya, A. Vogt
Radiatively generated parton distributions for high energy collisions
Z. Phys. **C48** (1990) 471-482
Parton distributions for high energy collisions
Z. Phys. **C53** (1992) 127-134
*Comparing radiatively generated parton distributions with recent measurements of $F_2(x, Q^2)$ in
the small-x region*
Phys. Lett **B306** (1993) 391-394
Dynamical parton distributions of the proton and small-x physics
Z. Phys **C67** (1995) 433-447

[38] S. Goble, G. Kieft, A. de Waard
Short Hardware Description of the 2TP_VME Module
NIKHEF, Electronic Department, Amsterdam 1990

[39] V. Gribov, L. Lipatov
Deep inelastic ep scattering in perturbation theory
Sov. J. Nucl. Phys. **15** (1972) 438–450
e^+e^--*pair annihilation and deep inelastic ep scattering in perturbation theory*
Sov. J. Nucl. Phys. **15** (1972) 675–684

[40] J. Große-Knetter
Messungen mit dem Strahlrohrkalorimeter am ZEUS-Detektor
Diplomarbeit am Fachbereich Physik der Universität Hamburg, Mai 1994

[41] H1-Collaboration: T. Ahmed et al.
A Measurement of the Proton Structure Function $F_2(X,Q^2)$
Nucl. Phys. **B439** (1995) 471–502

[42] H1-Collaboration: S. Aid et al.
Measurement of the Total Photon Proton Cross Section and its Decomposition at 200GeV Center of Mass Energy
DESY 95-162

[43] H1-Collaboration and ZEUS-Collaboration: Julian P. Phillips, et al.
Rapidity Gap Events at HERA and the Structure of the Pomeron
Invited talk at Workshop on Deep Inelastic Scattering and QCD (DIS 95), Paris, France, 24-28 Apr 1995
DESY-95-152 (C)

[44] G. Hartner
private communication

[45] G. Hartner, Y. Iga, J. Lane, N. McCubbin
VCTRAK (3.06/11): Offline Output Information
ZEUS-Note 95-004

[46] G. Ingelman
LEPTO version 6.1 — The Lund Monte Carlo for Deep Inelastic Lepton-Nucleon Scattering
in *Proceedings of the Workshop Physics at HERA* (ed. W. Buchmüller and G. Ingelman)
DESY (1991), Vol. 3, pp. 1366–1394

[47] INMOS Limited
Transputer Reference Manual
Prentice Hall, 1988

[48] A. Kwiatkowski, H.-J. Möhring and H. Spiesberger
HERACLES: an event generator for ep interactions at HERA energies including radiative processes
Comp. Phys. Commun. **69** (1992) 155–172

[49] A. Kwiatkowski, H. Spiesberger, H.-J. Möhring
Characteristics of radiative events in deep inelastic ep scattering at HERA
Z. Phys. **C50** (1991) 165–178

[50] M. Lancaster
talk presented at Durham, Sept. 1995
proceedings to be published in Physics Journal G

[51] Landolt-Börnstein
Total Cross Sections for Reactions of High Energy Particles
New Series, Vol. 12b, H. Schopper, Ed.(1987)

[52] A. Levy
The Energy behaviour of Real and Virtual Photon-Proton Cross Sections
DESY 95-003

[53] E. Lohrmann
Measurement of Electron-Proton elastic Scattering with the ZEUS Detector
ZEUS-Note 87-53

[54] E. Lohrmann
Hochenergiephysik
Teubner Studienbücher: Physik, 1986

[55] M. Löwe
The Hard- and Software of the Beampipe Calorimeter
ZEUS-Note 94-32

[56] M. Löwe
Radiation Dose Measurement in the Vicinity of the Beampipe Calorimeter
ZEUS-Notes 95-11 and 94-77

[57] J. Mainusch
Measurement of the Total Photon-Proton Cross-Section at HERA Energies
Ph.D. thesis, University of Hamburg, 1995

[58] G. Marchesini et al.
HERWIG 5.1 — a Monte Carlo event generator for simulating emission reactions with interfering gluons
Comp. Phys. Commun. **67** (1992) 465–508

[59] A. Martin
Extension of the axiomatic analyticity domain of scattering amplitudes by unitarity - I
Il Nuovo Cimento **42A** (1966) 930–953
Extension of the axiomatic analyticity domain of scattering amplitudes by unitarity - II
Il Nuovo Cimento **44A** (1966) 1219–1244

[60] M. Momayezi
Characteristics and Tolerance to Radiation of the Silicon Detectors used in the Hadron-Electron Separator of ZEUS
DESY F35D-92-05

[61] E. Morré
Ein Untergrundmonitor für das ZEUS-Experiment
Diplomarbeit am Fachbereich Physik der Universität Hamburg, 1992

[62] M. Nakao
GFLT homepage
http://zow00.desy.de:8000/ZEUS_ONLY/GFLT/gflt.html

[63] I. Park
Control Flow for Tasks on ZEUS CDAQ
ZEUS-note 90-065

[64] Particle Data Group
Review of Particle Properties
Phys. Rev. **D45** (1992) 1–584

[65] K. Piotrzkowski
private communication

[66] K. Piotrzkowski, M. Zachara
Determination of the ZEUS Luminosity in 1994
ZEUS-Note 95-138

[67] T. Regge
Introduction to Complex Orbital Momenta
IL Nuovo Cimento **14** (1959) 951–976
Bound States, Shadow States and Mandelstam Representation
Il Nuovo Cimento **18** (1960) 947–956

[68] R. Roberts
The structure of the proton
Cambridge University Press, Cambridge, 1990

[69] J. Sakurai
Theory of Strong Interactions
Ann. Phys. **11** (1960) 1–48

[70] G. Schuler, T. Sjöstrand
Towards a Complete Description of High-Energy Photoproduction
Nucl. Phys. **B407** (1993) 539–605

[71] G. Schuler, J. Terron
Photon-Proton Total Cross Section and the Reaction $\gamma p \to \rho$
CERN TH-6415-92, Feb. 1992

[72] O. Schwarzer
Improved determination of $y_{Jacquet-Blondel}$
ZEUS-Note 94-138

[73] W. Shambroom et al.
Diffractive production of vector mesons in muon-proton scattering at 150 and 100GeV
Phys. Rev. **D26** (1982) 1–26

[74] T. Sjøstrand
High-energy physics event generation with Pythia 5.7 and JETSET 7.4
Comp. Phys. Commun. **82** (1994) 74-90
Pythia 5.7 and JETSET 7.4 physics and manual
CERN-TH-7112-93, Feb. 1994

[75] W. Smith, M. Jaworski, J. Lackey, P. Robl
ZEUS Calorimeter First Level Trigger
ZEUS-Note 89-085

[76] W. Smith, K. Tokushuku, L. Wiggers
The ZEUS Trigger System
Proceedings of Computing in high energy physics '92, pp. 222-225
Annecy 1992, and DESY report 92-150

[77] K. Tokushuku
GFLT Design Document I -interface to component-
ZEUS Note 88-098

[78] UA8-Collaboration: A. Brandt et al.
Evidence for a super-hard pomeron structure
Phys. Lett. **B297**(1992) 417–424

[79] R. van Staa, H. Riege
ZEUS Beamline Calorimeter Local First Level Trigger Interface LFLT
Universität Hamburg, II. Institut f. Experimentalphysik TEB, 1993

[80] D. Westphal
Polarisationsmessungen am HERA Elektronenstrahl
DESY F35D-93-04 (1993)

[81] ZEUS-Collaboration: M. Derrick et al.
Measurement of the Proton Structure Function F_2 from the 1993 HERA Data
Z. Phys. **C65** (1995) 379–398

[82] ZEUS-Collaboration: M. Derrick et al.
Measurement of the Proton Structure Function F_2 at Low x and Low Q^2 at HERA
DESY 95-193

[83] ZEUS-Collaboration: M. Derrick et al.
Diffractive Hard Photoproduction at HERA and Evidence for the Gluon Content of the Pomeron
Phys. Lett. **B356**(1995) 129–146

[84] ZEUS-Collaboration: M. Derrick et al.
Exclusive ρ^0 production in Deep Inelastic Electron-Proton Scattering at HERA
Phys. Lett. **B356** (1995) 601-616

[85] ZEUS-Collaboration: M. Derrick et al.
Measurement of Total and Partial Photon Proton Cross Sections at 180 GeV Center of Mass Energy
Z. f. Physik, **C63** (1994) 391-408

[86] ZEUS-Collaboration: M. Derrick et al.
The ZEUS Detector, Status Report 1993
DESY 1993